A Composite Ultrasonic Transducer with a Fractal Architecture

Ebrahem A. Algehyne and Anthony J. Mulholland

Department of Mathematics and Statistics

University of Strathclyde

Livingstone Tower, 26 Richmond Street

Glasgow, UK

G1 1XH

September 14, 2015

Abstract

To ensure the safe operation of many safety critical structures such as nuclear plants, aircraft and oil pipelines, non-destructive imaging is employed using piezoelectric ultrasonic transducers. These sensors typically operate at a single frequency due to the restrictions imposed on its resonant behaviour by the use of a single length scale in its design. To allow these transducers to transmit and receive more complex signals it would seem logical to use a range of length scales in the design so that a wide range of resonating frequencies will result. In this article we derive a mathematical model to predict the dynamics of an ultrasound transducer that achieves this range of length scales by adopting a fractal architecture. In fact, the device is modelled as a graph where the nodes represent segments of the piezoelectric and polymer materials. The electrical and mechanical fields that are contained within this graph are then expressed in terms of a finite element basis. The structure of the resulting discretised equations yields to a renormalisation methodology which is used to derive expressions for the non-dimensionalised electrical impedance and the transmission and reception sensitivities. A comparison with a homogenised (standard) design shows some benefits of these fractal designs.

1 Introduction

Ultrasonic transducers are devices that are used to convert energy from one form to another [6]. In this context, they convert energy from its electrical form to mechanical vibrations and vice versa [37, 36]. These devices can act as both transmitters and receivers, they typically work by emitting a wave (which is con-

verted from electrical energy to mechanical energy) through a medium, then listening and interpreting the echoes of the transmitted wave (which at this point is transformed back into electrical energy from mechanical vibrations). To further improve the transmission and reception sensitivities [13, 29], composite structures are utilized in piezoelectric ultrasonic transducers. Many biological species such as dolphins, bats, etc, naturally produce and receive ultrasound by utilising a wide variety of intricate geometries in their transduction 'equipment'; often with resonators spread over a range of length scales [26, 25, 20, 7, 9, 27, 31, 8]. However, the man-made transducers tend to employ a regular geometry on a single length scale. Due to this characteristic, the man-made transducers are unable to operate over a wider range of frequencies resulting in transmission and reception sensitivities with narrow bandwidths. To produce transducers with wider bandwidths, structures with a range of geometrical components need to be mathematically modelled. One such structures is a fractal [23, 24, 28]. One approach to designing a new transducer is to experimentally assess its operating ability, however this is very time consuming. Each device requires materials to be sought, cut to the desired shape, bonded to other components such as inatching and backing layers, and is expensive and time consuming. In addition, to determine its transmission sensitivity the device has to be immersed in a water tank, input voltages of different frequencies are applied, and a hydrophone placed at some distance from the transducer monitors the output. An assessment can also be made by connecting the transducer to an electrical circuit and measuring its electrical impedance over a range of frequencies. Given the large number of variables present in any design then the use of mathematical models to assess radically new concepts such as that proposed in this paper is fully justified. Various papers have described wave propagation in fractal media for other

applications [17, 11, 18, 1, 2, 5, 12, 19]. This paper will build a model of a fractal ultrasound transducer and compares this model's operational qualities with that of a standard (homogenised) design. In the past, a finite differences approach [23] was used in the examination of this topic; an approach in which each edge of the fractal lattice was modelled as a one dimensional piezoelectric bar with the only degree of freedom present in the plane of the lattice. Consequently, there was no allowance for other types of motion of the lattice or directions of the electric field. This was a local description of the dynamics of the individual edges which, when joined to other edges from the lattice, led to the global dynamics of the device. To account for the three dimensional world that the device is embedded within, this paper will derive the governing equations from the general tensor equations. This framework enables the deployment of different parameterisations and a scenario where the displacement acts out of the plane of the lattice with the electric field operating within the plane of the lattice will be examined in this paper. We will use a finite element methodology and introduce new basis functions to express the wave fields within the lattice. This Galerkin approach leads to discrete formulation that lends itself to a renormalisation approach. The Sierpinski gasket will be used for the simulation of a self-similar transducer in this paper [10, 32]. Such an ultrasonic transducer would start with an equilateral triangle of piezoelectric crystal. This equilateral triangle is composed of four identical equilateral sub-triangles whose side length is half of the original. The first generation ($n = 1$) would be obtained by replacing the central sub-triangle by a polymer material. This process is then repeated for several generations with the removed sub-triangles from the smallest triangles being filled with a polymer (see Figure 1). The associated graph is constructed by a process which starts from the order $n = 1$ design (which consists of three

piezoelectric triangles and one polymer triangle), assigns a vertex to the centre of each of these triangles and, by connecting these vertices together with edges, the SG(3,4) lattice at generation level $n = 1$ is constructed (see Figure 2). The polymer triangle has a vertex denoted by a non-filled circle which was degree 3 whereas each piezoelectric triangle has a vertex denoted by a filled circle and has degree 4. The lattice has side length L units which remains constant as the generation level n increases. Therefore, as n increases, the length of the edge between adjacent vertices tends to zero and in this limit the lattice will perfectly match the space filling properties of the original Sierpinski gasket [21]. The total number of vertices is $N^* = 3^n + 3^{n-1} = N^{(n)} + 1$ where $N^{(1)} = 3$ and $N^{(2)} = 11$ (see Figures 3 and 4) and $h^{(n)} = L/(2^n - 1)$ is the edge length between any two adjacent piezoelectric vertices. The piezoelectric vertex degree is 4 (apart from the boundary vertices (input/output vertices) which have degree 3) and $M = (5 \times 3^n - 3)/2$ denotes the total number of edges. These boundary vertices will be used to interact with external loads (both electrical and mechanical) and so we introduce fictitious vertices A, B and C to accommodate these interfacial boundary conditions (see Figures 3 and 4). Denote by Ω the set of points lying on the edges or vertices of $SG(3, 4)$ and denote the region's boundary by $\partial\Omega$. Note that the edges joining the piezoelectric nodes to the polymer nodes are composed of a piezoelectric section (shown by the full line in Figure 3 along the edge joining node 1 to 4) and a polymer section (shown by the dashed line along this same edge). In what follows we will retain the freedom to vary the fraction of piezoelectric material in this edge from $\nu = 1$ (piezoelectric material only) to $\nu = 0$ (polymer material only).

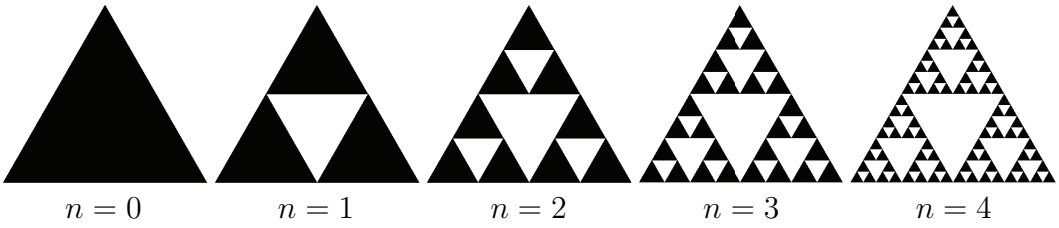

Figure 1: The first few generations of the Sierpinski gasket. The black triangles are a piezoelectric material and the *smallest* white triangles are a polymer material.

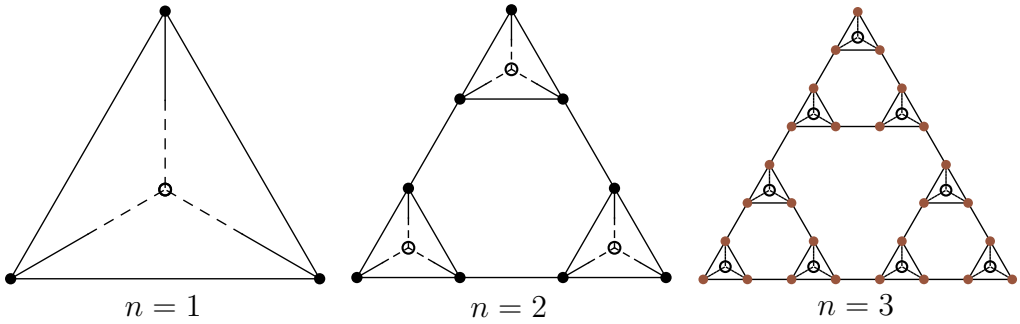

Figure 2: The first few generations of the Sierpinski gasket lattice $SG(3, 4)$.

2 Model Derivation

The lattice represents the vibrations of piezoelectric and polymer materials (here the focus will be on PZT-5H and HY1300/CY1301 hardset [30] respectively) that have been manufactured to form a Sierpinski gasket. The interplay between the electrical and mechanical behaviour of the lattice vertices is described by the piezoelectric constitutive equations [37, 36]

$$T_{ij} = c_{ijkl}S_{kl} - e_{kij}E_k, \tag{1}$$

$$D_i = e_{ikl}S_{kl} + \varepsilon_{ik}E_k, \tag{2}$$

where T_{ij} is the stress tensor, c_{ijkl} is the stiffness tensor, S_{kl} is the strain tensor, e_{kij} is the piezoelectric tensor, E_k is the electric field vector, D_i is the electrical displacement vector and ε_{ik} is the permittivity tensor (where the Einstein summation convention is adopted). The strain tensor is related to the displacement gradients $u_{i,j}$ by

$$S_{ij} = \frac{u_{i,j} + u_{j,i}}{2}, \tag{3}$$

and the electric field vector is related to the electric potential ϕ via

$$E_i = -\phi_{,i}. \tag{4}$$

The dynamics of the piezoelectric material is then governed by

$$\rho^E \ddot{u}_i = T_{ji,j}, \tag{5}$$

subject to Gauss' law

$$D_{i,i} = 0 \tag{6}$$

where ρ^E is the density and u_i is the component of displacement in the direction of the i^{th} basis vector. So, combining equations (5) and (1) gives

$$\rho^E \ddot{u}_i = c_{jikl} S_{kl,j} - e_{kji} E_{k,j}. \tag{7}$$

Combining equations (6) and (2) gives

$$D_{i,i} = e_{ikl} S_{kl,i} + \varepsilon_{ik} E_{k,i} = 0. \tag{8}$$

We will restrict attention to the out of plane displacement only (a horizontal shear wave) by stipulating that

$$\underline{u} = \big(0, 0, u_3(x_1, x_2, t)\big), \tag{9}$$

this choice of parameterisation will simplify the algebra significantly and will lead to a scalar dynamical equation. It also will allow us to consider the transverse

vibrations of the device which is of engineering interest in the application of this device. There are of course other parameterisations that could be chosen and a suitable choice would also afford the study of the vector elastodynamical equations. So only $u_{3,1}$ and $u_{3,2}$ are nonzero then equation (7) gives

$$\rho^E \ddot{u}_3 = c_{13kl} S_{kl,1} + c_{23kl} S_{kl,2} - e_{kj3} E_{k,j}. \tag{10}$$

From equation (3) we get

$$S_{ij} = \begin{cases} \frac{1}{2} u_{3,1} & i = 1, j = 3 \text{ or } i = 3, j = 1 \\ \frac{1}{2} u_{3,2} & i = 2, j = 3 \text{ or } i = 3, j = 2 \\ 0 & \text{otherwise,} \end{cases} \tag{11}$$

so equation (10) gives

$$\rho^E \ddot{u}_3 = c_{1331} u_{3,11} + c_{1332} u_{3,21} + c_{2331} u_{3,12} + c_{2332} u_{3,22} - e_{kj3} E_{k,j}. \tag{12}$$

From the properties of PZT-5H (see Appendix 11.2), then

$$\rho^E \ddot{u}_3 = c_{44}(u_{3,11} + u_{3,22}) - e_{kj3} E_{k,j}. \tag{13}$$

since $c_{55} = c_{44}$ and the Voigt notation has been used to express these tensors as matrices. For example, $c_{44} \equiv c_{2323}$ and $e_{24} \equiv e_{223}$. Now if $\underline{E} = \big(E_1(x_1, x_2), E_2(x_1, x_2), 0\big)$ then

$$\rho^E \ddot{u}_3 = c_{44}(u_{3,11} + u_{3,22}) - e_{113} E_{1,1} - e_{123} E_{1,2} - e_{213} E_{2,1} - e_{223} E_{2,2}. \tag{14}$$

That is

$$\rho^E \ddot{u}_3 = c_{44}(u_{3,11} + u_{3,22}) - e_{15} E_{1,1} - e_{14} E_{1,2} - e_{25} E_{2,1} - e_{24} E_{2,2}. \tag{15}$$

Then, for PZT-5H,

$$\rho^E \ddot{u}_3 = c_{44}(u_{3,11} + u_{3,22}) - e_{24}(E_{1,1} + E_{2,2}), \tag{16}$$

since $e_{15} = e_{24}$. From equation (8) we get

$$e_{113}S_{13,1} + e_{131}S_{31,1} + e_{223}S_{23,2} + e_{232}S_{32,2} + \varepsilon_{11}E_{1,1} + \varepsilon_{22}E_{2,2} = 0. \tag{17}$$

That is, for PZT-5H,

$$e_{15}u_{3,11} + e_{24}u_{3,22} + \varepsilon_{11}E_{1,1} + \varepsilon_{22}E_{2,2} = 0. \tag{18}$$

Therefore

$$e_{24}(u_{3,11} + u_{3,22}) + \varepsilon_{11}(E_{1,1} + E_{2,2}) = 0 \tag{19}$$

since $\varepsilon_{11} = \varepsilon_{22}$ for PZT-5H. So we get

$$E_{1,1} + E_{2,2} = -\frac{e_{24}}{\varepsilon_{11}}(u_{3,11} + u_{3,22}). \tag{20}$$

Substituting this equation into equation (16) gives

$$\rho^E \ddot{u}_3 = c_{44}(u_{3,11} + u_{3,22}) + \frac{e_{24}^2}{\varepsilon_{11}}(u_{3,11} + u_{3,22}). \tag{21}$$

A similar analysis can be conducted for the polymer phase. The dynamical equation in each phase can be written as

$$\ddot{u}_3 = c^2\nabla^2 u_3 \tag{22}$$

where c is the shear wave velocity defined as

$$c = \begin{cases} c_T = \sqrt{c_{44}^T/\rho^E}, \quad c_{44}^T = c_{44}^E + e_{24}^2/\varepsilon_{11}^E, & \text{PZT-5H} \\ c_P = \sqrt{c_{44}^P/\rho^P}, & \text{polymer} \end{cases} \tag{23}$$

and $\nabla^2 = \partial^2/\partial x_1^2 + \partial^2/\partial x_2^2$. c_{44}^T is the piezoelectrically stiffened shear modulus in the ceramic phase, c_{44}^P is the shear modulus of the polymer, $\rho^{E/P}$ is the density in the E-piezoelectric / P- polymer phase, e_{24} is an element of the piezoelectric tensor, and ε_{11} is an element of the permittivity tensor. The polymer's

material tensors are given in the Appendix 11.2 and the derivation c_P follows similar lines to these for the piezoelectric material. We impose the initial conditions $u_3(\underline{x}, 0) = \dot{u}_3(\underline{x}, 0) = 0$ and the boundary conditions of continuity of displacement and force at $\partial\Omega$ (the boundary to Ω). By introducing the non-dimensionalised variable $\theta = c_T t/h$ then (temporarily dropping the subscript on u and the superscript on h)

$$\frac{\partial^2 u}{\partial \theta^2} = \frac{h^2}{c_T^2} c^2 \, \nabla^2 u. \tag{24}$$

Applying the Laplace transform $\mathscr{L} : \theta \to q$ then gives

$$q^2 \, \bar{u} = \frac{h^2}{c_T^2} c^2 \, \nabla^2 \bar{u}. \tag{25}$$

We will seek a weak solution $\bar{u} \in H^1(\Omega)$ where on the boundary $\bar{u} = \bar{u}_{\partial\Omega} \in H^1(\partial\Omega)$. Now multiplying by a test function $w \in H^1_B(\Omega)$, where $H^1_B(\Omega) := \{w \in H^1(\Omega) : w = 0 \, \text{on} \, \partial\Omega\}$, integrating over the region Ω, and using Green's first identity $\int_\Omega \psi \, \nabla^2 \phi \, dv = \oint_{\partial\Omega} \psi (\nabla\phi.\underline{n}) \, dr - \int_\Omega \nabla\phi.\nabla\psi \, dv$, where $\underline{n}$ is the outward pointing unit normal of surface element dr, gives

$$\int_\Omega q^2 \, \bar{u} \, w \, d\underline{x} = \frac{h^2}{c_T^2} c^2 \oint_{\partial\Omega} w (\nabla\bar{u}.\underline{n}) \, dr - \frac{h^2}{c_T^2} c^2 \int_\Omega \nabla\bar{u}.\nabla w \, d\underline{x}. \tag{26}$$

Now $h^2 \oint_{\partial\Omega} w(\nabla\bar{u}.\underline{n}) \, dr$ is zero since $w = 0$ on $\partial\Omega$ and so, we seek $\bar{u} \in H^1(\Omega)$ such that

$$q^2 \int_\Omega \bar{u} \, w \, d\underline{x} = -\frac{h^2}{c_T^2} c^2 \int_\Omega \nabla\bar{u}.\nabla w \, d\underline{x} \tag{27}$$

where $w \in H^1_B(\Omega)$.

3 Galerkin discretisation

Using a standard Galerkin method we replace $H^1(\Omega)$ and $H^1_B(\Omega)$ by the finite dimensional subspaces S and $S_B = S \cap H^1_B(\Omega)$. Let $U_B \in S$ be a function that

approximates $\bar{u}_{\partial\Omega}$ on $\partial\Omega$, then the discretised problem involves finding $\bar{U} \in S$ such that

$$q^2 \int_\Omega \bar{U}\ W\ d\underline{x} = -\frac{h^2}{c_T^2} c^2 \int_\Omega \nabla\bar{U}.\nabla W\, d\underline{x}, \tag{28}$$

where W is the test function expressed in this finite dimensional space. Let $\{\phi_1, \phi_2, \cdots, \phi_N, \phi_{N+1}\}$ form a basis of S_B and set $W = \phi_j$, then

$$q^2 \int_\Omega \bar{U}\phi_j\ d\underline{x} = -\frac{h^2}{c_T^2} c^2 \int_\Omega \nabla\bar{U}.\nabla\phi_j\, d\underline{x}, \quad j = 1, \ldots, N+1. \tag{29}$$

Furthermore, let ψ_I, $I = \{N+2, N+3, N+4\}$ form a basis for the boundary nodes and let

$$\bar{U} = \sum_{i=1}^{N+1} U_i\phi_i + \sum_{i\in I} U_{B_i}\psi_i. \tag{30}$$

Hence, equation (29) becomes

$$\begin{aligned} &\sum_{i=1}^{N+1} \left(q^2 \int_\Omega \phi_i\phi_j\ d\underline{x} + \frac{h^2}{c_T^2} c^2 \int_\Omega \nabla\phi_i.\nabla\phi_j\ d\underline{x} \right) U_i = \\ &-\sum_{i\in I} \left(q^2 \int_\Omega \psi_i\phi_j\ d\underline{x} + \frac{h^2}{c_T^2} c^2 \int_\Omega \nabla\psi_i.\nabla\phi_j\ d\underline{x} \right) U_{B_i} \end{aligned} \tag{31}$$

where $j \in \{1, 2, \ldots, N, N+1\}$. That is

$$A_{ji}U_i = b_j \tag{32}$$

where

$$A_{ji} = q^2 \int_\Omega \phi_i\phi_j\ d\underline{x} + \frac{h^2}{c_T^2} c^2 \int_\Omega \nabla\phi_i.\nabla\phi_j\ d\underline{x}, \tag{33}$$

and

$$b_j = -\sum_{i\in I} \left(q^2 \int_\Omega \psi_i\phi_j\ d\underline{x} + \frac{h^2}{c_T^2} c^2 \int_\Omega \nabla\psi_i.\nabla\phi_j\ d\underline{x} \right) U_{B_i}. \tag{34}$$

It is important to now explicitly record the fractal generation level n and so equation (33) can be written

$$A_{ji}^{(n)} = q^2\, H_{ji}^{(n)} + \frac{\left(h^{(n)}\right)^2}{c_T^2}\, K_{ji}^{(n)}, \tag{35}$$

where

$$H_{ji}^{(n)} = \int_{\Omega} (\phi_j \phi_i) d\underline{x}, \tag{36}$$

and

$$K_{ji}^{(n)} = c^2 \int_{\Omega} (\nabla \phi_j . \nabla \phi_i) d\underline{x}. \tag{37}$$

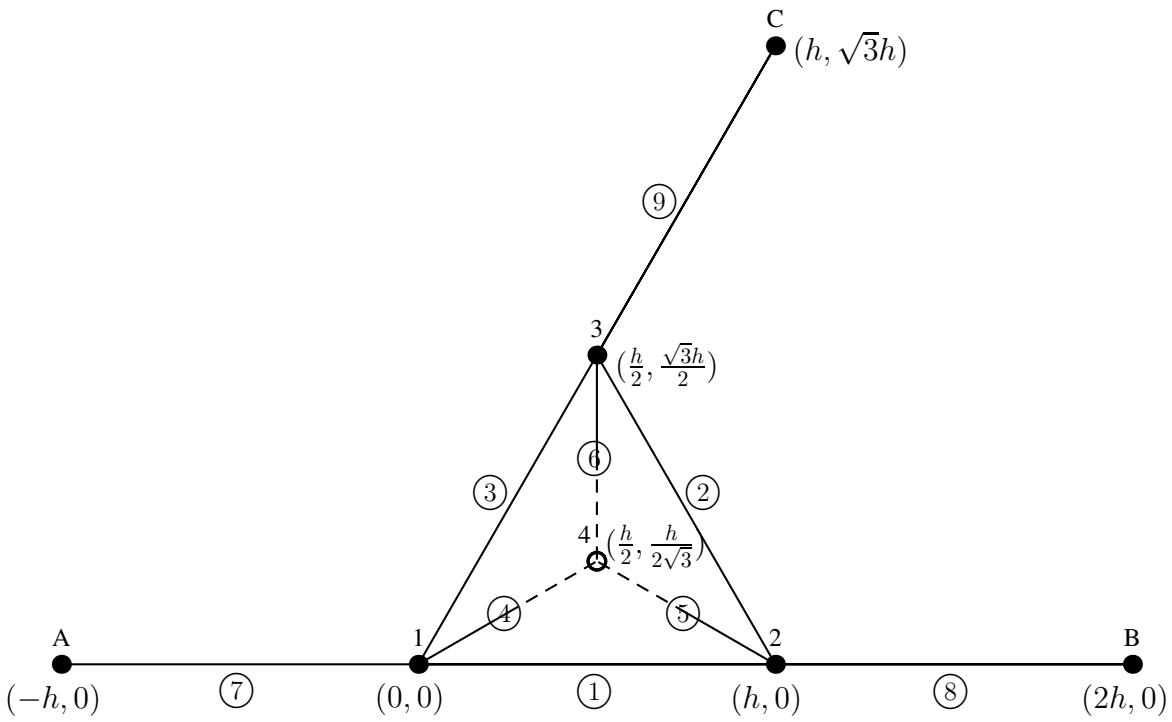

Figure 3: The modified Sierpinski Gasket lattice $SG(3, 4)$ at generation level $n = 1$. Nodes $1, 2$ and 3 are the input/output piezoelectric nodes, node 4 is a polymer node, and nodes A (or 5), B (or 6) and C (or 7) are fictitious nodes used to accommodate the boundary conditions. The lattice has 9 elements (circled numbers), with two vertices adjacent to each element.

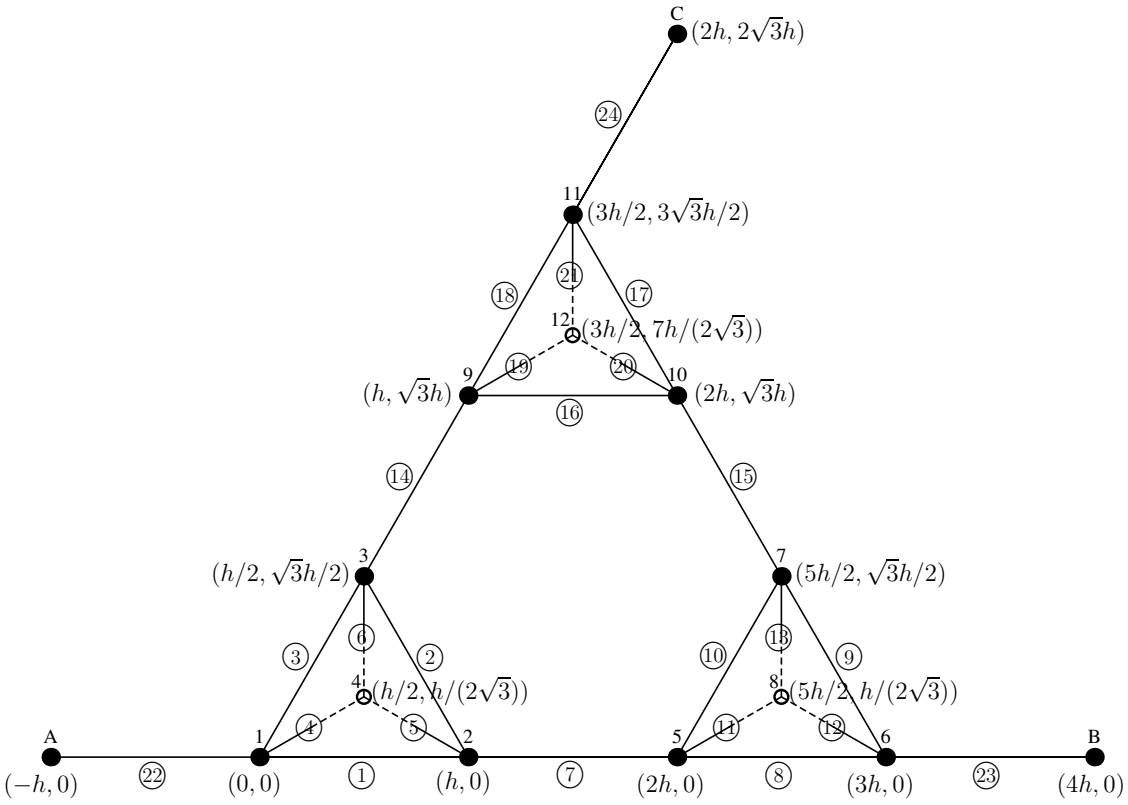

Figure 4: The modified Sierpinski Gasket lattice $SG(3, 4)$ at generation level $n = 2$. Nodes A (or 13), B (or 14) and C (or 15) are fictitious nodes used to accommodate the boundary conditions. The lattice has 24 elements (circled numbers), with two vertices adjacent to each element.

3.1 Transformations of the fundamental basis functions

In this section we will consider transformations of some fundamental basis functions $\hat{\phi}_J$, $\hat{\phi}_K$ and $\hat{\psi}_I$ (see Figures 5, 6 and 7) to get basis functions ϕ_J, ϕ_K and ψ_I at each vertex in the lattice. These basis functions will be based on a fundamental basis function for the interior piezoelectric vertices (J), one for the interior polymer vertices (K) and one for the exterior piezoelectric vertices (I).

We choose the design of the fundamental basis functions $\hat{\phi}_J$ as shown in Figure 5 with nodes $(\frac{\sqrt{3}}{2}h, \frac{h}{2})$, $(\frac{\sqrt{3}}{2}h, \frac{-h}{2})$, $(\frac{h}{\sqrt{3}}, 0)$ and $(\frac{-\sqrt{3}}{2}h, \frac{h}{2})$. The $\hat{\phi}_J$ basis function is defined such that (we ease the notation by setting $x_1 = x$, and $x_2 = y$)

$$\hat{\phi}_j(x,y) = \begin{cases} 1 & \text{if } (x,y) = (x_j, y_j) \\ 0 & \text{if } (x,y) = \text{coordinates of vertices adjacent to vertex } j. \end{cases} \tag{38}$$

The basis functions have a compact support and are identically zero outside the edges that are incident upon the particular vertex.

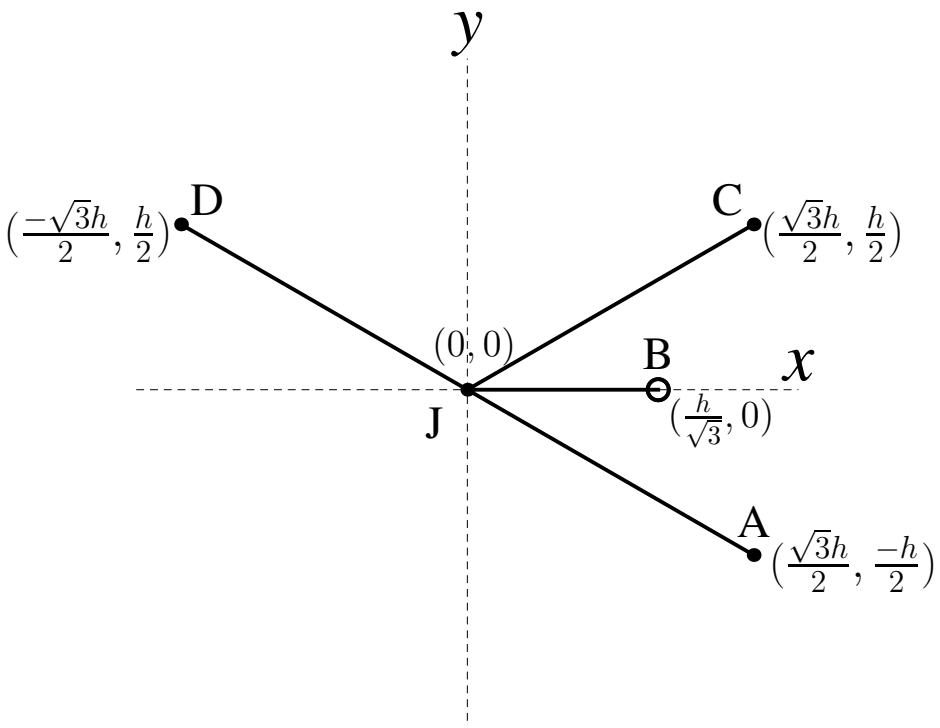

Figure 5: Plan view of $\hat{\phi}_J$, the fundamental basis function for the piezoelectric vertices; it is symmetric with respect to the x axis.

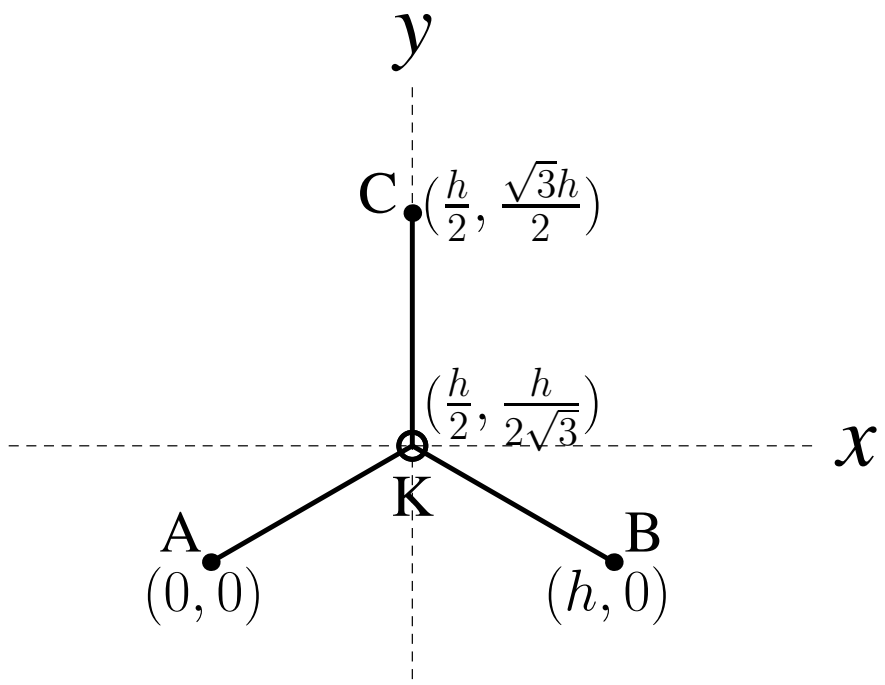

Figure 6: Plan view of $\hat{\phi}_K$, the fundamental basis function for the polymer vertices.

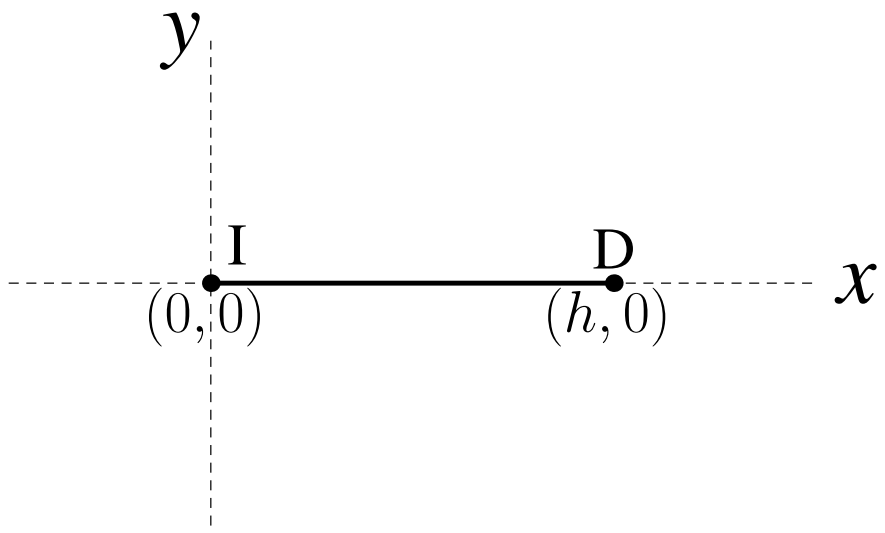

Figure 7: Plan view of $\hat{\phi}_I$, the fundamental basis function.

For the fundamental basis functions $\hat{\phi}_J$ (see Figure 5) we have five nodes and so the functional form has five unknowns. Setting

$$\hat{\phi}_J(x,y) = a + bx + cy + dx^2 + ey^2, \tag{39}$$

then, by applying equation (38), we get

$$\begin{aligned}
\hat{\phi}_J(0,0) &= a = 1, && (40)\\
\hat{\phi}_J(\frac{h}{\sqrt{3}},0) &= 1 + \frac{h}{\sqrt{3}}b + \frac{h^2}{3}d = 0, && (41)\\
\hat{\phi}_J(\frac{\sqrt{3}h}{2},\frac{h}{2}) &= 1 + \frac{\sqrt{3}}{2}hb + \frac{h}{2}c + \frac{3}{4}h^2d + \frac{h^2}{4}e = 0, && (42)\\
\hat{\phi}_J(\frac{\sqrt{3}h}{2},\frac{-h}{2}) &= 1 + \frac{\sqrt{3}}{2}hb - \frac{h}{2}c + \frac{3}{4}h^2d + \frac{h^2}{4}e = 0 && (43)
\end{aligned}$$

and

$$\hat{\phi}_J(\frac{-\sqrt{3}h}{2},\frac{h}{2}) = 1 - \frac{\sqrt{3}}{2}hb + \frac{h}{2}c + \frac{3}{4}h^2d + \frac{h^2}{4}e = 0. \tag{44}$$

Equations (41) to (44) provide four equations in the four unknowns b, c, d and e, which give $b = 0$, $c = 0$, $d = -3/h^2$ and $e = 5/h^2$ and substituting these into equation (39) gives

$$\hat{\phi}_J(x,y) = 1 - \frac{3}{h^2}x^2 + \frac{5}{h^2}y^2. \tag{45}$$

Similarly, for the fundamental basis function $\hat{\phi}_K$ (see Figure 6), we have four nodes, so we need to form an equation with four unknowns, so consider

$$\hat{\phi}_K(x,y) = a + bx + cy + d(x^2 + y^2). \tag{46}$$

By applying equation (38), then we get

$$\begin{aligned}
\hat{\phi}_K(0,0) &= a = 0, && (47)\\
\hat{\phi}_K(h,0) &= hb + h^2d = 0, && (48)\\
\hat{\phi}_K(\frac{h}{2},\frac{\sqrt{3}h}{2}) &= \frac{h}{2}b + \frac{\sqrt{3}h}{2}c + h^2d = 0 && (49)
\end{aligned}$$

and

$$\hat{\phi}_K(\frac{h}{2}, \frac{h}{2\sqrt{3}}) = \frac{h}{2}b + \frac{h}{2\sqrt{3}}c + \frac{h^2}{3}d = 1. \tag{50}$$

Equations (48) to (50) provide three equations in the three unknowns b, c and d, which gives $b = 3/h$, $c = \sqrt{3}/h$ and $d = -3/h^2$, and substituting these into equations (46) gives

$$\hat{\phi}_K(x, y) = \frac{3}{h}x + \frac{\sqrt{3}}{h}y - \frac{3}{h^2}(x^2 + y^2). \tag{51}$$

Similarly, for the fundamental basis functions $\hat{\psi}_I$ (see Figure 7), we have two nodes, so consider

$$\hat{\psi}_I(x, y) = a + d(x^2 + y^2). \tag{52}$$

By applying equation (38), we get

$$\hat{\psi}_I(0, 0) = a = 1 \tag{53}$$

and

$$\hat{\psi}_I(h, 0) = 1 + h^2 d = 0. \tag{54}$$

This equation gives $d = -1/h^2$, and substituting this into equation (52) gives

$$\hat{\psi}_I(x, y) = 1 - \frac{1}{h^2}(x^2 + y^2). \tag{55}$$

Having established the fundamental (canonical) basis functions for each type of vertex in the lattice we now need to calculate the specific basis functions for each vertex. In order to do this each fundamental basis functions is mapped onto the specific vertex by a series of transformations such as a translation, a rotation, or a reflection in the x or y axis. This has to be performed for each vertex in the lattice and below we illustrate the process by detailing the transformations for a small subset of these vertices.

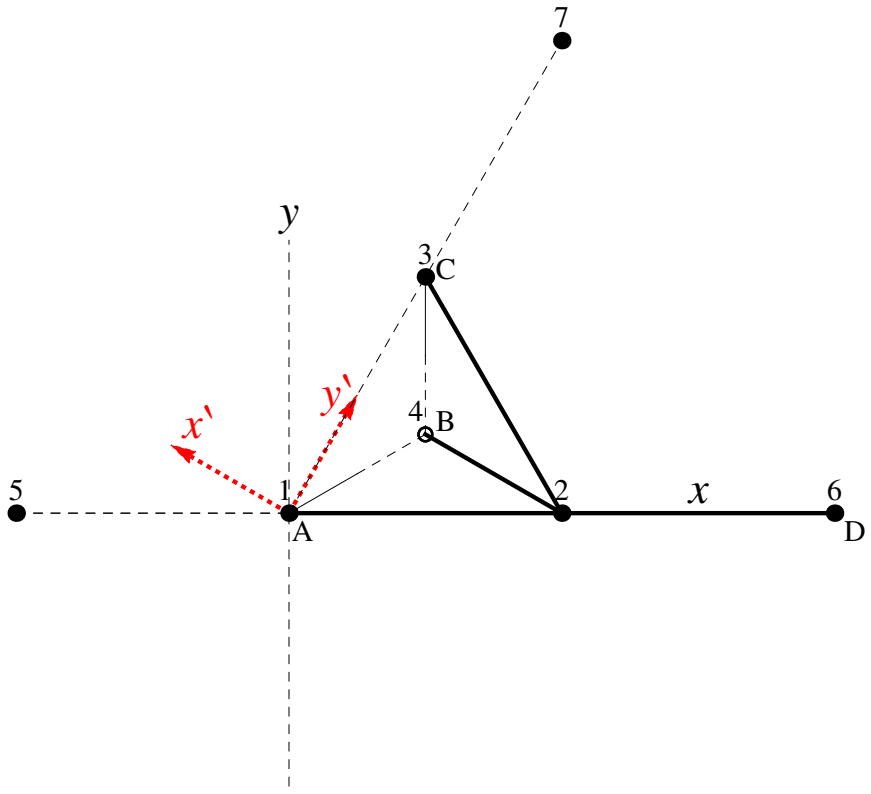

Figure 8: The plan view of the basis function ϕ_2. The coordinate axis x' lies along the edge JD in Figure 5.

In Figure 8 the plan view of the basis function centred on vertex 2 at fractal generation level $n = 1$ is shown. The form of this basis function is obtained by relating it to the canonical basis function shown in Figure 5 as given by equation (45) (with respect to the (x', y') coordinate frame shown in red in Figure 8). To transform this plan view of ϕ_2 to the plan view of $\hat{\phi}_J$ then we simply need to transform the (x, y) axis in Figure 8 to the (x', y') axis in Figure 5. So the first step is via a translation of $x_2 = (h, 0)$ to $x_2' = (0, 0)$ (see Figure 9). So, from equation (45), we have so far

$$\phi_2(x - h, y) = 1 - \frac{3}{h^2}(x - h)^2 + \frac{5}{h^2}y^2. \tag{56}$$

In general, the translation of the basis vectors to the point (x_j, y_j) is given by the transformation

$$R_T(\underline{x}_j) = \begin{pmatrix} x - x_j \\ y - y_j \end{pmatrix}. \tag{57}$$

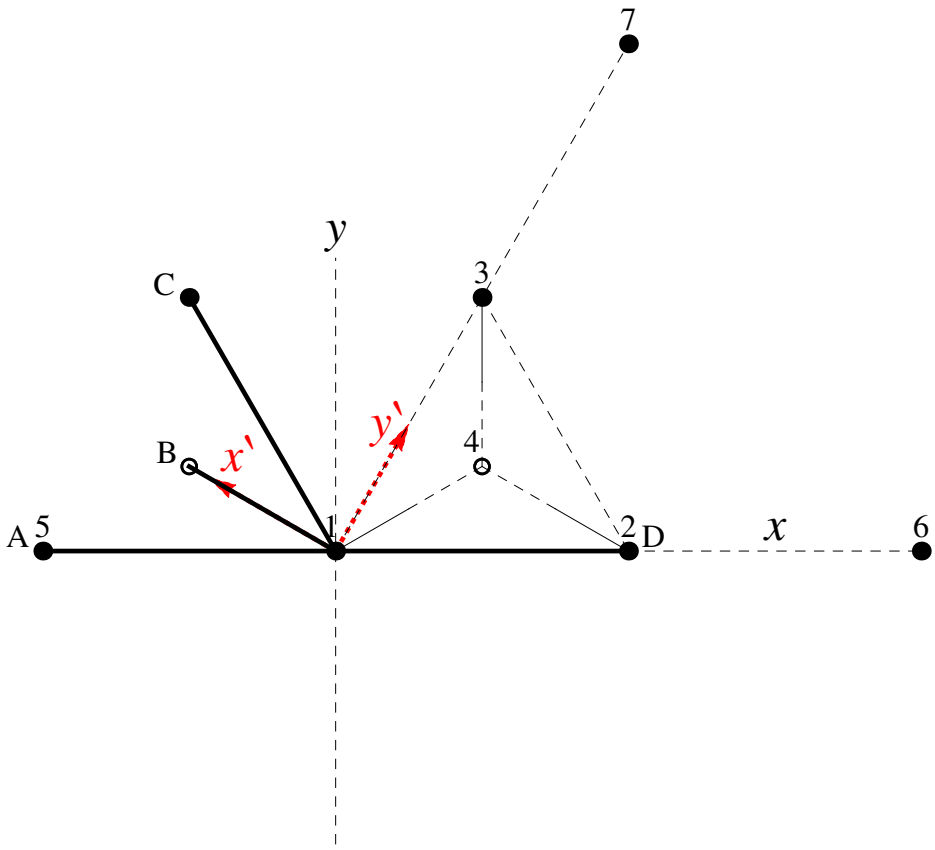

Figure 9: The plan view of ϕ_2, after the first transformation.

The second step in transforming ϕ_2 to $\hat{\phi}_J$ is via a reflection in the (y axis) (see Figure 10). Reflection in the y axis can be obtained by multiplying the basis vectors by the matrix

$$R_R = \begin{pmatrix} -1 & 0 \\ 0 & 1 \end{pmatrix}. \tag{58}$$

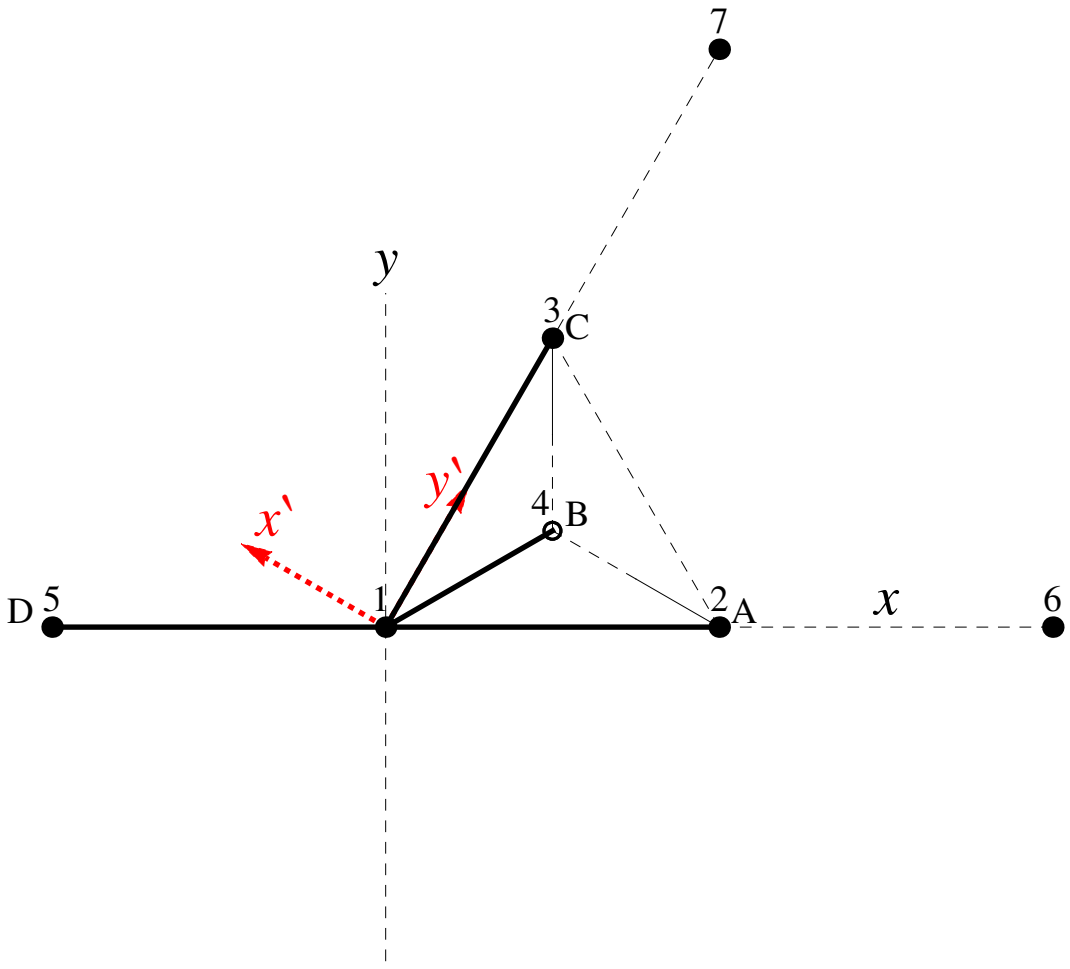

Figure 10: The plan view of ϕ_2, after the second transformation.

Then from this plan view of ϕ_2, the third (final) step in transforming ϕ_2 to $\hat{\phi}_J$ is via a rotation of $-\pi/6$ (clockwise) (see Figure 11). The anticlockwise rotation by an amount θ is obtained by multiplying the basis vectors by the matrix

$$R_\theta = \begin{pmatrix} \cos\theta & -\sin\theta \\ \sin\theta & \cos\theta \end{pmatrix}. \tag{59}$$

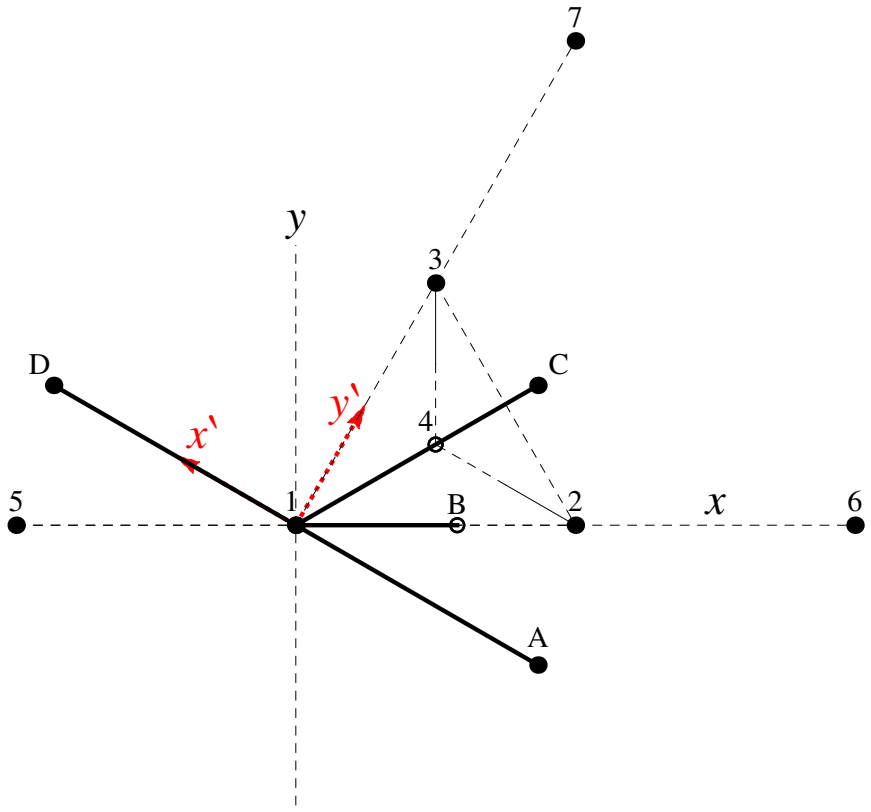

Figure 11: The plan view of ϕ_2, after the third (final) transformation.

So, for example, at fractal generation level $n = 1$,

$$\begin{aligned}
\phi_2 &= R_{\frac{-\pi}{6}} \circ R_R \circ R_T(\underline{x}_2)\hat{\phi}_J(x,y) && (60)\\
&= R_{\frac{-\pi}{6}} \circ R_R\hat{\phi}_J(x-x_2,y)\\
&= R_{\frac{-\pi}{6}}\hat{\phi}_J(-x-x_2,y)\\
&= \hat{\phi}_J\big(-\cos(-\frac{\pi}{6})(x+x_2)-\sin(-\frac{\pi}{6})y, -\sin(-\frac{\pi}{6})(x+x_2)+\cos(-\frac{\pi}{6})y\big)\\
&= \hat{\phi}_J\big(-(x+h)\frac{\sqrt{3}}{2}+\frac{1}{2}y, \frac{1}{2}(x+h)+\frac{\sqrt{3}}{2}y\big)\\
&= 1-\frac{3}{h^2}\big(-(x+h)\frac{\sqrt{3}}{2}+\frac{1}{2}y\big)^2+\frac{5}{h^2}\big(\frac{1}{2}(x+h)+\frac{\sqrt{3}}{2}y\big)^2\\
&= \frac{2}{h}x-\frac{4\sqrt{3}}{h}y+\frac{4\sqrt{3}}{h^2}xy-\frac{1}{h^2}x^2+\frac{3}{h^2}y^2. && (61)
\end{aligned}$$

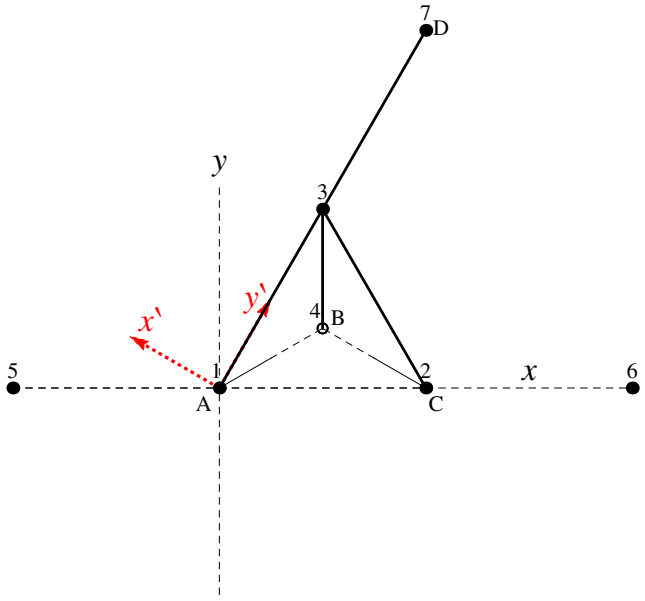

Figure 12: The plan view the basis function ϕ_3.

To transform ϕ_3 (see Figure 12) to $\hat{\phi}_J$ (see Figure 5) we need a translation of $x_3 = (h/2, \sqrt{3}h/2)$ (see Figure 13).

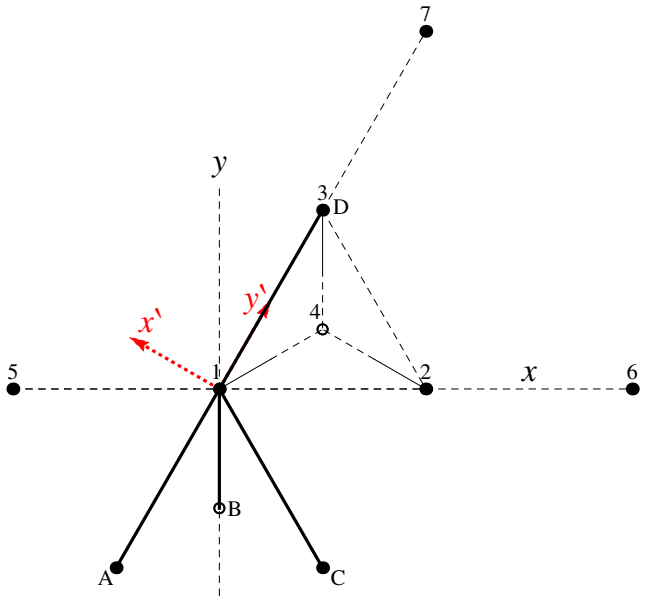

Figure 13: The plan view of ϕ_3, after the first step of transformation.

The second (final) step in transforming ϕ_3 to $\hat{\phi}_J$ is via a rotation of $\pi/2$ (anti-clockwise) (see Figure 14).

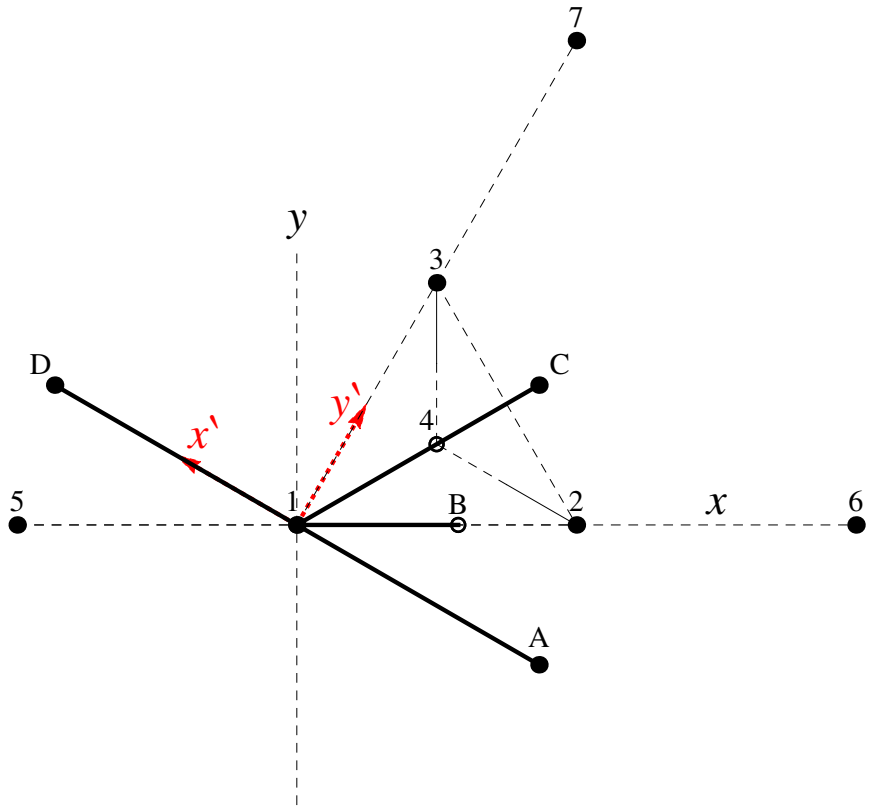

Figure 14: The plan view of ϕ_3, after the second step of transformation.

So,

$$\begin{aligned}
\phi_3 &= R_{\frac{\pi}{2}} \circ R_T(\underline{x}_3)\hat{\phi}_J(\underline{x}) && (62)\\
&= R_{\frac{\pi}{2}} \circ \hat{\phi}_J\big(x - \frac{h}{2}, y - \frac{\sqrt{3}h}{2}\big)\\
&= \hat{\phi}_J\big(-y + \frac{\sqrt{3}h}{2}, x - \frac{h}{2}\big)\\
&= 1 - \frac{3}{h^2}\big(-y + \frac{\sqrt{3}h}{2}\big)^2 + \frac{5}{h^2}\big(x - \frac{h}{2}\big)^2\\
&= 1 - \frac{5}{h}x + \frac{3\sqrt{3}}{h}y + \frac{5}{h^2}x^2 - \frac{3}{h^2}y^2. && (63)
\end{aligned}$$

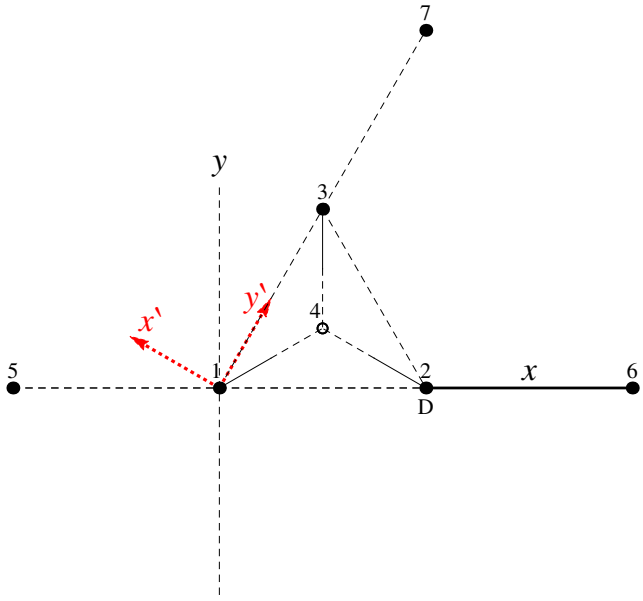

Figure 15: The plan view of the basis function ψ_6, before transformation.

To transform the basis function ψ_6 (see Figure 15) to the canonical basis function $\hat{\psi}_I$ (see Figure 7), the first step is a translation of $x_6 = (2h, 0)$ (see Figure 16).

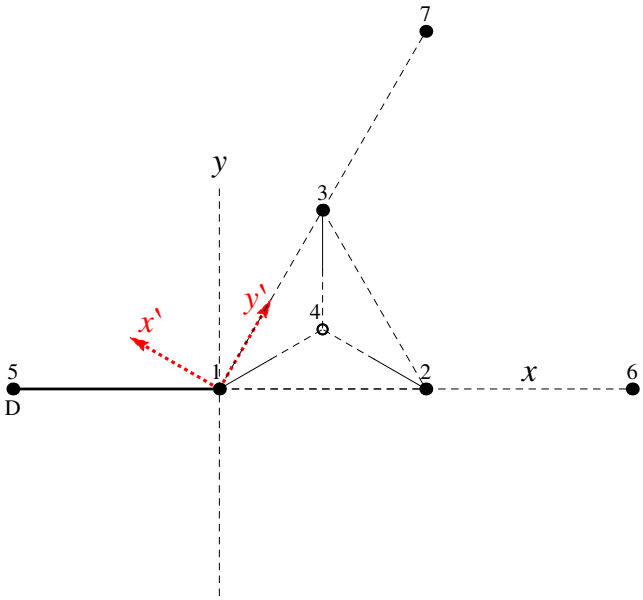

Figure 16: The plan view of ψ_6, after the first step of transformation.

The second (final) step in transforming ψ_6 to $\hat{\psi}_I$ is via a rotation of π (see Figure 17).

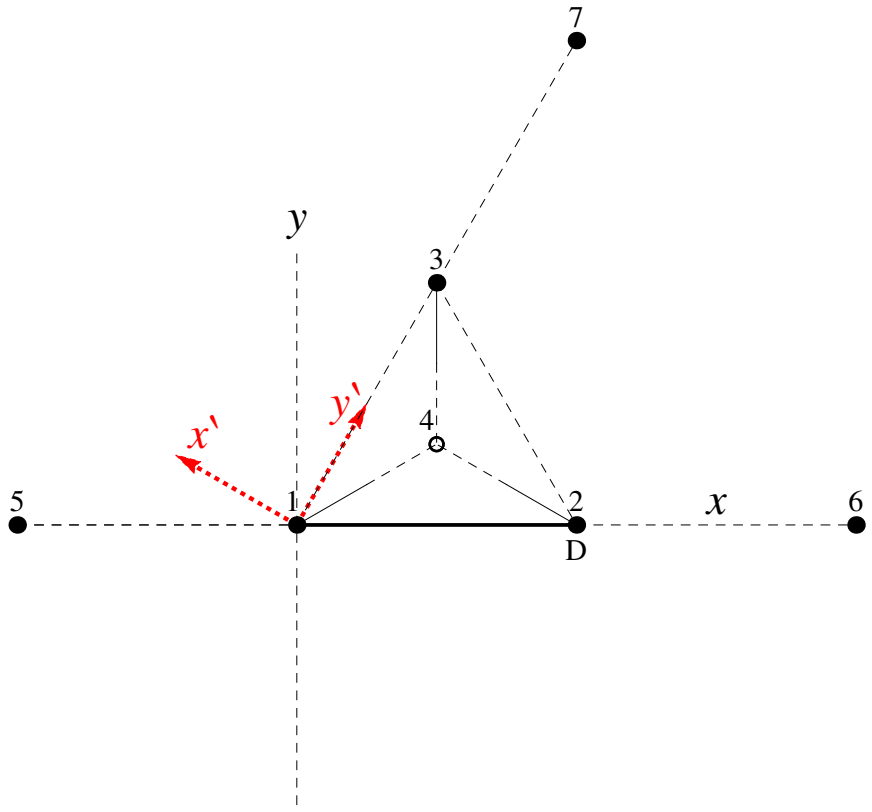

Figure 17: The plan view of ψ_6, after the second (final) step of transformation.

So,

$$\begin{aligned} \psi_6 &= R_\pi \circ R_T(\underline{x}_6)\hat{\psi}_I(\underline{x}) \qquad (64) \\ &= R_\pi \circ \hat{\psi}_I(x-2h, y) \\ &= \hat{\psi}_I(-x+2h, -y) \\ &= -3 + \frac{4}{h}x - \frac{1}{h^2}x^2 - \frac{1}{h^2}y^2. \qquad (65) \end{aligned}$$

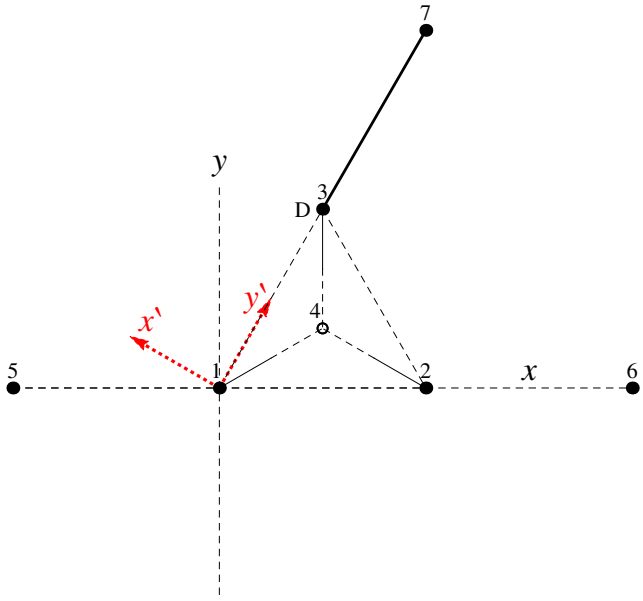

Figure 18: The plan view of the basis function ψ_7, before transformation.

To transform ψ_7 (see Figure 18) to $\hat{\psi}_I$ (see Figure 7), the first step is a translation of $x_7 = (h, \sqrt{3}h)$ (see Figure 19).

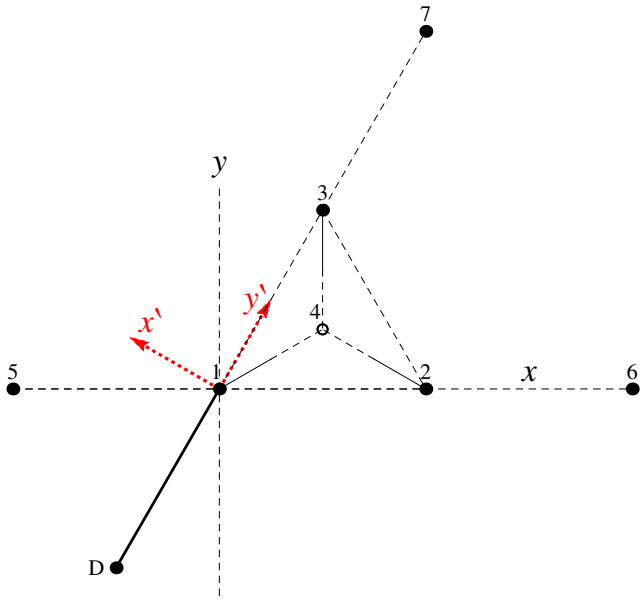

Figure 19: The plan view of ψ_7, after the first step of transformation.

The second (final) step in transforming ψ_7 to $\hat{\psi}_I$ is via a rotation of $2\pi/3$ (anti-clockwise) (see Figure 20).

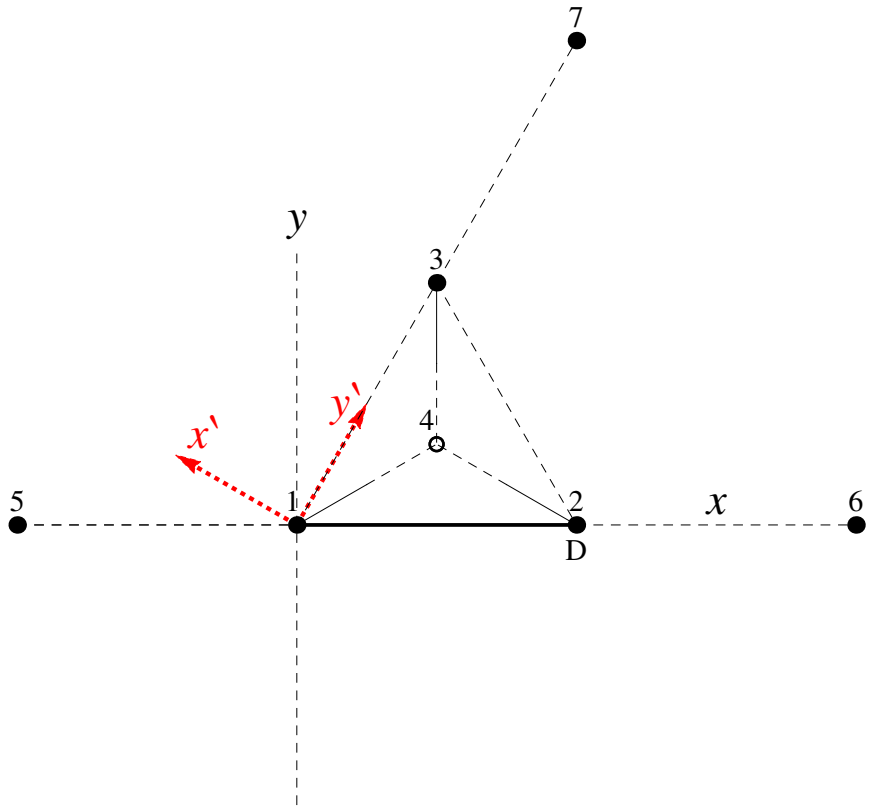

Figure 20: The plan view of ψ_7, after the second (final) step of transformation.

So,

$$\begin{aligned} \psi_7 &= R_{\frac{2\pi}{3}} \circ R_T(\underline{x}_7)\hat{\psi}_I(\underline{x}) && (66) \\ &= R_{\frac{2\pi}{3}} \circ \hat{\psi}_I(x-h, y-\sqrt{3}h) \\ &= -3 + \frac{2}{h}x + \frac{2\sqrt{3}}{h}y - \frac{1}{h^2}x^2 - \frac{1}{h^2}y^2. && (67) \end{aligned}$$

j	Related steps from ϕ_j and ψ_j to their respective canonical basis function		
	(1) Translation (R_T)	(2) Reflection (R_R)	(3) Rotation (R_θ)
1	–	–	$-\pi/6$
2	$(h, 0)$	y axis	$-\pi/6$
3	$(\frac{h}{2}, \frac{\sqrt{3}h}{2})$	–	$\pi/2$
4	–	–	–
5	$(-h, 0)$	–	–
6	$(2h, 0)$	–	π
7	$(h, \sqrt{3}h)$	–	$2\pi/3$

Table 1: The related steps of the transformation from ϕ_j, $j = 1, \ldots, 4$ and ψ_j, $j = 5, 6, 7$ to their respective canonical basis function in fractal generation level $n = 1$.

A summary of the transformations required for each basis function at fractal generation level $n = 1$ is given in Table 1. A table summarising the coefficients that subsequently arise for each basis function is given in Table 7 (see Appendix).

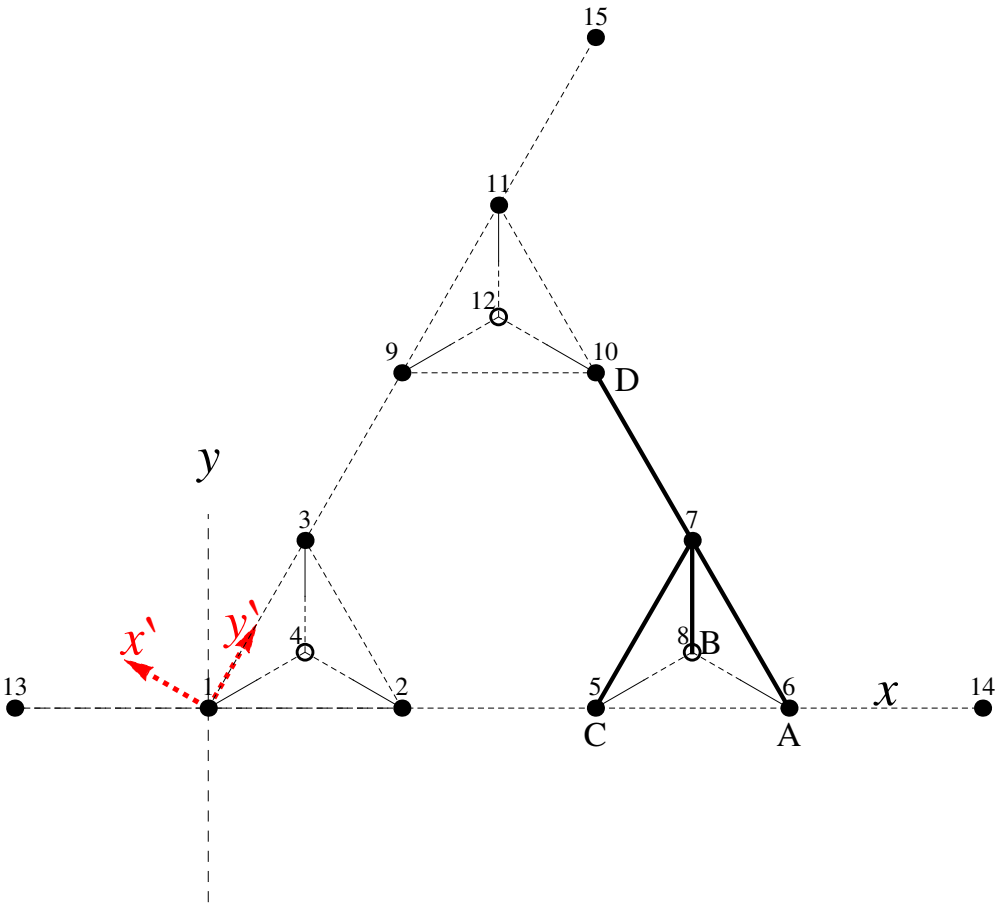

Figure 21: The plan view of the basis function $\phi_7 5$, before transformation.

The above process can then be repeated for fractal generation level $n = 2$. Recall that at each generation level the overall length of the lattice remains fixed (L) and the edge length h decreases. As such the canonical basis function given by equation (45) can still be applied here since it will be automatically scaled as its coefficients depend on h. For example, to transform ϕ_7 (see Figure 21) to $\hat{\phi}_J$ (see Figure 5), the first step is a translation of $x_7 = (5h/2, \sqrt{3}h/2)$ (see Figure 22).

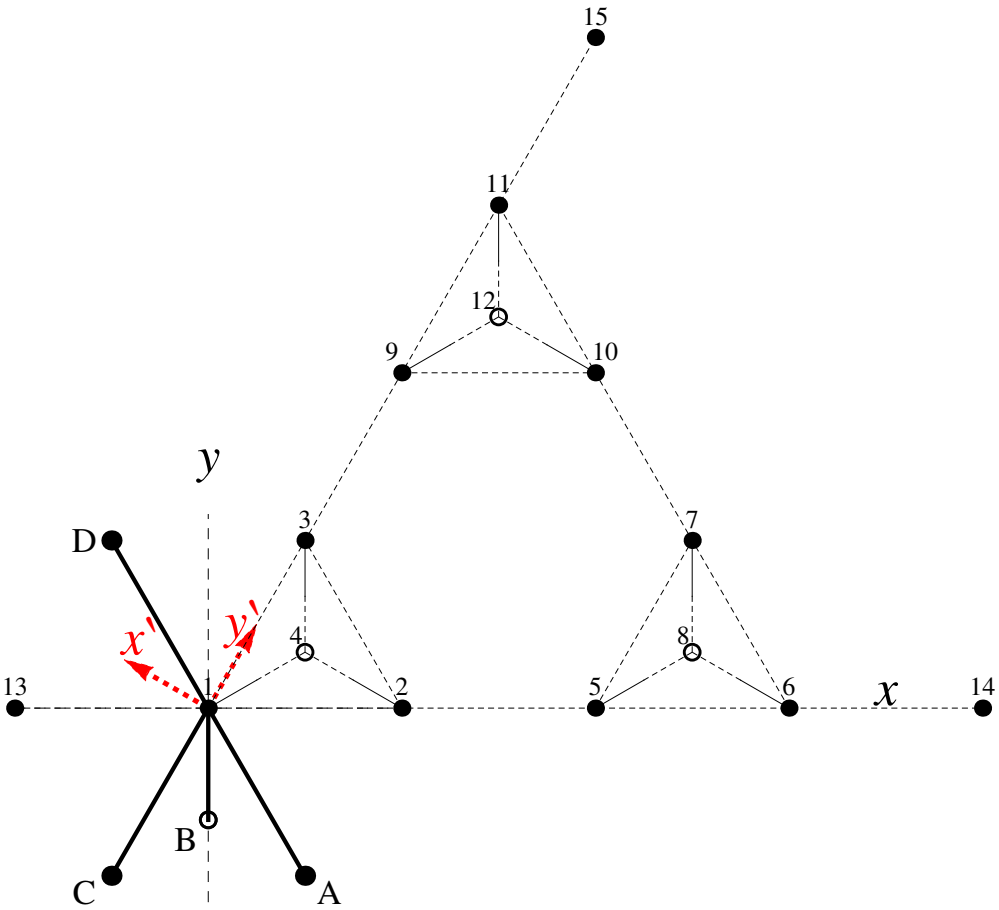

Figure 22: The plan view of ϕ_7, after the first transformation.

The second step in transforming ϕ_7 to $\hat{\phi}_J$ is via a reflection in the y axis (see Figure 23).

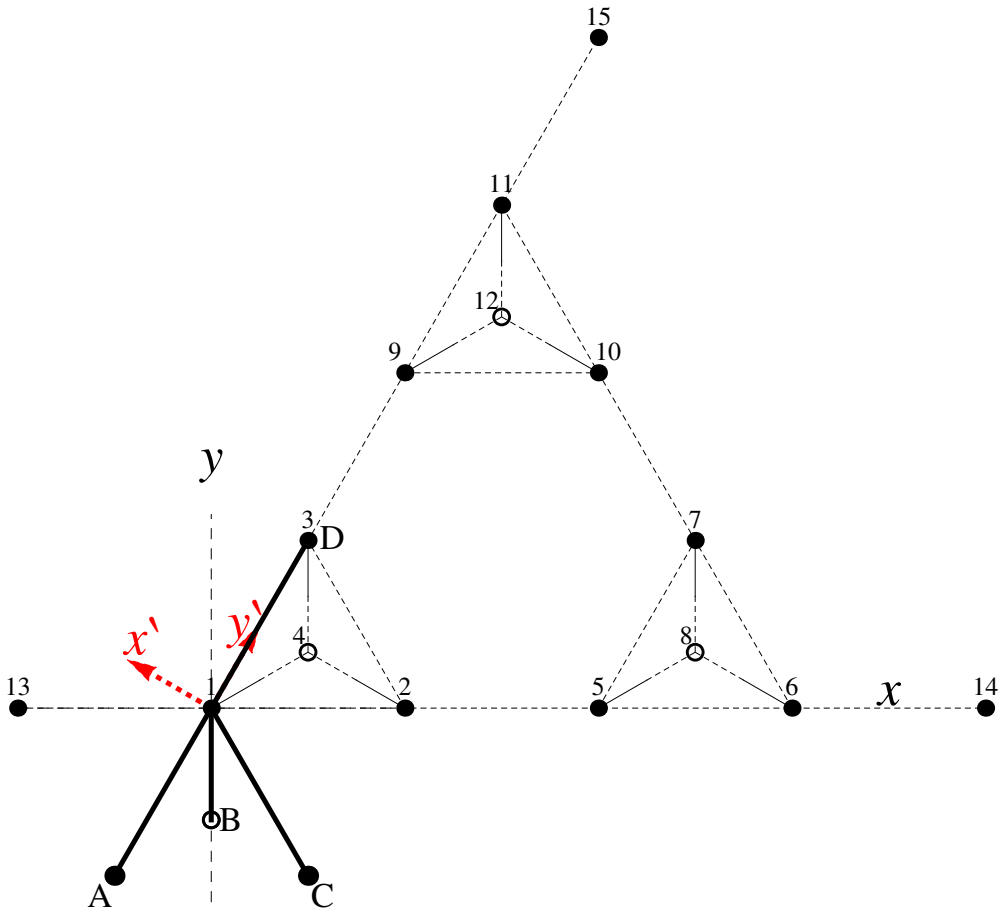

Figure 23: The plan view of ϕ_7, after the second transformation.

Then from this plan view of ϕ_7, the third (final) step in transforming ϕ_7 to $\hat{\phi}_J$ is via a rotation of $\pi/2$ (anticlockwise) (see Figure 24).

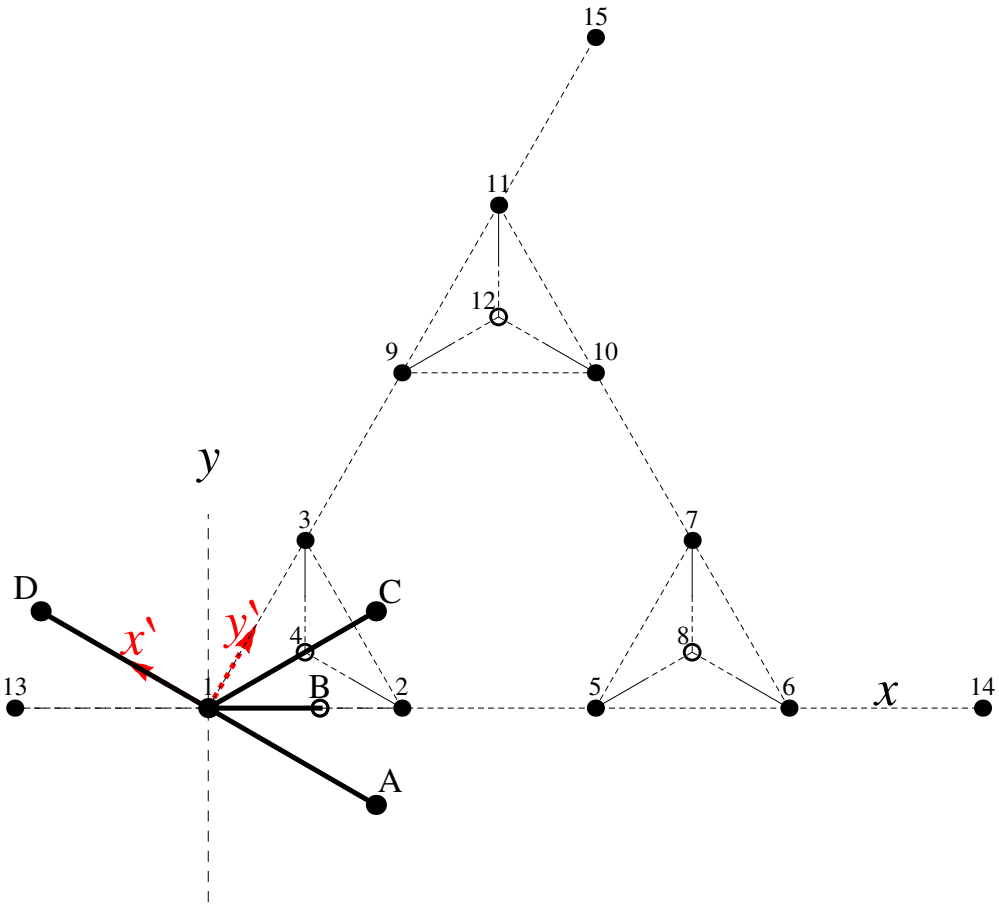

Figure 24: The plan view of ϕ_7, after the third (final) transformation.

So,

$$\begin{aligned}
\phi_7 &= R_{\frac{\pi}{2}} \circ R_R \circ R_T(\underline{x}_7)\hat{\phi}_J(\underline{x}) && (68)\\
&= R_{\frac{\pi}{2}} \circ R_R \hat{\phi}_J\big(x - \frac{5h}{2}, y - \frac{\sqrt{3}h}{2}\big)\\
&= R_{\frac{\pi}{2}} \hat{\phi}_J\big(-x + \frac{5h}{2}, y - \frac{\sqrt{3}h}{2}\big)\\
&= \hat{\phi}_J\big(-y + \frac{\sqrt{3}h}{2}, -x + \frac{5h}{2}\big)\\
&= 30 - \frac{25}{h}x + \frac{3\sqrt{3}}{h}y + \frac{5}{h^2}x^2 - \frac{3}{h^2}y^2. && (69)
\end{aligned}$$

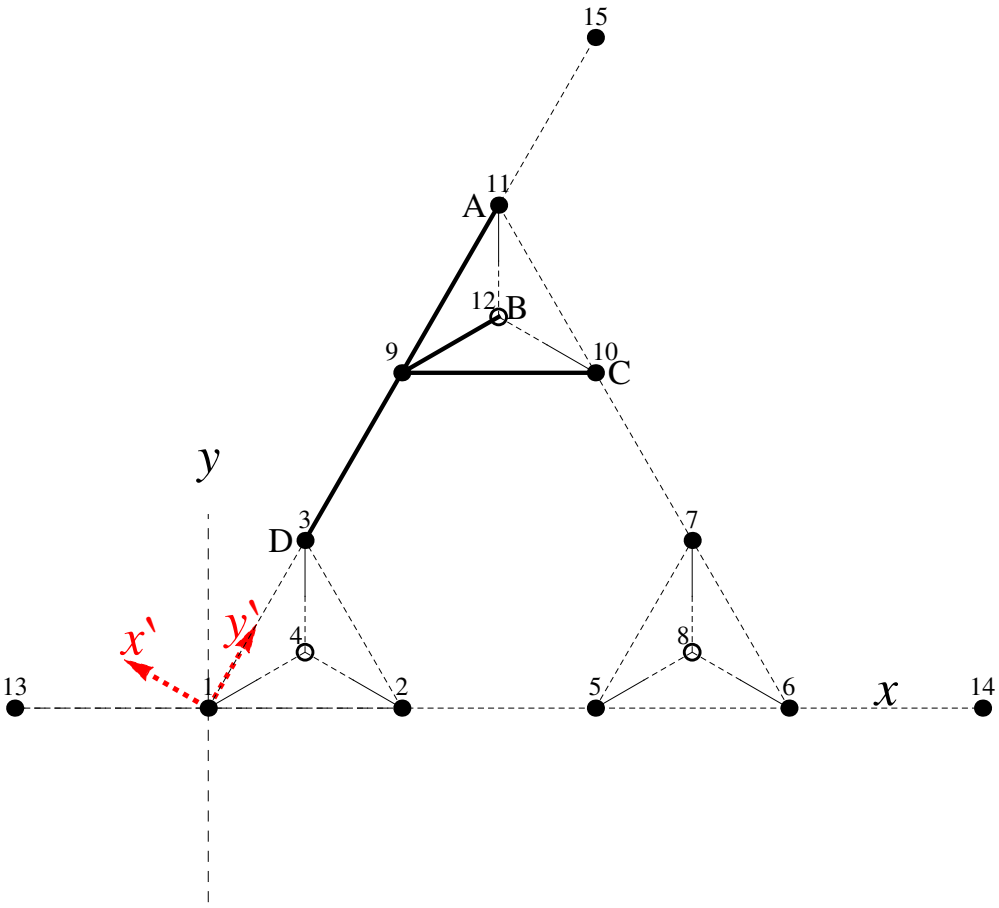

Figure 25: The plan view of the basis function ϕ_9, before transformation.

To transform ϕ_9 (see Figure 25) to $\hat{\phi}_J$ (see Figure 5) the first step is a translation of $x_9 = (h, \sqrt{3}h)$ (see Figure 26).

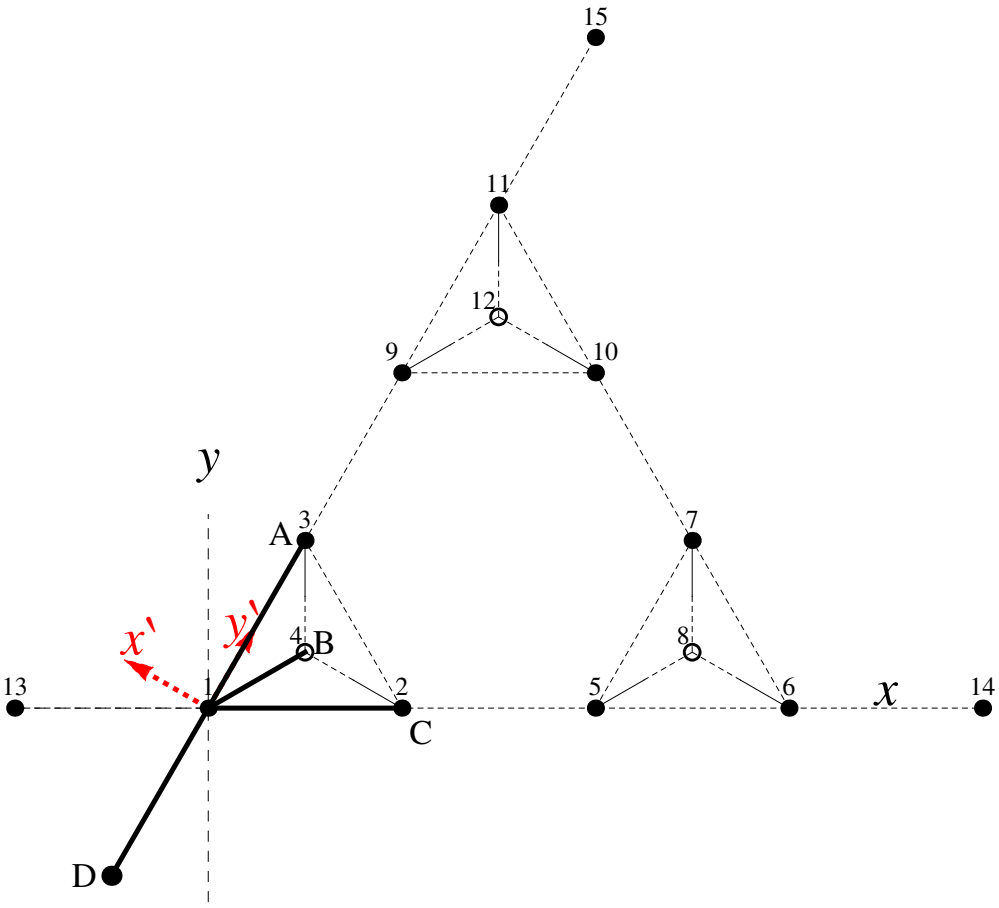

Figure 26: The plan view of ϕ_9, after the first transformation.

The second related step is a reflection in the (y axis) (see Figure 27).

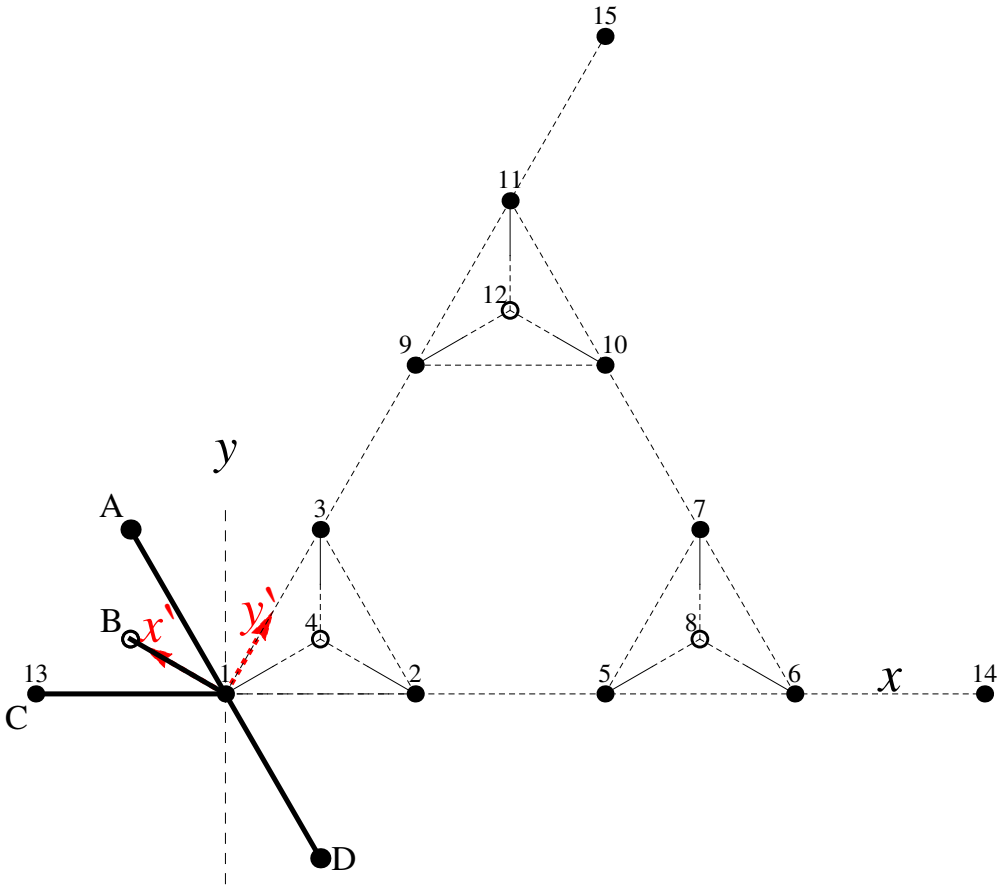

Figure 27: The plan view of ϕ_9, after the second transformation.

Then from this plan view of ϕ_9, the third (final) step is a rotation of $-5\pi/6$ (clockwise) (see Figure 28).

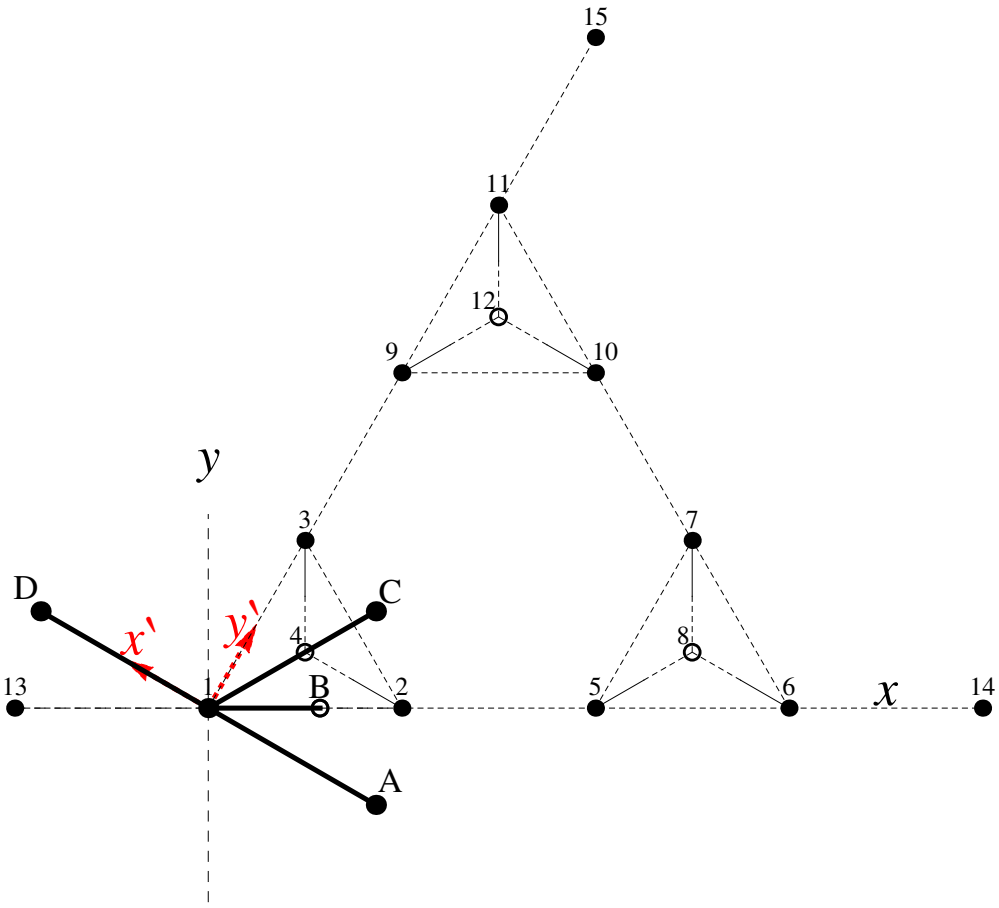

Figure 28: The plan view of ϕ_9, after the third (final) transformation.

Hence,

$$\begin{aligned}
\phi_9 &= R_{\frac{-5\pi}{6}} \circ R_R \circ R_T(\underline{x}_9)\hat{\phi}_J(\underline{x}) && (70)\\
&= R_{\frac{-5\pi}{6}} \circ R_R \hat{\phi}_J(x-h, y-\sqrt{3}h)\\
&= R_{\frac{-5\pi}{6}} \hat{\phi}_J(-x+h, y-\sqrt{3}h)\\
&= \hat{\phi}_J\big(\frac{\sqrt{3}}{2}x - \frac{\sqrt{3}h}{2} + \frac{1}{2}y - \frac{\sqrt{3}h}{2}, \frac{1}{2}x - \frac{h}{2} - \frac{\sqrt{3}}{2}y + \frac{3h}{2}\big)\\
&= 1 - \frac{3}{h^2}\big(\frac{\sqrt{3}}{2}x + \frac{1}{2}y - \sqrt{3}h\big)^2 + \frac{5}{h^2}\big(\frac{1}{2}x - \frac{\sqrt{3}}{2}y + h\big)^2\\
&= -3 + \frac{14}{h}x - \frac{2\sqrt{3}}{h}y - \frac{1}{h^2}x^2 + \frac{3}{h^2}y^2 - \frac{4\sqrt{3}}{h^2}xy. && (71)
\end{aligned}$$

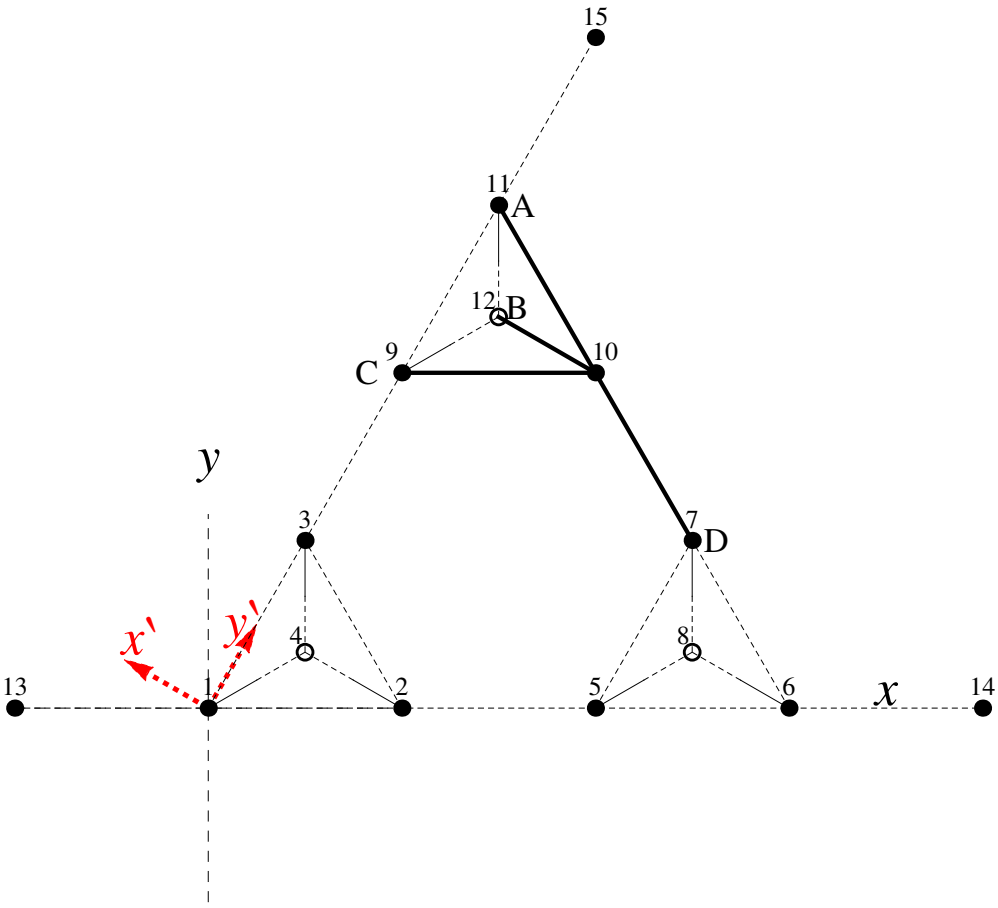

Figure 29: The plan view of the basis function ϕ_{10}, before transformation.

To transform ϕ_{10} (see Figure 29) to $\hat{\phi}_J$ (see Figure 5) the first step is a translation of $x_{10} = (2h, \sqrt{3}h)$ (see Figure 30).

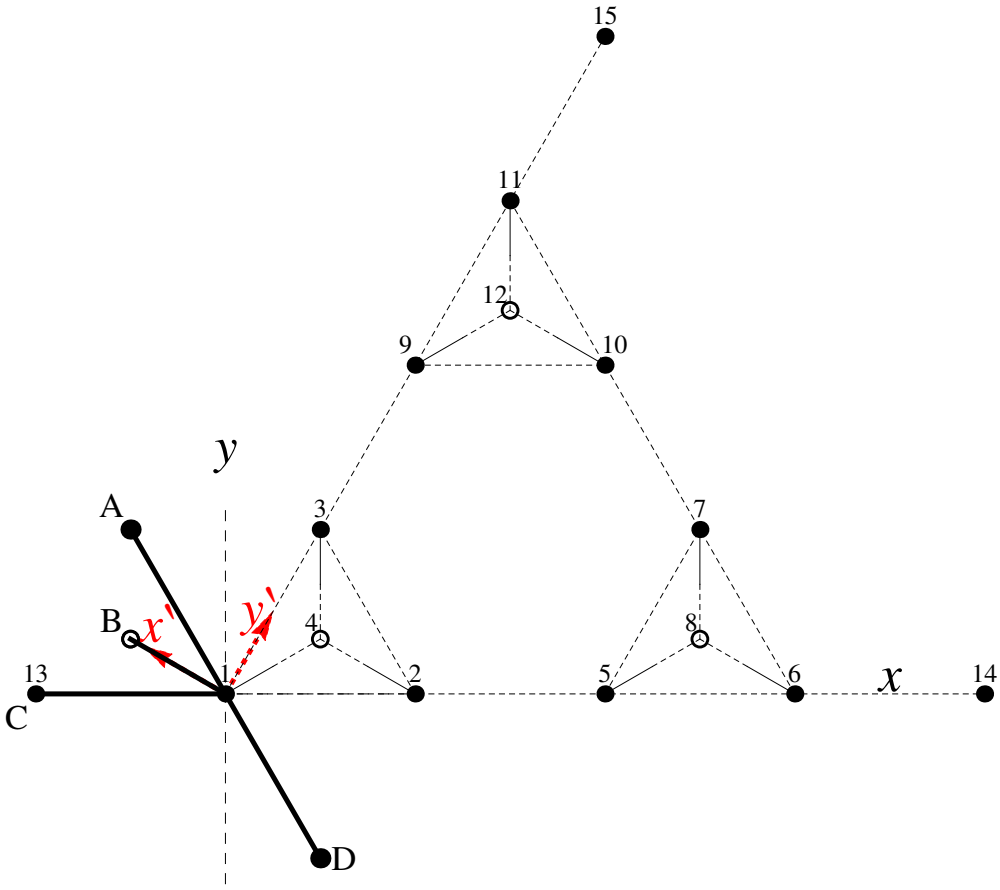

Figure 30: The plan view of ϕ_{10}, after the first transformation.

The second (final) step is a rotation of $-5\pi/6$ (clockwise) (see Figure 31).

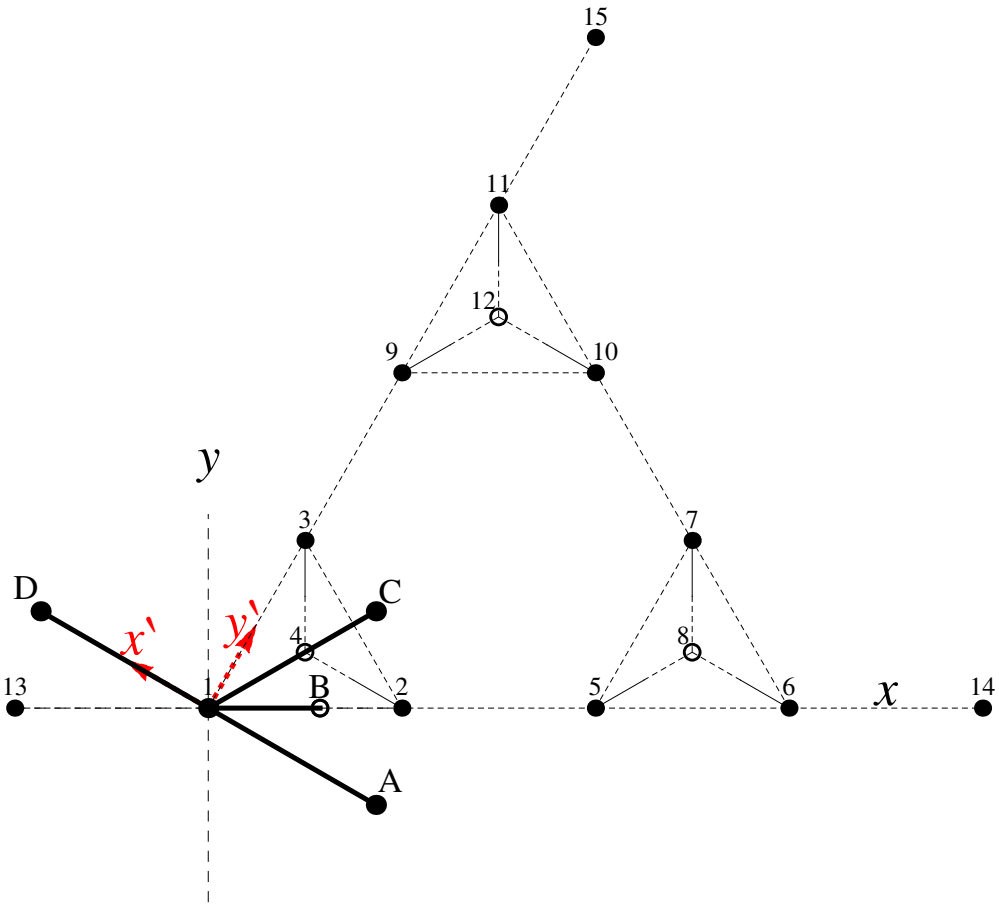

Figure 31: The plan view of ϕ_{10}, after the second (final) transformation.

So,

$$\begin{aligned}
\phi_{10} &= R_{\frac{-5\pi}{6}} \circ R_T(\underline{x}_{10})\hat{\phi}_J(\underline{x}) && (72)\\
&= R_{\frac{-5\pi}{6}} \circ \hat{\phi}_J(x-2h, y-\sqrt{3}h)\\
&= \hat{\phi}_J(-\frac{\sqrt{3}}{2}x + \sqrt{3}h + \frac{y}{2} - \frac{\sqrt{3}h}{2}, -\frac{1}{2}x + h - \frac{\sqrt{3}}{2}y + \frac{3h}{2})\\
&= 1 - \frac{3}{h^2}\big(-\frac{\sqrt{3}}{2}x + \frac{1}{2}y + \frac{\sqrt{3}h}{2}\big)^2 + \frac{5}{h^2}\big(-\frac{1}{2}x - \frac{\sqrt{3}}{2}y + \frac{5h}{2}\big)^2\\
&= 30 - \frac{8}{h}x - \frac{14\sqrt{3}}{h}y - \frac{1}{h^2}x^2 + \frac{3}{h^2}y^2 + \frac{4\sqrt{3}}{h^2}xy. && (73)
\end{aligned}$$

j	Related steps from ϕ_j and ψ_j to their respective canonical basis function		
	(1) Translation (R_T)	(2) Reflection (R_R)	(3) Rotation (R_θ)
1	–	–	$-\pi/6$
2	$\lambda(h, 0)$	y axis	$-\pi/6$
3	$\lambda(\frac{h}{2}, \frac{\sqrt{3}h}{2})$	–	$\pi/2$
4	–	–	–
5	$\lambda(2h, 0)$	–	$-\pi/6$
6	$\lambda(3h, 0)$	y axis	$-\pi/6$
7	$\lambda(\frac{5h}{2}, \frac{\sqrt{3}h}{2})$	y axis	$\pi/2$
8	$\lambda(\frac{5h}{2}, \frac{h}{2\sqrt{3}})$	–	–
9	$\lambda(h, \sqrt{3}h)$	y axis	$-5\pi/6$
10	$\lambda(2h, \sqrt{3}h)$	–	$-5\pi/6$
11	$\lambda(\frac{3h}{2}, \frac{3\sqrt{3}h}{2})$	–	$\pi/2$
12	$\lambda(\frac{3h}{2}, \frac{7h}{2\sqrt{3}})$	–	–
13	$\lambda(-h, 0)$	–	–
14	$\lambda(4h, 0)$	–	π
15	$\lambda(2h, 2\sqrt{3}h)$	–	$2\pi/3$

Table 2: The related steps of the transformation from ϕ_j, $j = 1, \ldots, 12$ and ψ_j, $j = 13, 14, 15$ to their respective canonical basis function in fractal generation level $n = 2$, where $\lambda = 1/3$.

A table showing all the transformations required to create the basis functions, for fractal generation level $n = 2$, is shown in Table 2. Another table showing the coefficients that arise from this process for each basis function is given in Table 8

(see Appendix). To aid in the visualisation of these basis functions an example is provided in the graph below, which shows the lattice basis functions ϕ_j where $j = 1, 2$ and 3, which are the interior PZT-5H nodes at fractal generation level $n = 1$ (see Figure 3). The lattice basis functions ϕ_1 at vertex $(0, 0)$ (as shown in green in Figure 32) is connected to node 2 through element 1, node A through element 7, node 3 through element 3 and node 4 through element 4. The lattice basis functions ϕ_2 at vertex $(h, 0)$ (as shown in blue in Figure 32) is connected to node 1 through element 1, node B through element 8, node 3 through element 2 and node 4 through element 5. The lattice basis functions ϕ_3 at vertex $(h/2, \sqrt{3}h/2)$ (as shown in blue in Figure 32) is connected to node 1 through element 3, node 2 through element 2, node C through element 9, and node 4 through element 6.

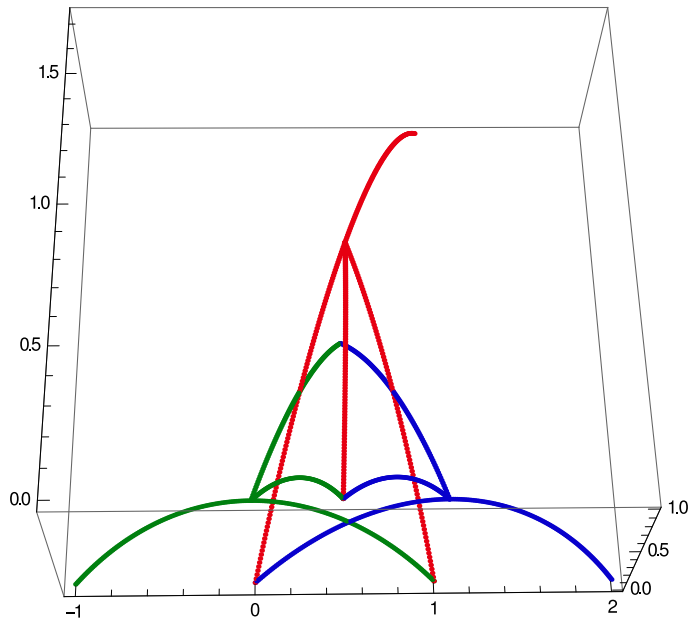

Figure 32: The basis functions ϕ_j where $j = 1, 2$ and 3 at fractal generation level $n = 1$.

The graph below shows the lattice basis functions ϕ_4 which is the interior polymer node at fractal generation level $n = 1$ (see Figure 3). The lattice basis functions ϕ_4 at vertex $(h/2, h/2\sqrt{3})$ (as shown at Figure 33) is connected to node 1 through element 4, node 2 through element 5 and node 3 through element 6.

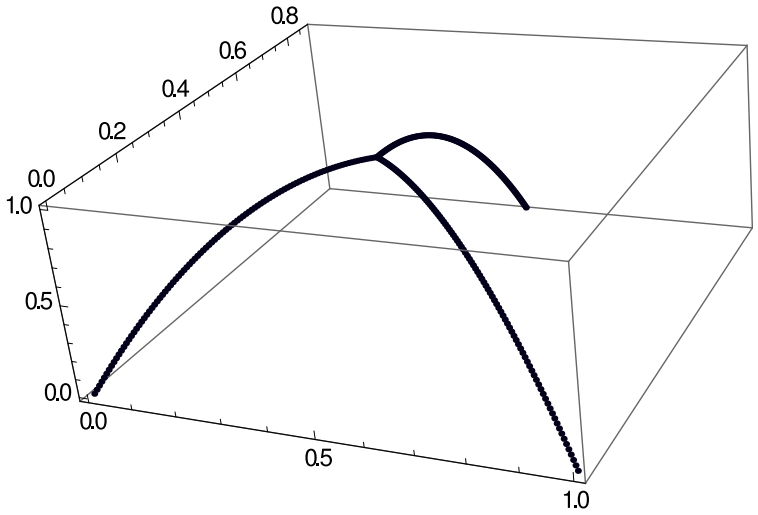

Figure 33: The basis function ϕ_4 at fractal generation level $n = 1$.

The graph below shows the lattice basis functions ψ_j where $j = 5, 6$ and 7 which are the exterior nodes at fractal generation level $n = 1$ (see Figure 3). The lattice basis functions ψ_5 at vertex $(-h, 0)$ (as shown in red in Figure 34) is connected to node 1 through element 7. The lattice basis functions ψ_6 at vertex $(2h, 0)$ (as shown in blue in Figure 34) is connected to node 2 through element 8. The lattice basis functions ψ_7 at vertex $(h, \sqrt{3}h)$ (as shown in green in Figure 34) is connected to node 3 through element 9.

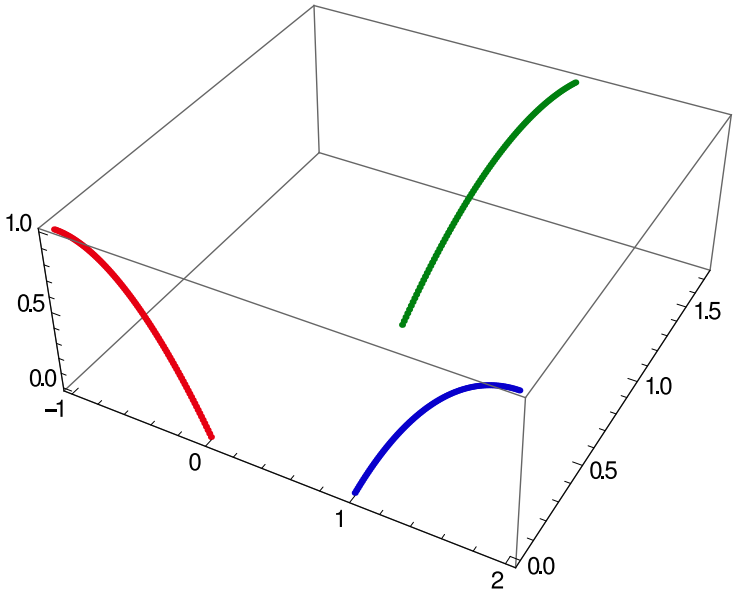

Figure 34: The basis functions ψ_j where $j = 5, 6$ and 7 at fractal generation level $n = 1$.

The graph below shows the lattice basis functions ϕ_j where $j = 1, 2$ and 3 which are some of the interior PZT-5H nodes at fractal generation level $n = 2$ (see Figure 4). The lattice basis functions ϕ_1 at vertex $(0, 0)$ (as shown in green in Figure 35) is connected to node 2 through element 1, node A (that is, node 13) through element 22, node 3 through element 3, and node 4 through element 4. The lattice basis functions ϕ_2 at vertex $(h, 0)$ (as shown in blue in Figure 35) is connected to node 1 through element 1, node 5 through element 7, node 3 through element 2, and node 4 through element 5. The lattice basis functions ϕ_3 at vertex $(h/2, \sqrt{3}h/2)$ (as shown in blue in Figure 35) is connected to node 1 through element 3, node 2 through element 2, node 9 through element 14, and node 4 through element 6.

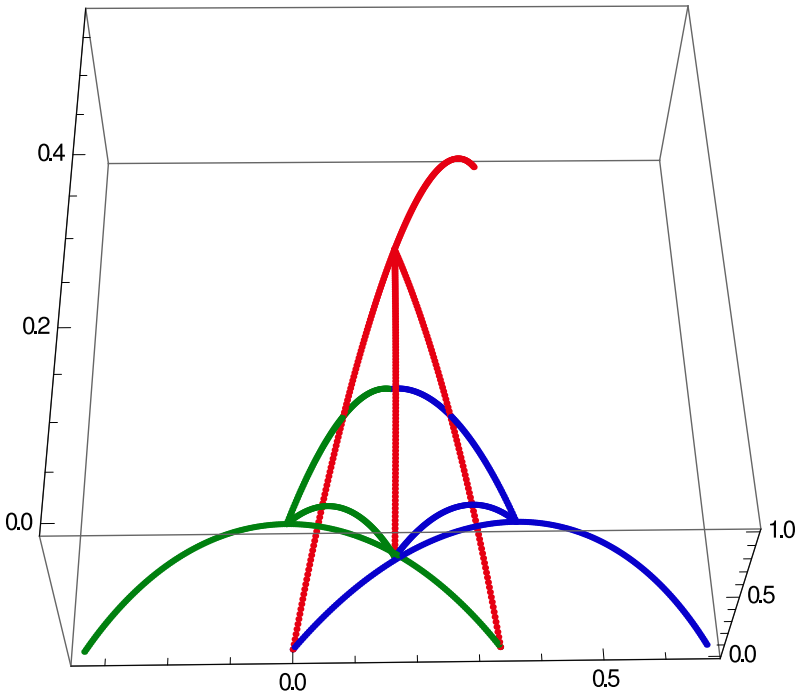

Figure 35: The basis functions ϕ_j where $j = 1, 2$ and 3 at fractal generation level $n = 2$.

The graph below shows the lattice basis functions ϕ_j where $j = 5, 6$ and 7 which are some of the interior PZT-5H nodes at fractal generation level $n = 2$ (see Figure 4). The lattice basis functions ϕ_5 at vertex $(2h, 0)$ (as shown in green in Figure 36) is connected to node 2 through element 7, node 6 through element 8, node 7 through element 10, and node 8 through element 11. The lattice basis functions ϕ_6 at vertex $(3h, 0)$ (as shown in blue in Figure 36) is connected to node 5 through element 8, node B (that is, node 14) through element 23, node 7 through element 9, and node 8 through element 12. The lattice basis functions ϕ_7 at vertex $(5h/2, \sqrt{3}h/2)$ (as shown in blue in Figure 36) is connected to node 5 through element 10, node 6 through element 9, node 10 through element 15, and node 8 through element 13.

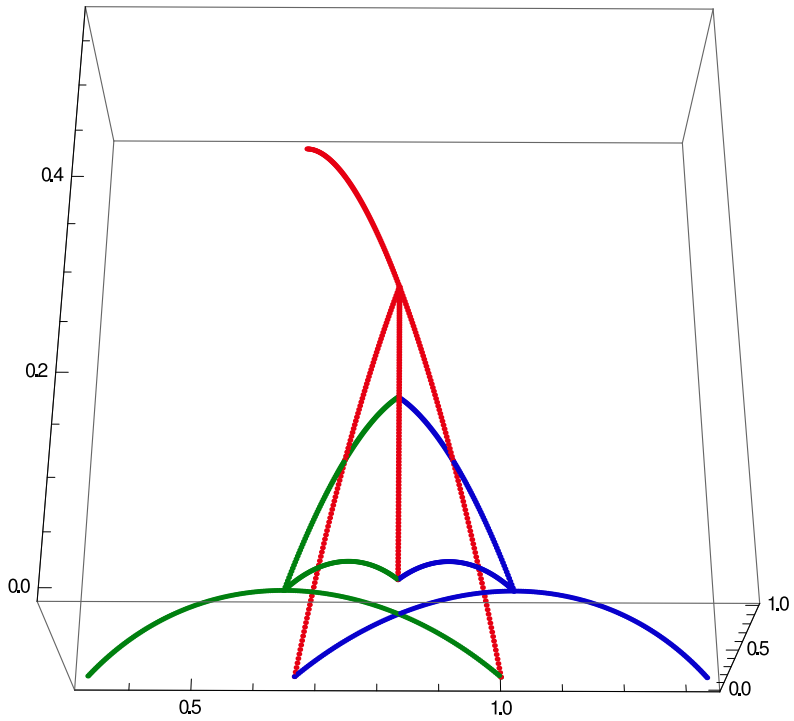

Figure 36: The basis functions ϕ_j where $j = 5, 6$ and 7 at fractal generation level $n = 2$.

The graph below shows the lattice basis functions ϕ_j where $j = 9, 10$ and 11 which are some of the interior PZT-5H nodes at fractal generation level $n = 2$ (see Figure 4). The lattice basis functions ϕ_9 at vertex $(h, \sqrt{3}h)$ (as shown in green in Figure 37) is connected to node 3 through element 14, node 10 through element 16, node 11 through element 18, and node 12 through element 19. The lattice basis functions ϕ_{10} at vertex $(2h, \sqrt{3}h)$ (as shown in blue in Figure 37) is connected to node 7 through element 15, node 9 through element 16, node 11 through element 17, and node 12 through element 20. The lattice basis functions ϕ_{11} at vertex $(3h/2, 3\sqrt{3}h/2)$ (as shown in blue in Figure 36) is connected to node 9 through element 18, node 10 through element 17, node C (that is, node 15) through element 24, and node 12 through element 21.

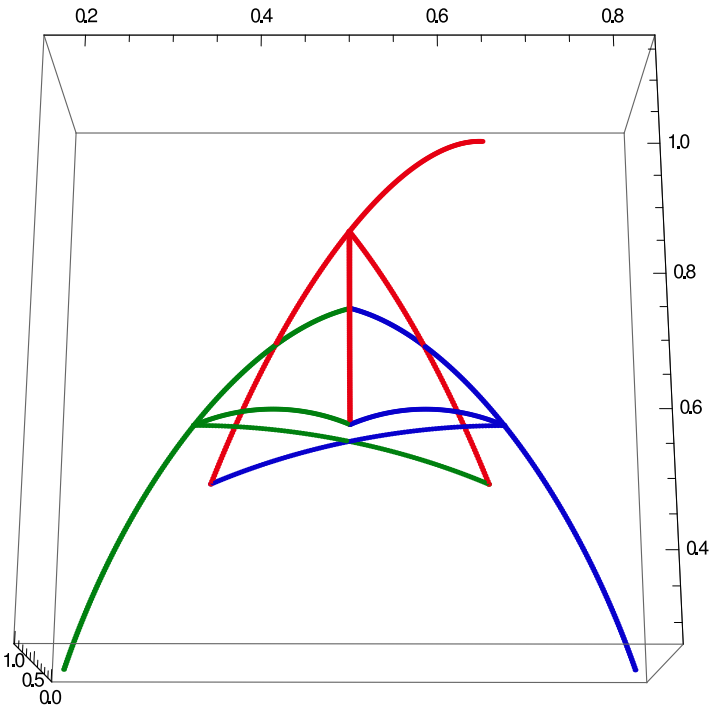

Figure 37: The basis functions ϕ_j where $j = 9, 10$ and 11 at fractal generation level $n = 2$.

The graph below shows the lattice basis functions ϕ_j where $j = 4, 8$ and 12 which are the interior polymer nodes at fractal generation level $n = 2$ (see Figure 4). The lattice basis functions ϕ_4 at vertex $(h/2, h/2\sqrt{3})$ (as shown in green in Figure 38) is connected to node 1 through element 4, node 2 through element 5 and node 3 through element 6. The lattice basis functions ϕ_8 at vertex $(5h/2, h/2\sqrt{3})$ (as shown in blue in Figure 38) is connected to node 5 through element 11, node 6 through element 12 and node 7 through element 13. The lattice basis functions ϕ_{12} at vertex $(3h/2, 7h/2\sqrt{3})$ (as shown in red in Figure 38) is connected to node 9 through element 19, node 10 through element 20 and node 11 through element 21.

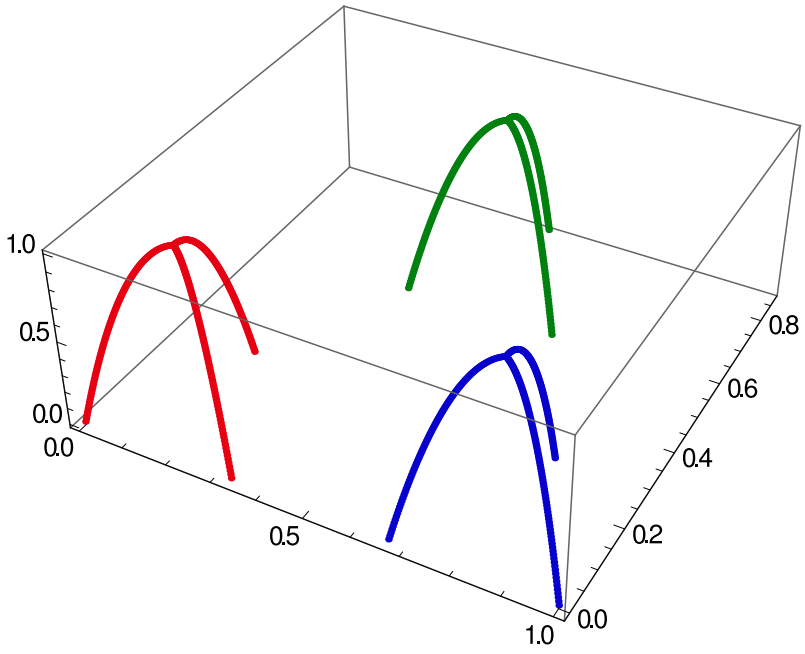

Figure 38: The basis functions ϕ_j where $j = 4, 8$ and 12 at fractal generation level $n = 2$.

The graph below shows the lattice basis functions ψ_j where $j = 13, 14$ and 15 which are the exterior nodes at fractal generation level $n = 2$ (see Figure 4). The lattice basis functions ψ_{13} at vertex $(-h, 0)$ (as shown in green in Figure 39) is connected to node 1 through element 22. The lattice basis functions ψ_{14} at vertex $(4h, 0)$ (as shown in blue in Figure 39) is connected to node 6 through element 23. The lattice basis functions ψ_{15} at vertex $(2h, 2\sqrt{3}h)$ (as shown in red in Figure 39) is connected to node 11 through element 24.

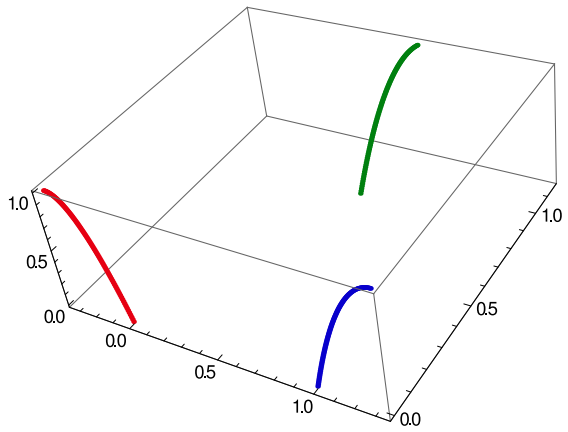

Figure 39: The basis functions ψ_j where $j = 13, 14$ and 15 at fractal generation level $n = 2$.

As described above each of the lattice basis functions is given by

$$\phi_j(x,y) = \begin{cases} a_j + b_j x + c_j y + d_j x^2 + f_j y^2 + g_j xy & j \in J \\ a_j + b_j x + c_j y + d_j (x^2 + y^2) & j \in K \end{cases} \tag{74}$$

and

$$\psi_j(x,y) = a_j + b_j x + c_j y + d_j (x^2 + y^2) \quad j \in I \tag{75}$$

where $(x, y) \in \Omega$ and a, b, c, d, f and $g \in \mathbb{R}$ are coefficients to be determined (see Tables 7 and 8 Appendix 11.1) and $J = \{1, 2, 3\}$ at $n = 1$, $J = \{1, 2, 3, 5, 6, 7, 9, 10, 11\}$ at $n = 2$ which are the interior PZT-5H nodes, $K = \{4\}$ at $n = 1$ and $K = \{4, 8, 12\}$ at $n = 2$ which are the polymer nodes and $I = \{5, 6, 7\}$ at $n = 1$, $I = \{13, 14, 15\}$ at $n = 2$ which are the exterior PZT-5H nodes. Hence

$$\nabla\phi_j(x,y) = \begin{cases} (b_j + 2d_j x + g_j y, c_j + 2f_j y + g_j x) & j \in J \\ (b_j + 2d_j x, c_j + 2d_j y) & j \in K \end{cases} \tag{76}$$

and

$$\nabla\psi_j(x,y) = (b_j + 2d_j x, c_j + 2e_j y) \quad j \in I. \tag{77}$$

For each element (edge) e where $e \in M_J$ (which is the set of elements in the interior that are piezoelectric), for ${}^{e}H_{ji}^{(n)}$ where $j, i \in \{1, 2, \ldots, N, N+1\}$ we can write equation (36) using equation (74) as

$$\begin{aligned}
{}^{M_J}H_{ji}^{(n)} &= \int_e \Big((a_j + b_j x + c_j y + d_j x^2 + f_j y^2 + g_j xy) \\
&\quad .(a_i + b_i x + c_i y + d_i x^2 + f_i y^2 + g_i xy) \Big) d\underline{x} \\
&= \int_e \Big(a_j a_i + (a_j b_i + a_i b_j)x + (a_j c_i + a_i c_j)y + (a_j d_i + a_i d_j + b_j b_i)x^2 \\
&\quad + (a_j f_i + a_i f_j + c_j c_i)y^2 + (a_j g_i + a_i g_j + b_j c_i + b_i c_j)xy + (b_j d_i + \\
&\quad b_i d_j)x^3 + (c_j f_i + c_i f_j)y^3 + (b_j f_i + b_i f_j + c_j g_i + c_i g_j)xy^2 + (b_j g_i + \\
&\quad b_i g_j + c_j d_i + c_i d_j)x^2 y + (f_j g_i + f_i g_j)xy^3 + (d_j g_i + d_i g_j)x^3 y + (d_j f_i \\
&\quad + d_i f_j + g_j g_i)x^2 y^2 + d_j d_i x^4 + f_j f_j y^4 \Big) d\underline{x}. \qquad (78)
\end{aligned}$$

Similarly, for each element (edge) e where $e \in M_K$ (which is the set of elements in the interior that are a polymer - piezoelectric mix), then

$$\begin{aligned}
{}^{M_K}H_{ji}^{(n)} &= \int_e \Big(\big(a_j + b_j x + c_j y + d_j x^2 + f_j y^2 + g_j xy\big).\big(a_i + b_i x + c_i y + \\
&\quad d_i(x^2 + y^2)\big) \Big) d\underline{x} \\
&= \int_e \Big(a_j a_i + (a_j b_i + a_i b_j)x + (a_j c_i + a_i c_j)y + (b_i b_j + a_j d_i + a_i d_j)x^2 \\
&\quad + (c_i c_j + a_j d_i + a_i f_j)y^2 + (b_i c_j + b_j c_i + a_i g_j)xy + (b_j d_i + b_i d_j)x^3 + \\
&\quad (c_j d_i + c_i f_j)y^3 + (b_j d_i + b_i f_j + c_i g_j)xy^2 + (c_j d_i + c_i d_j + b_i g_j)x^2 y + \\
&\quad d_i g_j xy^3 + d_i g_j x^3 y + (d_i d_j + d_i f_j)x^2 y^2 + d_i d_j x^4 + d_i f_j y^4 \Big) d\underline{x}. \qquad (79)
\end{aligned}$$

For the boundary elements $e \in M_I$ (which is the set of elements that connect to the exterior) note that ${}^{M_I}H_{ii}^{(n)} = {}^{M_J}H_{ii}^{(n)}$ where $i \in J$ (corner vertices). For a piezoelectric element lying between vertex p and vertex q the isoparametric representation, given by

$$\Big(x(s), y(s)\Big) = \Big((x_j - x_i)s + x_i, (y_j - y_i)s + y_i\Big) \qquad (80)$$

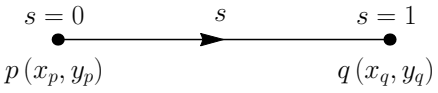

Figure 40: An isoparametric element (edge) between piezoelectric vertices $p\,(x_p, y_p)$ and $q\,(x_q, y_q)$.

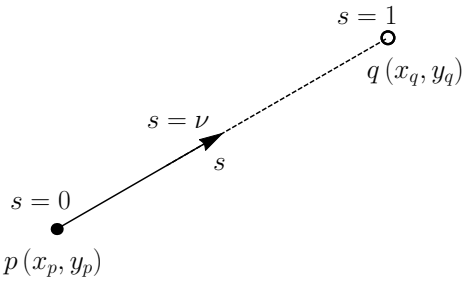

Figure 41: An isoparametric element (edge) between piezoelectric vertex $p\,(x_p, y_p)$ and polymer vertex $q\,(x_q, y_q)$. The fraction of piezoelectric material in this edge is given by ν.

is employed, where $s = 0$ and $s = 1$ and $d\underline{x} = h\,ds$ (see Figure 40). For the elements that join a piezoelectric node to a polymer node a similar representation is used but here $d\underline{x} = h/\sqrt{3}\,ds$ and the region between $s = 0$ and $s = \nu$ is piezoelectric and that between $s = \nu$ and $s = 1$ is polymer (see Figure 41). Substituting this into equations (78) and (79) gives

$$H_{ji}^{(n)} = \begin{cases} h \int_0^1 \phi_j \phi_i \, ds & \text{if } e \in M_J \\ \frac{h}{\sqrt{3}} \int_0^1 \phi_j \phi_i \, ds & \text{if } e \in M_K \\ h \int_0^1 \phi_j \phi_i \, ds & \text{if } e \in M_I. \end{cases} \tag{81}$$

Let us start with an interior piezoelectric element ($e \in M_J$), say $e = 1 \in M_J$ which is connected between node 1 at $(x_i, y_j) = (0, 0)$ and node 2 at $(x_j, y_j) = (h, 0)$. From equation (80) we get $(x(s), y(s)) = (hs, 0)$ and then from equation

(81) we get

$$
\begin{aligned}
{}^{e=1}H_{11}^{(1)} &= h\int_0^1 \phi_1(hs,0)\phi_1(hs,0)\,ds && (82)\\
&= h\int_0^1 \left(1-s^2\right)^2 ds. && (83)
\end{aligned}
$$

Similarly,

$$
\begin{aligned}
{}^{e=1}H_{12}^{(1)} &= h\int_0^1 \phi_1(hs,0)\phi_2(hs,0)\,ds && (84)\\
&= h\int_0^1 \left(1-s^2\right)\left(2s-s^2\right) ds\\
&= h\int_0^1 \left(1-s^2\right)\left(2-s\right)s\,ds, && (85)
\end{aligned}
$$

where we note that ${}^{e=1}H_{21}^{(1)} = {}^{e=1}H_{12}^{(1)}$. Also

$$
\begin{aligned}
{}^{e=1}H_{22}^{(1)} &= h\int_0^1 \phi_2(hs,0)\phi_2(hs,0)\,ds && (86)\\
&= h\int_0^1 \left(2s-s^2\right)^2 ds\\
&= h\int_0^1 \left(2-s\right)^2 s^2\,ds. && (87)
\end{aligned}
$$

So for each interior piezoelectric element ($e \in M_J$),

$$
{}^{M_J}H_{ji}^{(n)} = h\begin{cases}
\int_0^1 (s^2-1)^2\,ds & \text{if } j=i=p\\
\int_0^1 (s^2-1)(s-2)s\,ds & \text{if } (j=p \text{ and } i=q) \text{ or } (j=q \text{ and } i=p)\\
\int_0^1 (s-2)^2 s^2\,ds & \text{if } j=i=q\\
0 & \text{otherwise,}
\end{cases} \qquad (88)
$$

where element e connects node p to node q. Evaluating these integrals gives

$$
{}^{M_J}H_{ji}^{(n)} = \frac{h}{30}\begin{cases}
16 & \text{if } j=i=p\\
11 & \text{if } (j=p \text{ and } i=q) \text{ or } (j=q \text{ and } i=p)\\
16 & \text{if } j=i=q\\
0 & \text{otherwise.}
\end{cases} \qquad (89)
$$

For a piezoelectric - polymer element ($e \in M_K$), let us take the example $e = 5 \in M_K$ which is connected between node 2 at $(x_i, y_j) = (h, 0)$ and node 4 at $(x_j, y_j) = (h/2, h/(2\sqrt{3}))$. From equation (80) we get $(x(s), y(s)) = (-h/2s + h, h/(2\sqrt{3})s)$ and then from equation (81) we get

$$
\begin{aligned}
{}^{e=5}H^{(1)}_{22} &= \frac{h}{\sqrt{3}} \int_0^1 \phi_2(\frac{-h}{2}s + h, \frac{h}{2\sqrt{3}}s)\phi_2(\frac{-h}{2}s + h, \frac{h}{2\sqrt{3}}s)\, ds \qquad (90)\\
&= \frac{h}{\sqrt{3}} \int_0^1 \big(1 - s^2\big)^2\, ds. \qquad (91)
\end{aligned}
$$

Similarly,

$$
\begin{aligned}
{}^{e=5}H^{(1)}_{24} &= \frac{h}{\sqrt{3}} \int_0^1 \phi_2(\frac{-h}{2}s + h, \frac{h}{2\sqrt{3}}s)\phi_4(\frac{-h}{2}s + h, \frac{h}{2\sqrt{3}}s)\, ds \qquad (92)\\
&= \frac{h}{\sqrt{3}} \int_0^1 \big(1 - s^2\big)\big(2 - s\big)s\, ds. \qquad (93)
\end{aligned}
$$

where we note that ${}^{e=5}H^{(1)}_{42} = {}^{e=5}H^{(1)}_{24}$. Also

$$
\begin{aligned}
{}^{e=5}H^{(1)}_{44} &= \frac{h}{\sqrt{3}} \int_0^1 \phi_4(\frac{-h}{2}s + h, \frac{h}{2\sqrt{3}}s)\phi_4(\frac{-h}{2}s + h, \frac{h}{2\sqrt{3}}s)\, ds \qquad (94)\\
&= \frac{h}{\sqrt{3}} \int_0^1 \big(2 - s\big)^2 s^2\, ds. \qquad (95)
\end{aligned}
$$

So, for each piezoelectric - polymer element ($e \in M_K$),

$$
{}^{M_K}H^{(n)}_{ji} = \frac{h}{\sqrt{3}} \begin{cases} \int_0^1 (s^2 - 1)^2\, ds & \text{if } j = i = p \\ \int_0^1 (s^2 - 1)(s - 2)s\, ds & \text{if } (j = p \text{ and } i = q) \text{ or } (j = q \text{ and } i = p) \\ \int_0^1 (s - 2)^2 s^2\, ds & \text{if } j = i = q \\ 0 & \text{otherwise.} \end{cases} \qquad (96)
$$

That is

$$
{}^{M_K}H^{(n)}_{ji} = \frac{h}{30\sqrt{3}} \begin{cases} 16 & \text{if } j = i = p \\ 11 & \text{if } (j = p \text{ and } i = q) \text{ or } (j = q \text{ and } i = p) \\ 16 & \text{if } j = i = q \\ 0 & \text{otherwise.} \end{cases} \qquad (97)
$$

Note that from equation (35) since ${}^{M_K}H_{ji}^{(n)} = h/\sqrt{3}\big(\int_0^\nu \phi_j\phi_i\,dx + \int_\nu^1 \phi_j\phi_i\,dx\big) = h/\sqrt{3}\int_0^1 \phi_j\phi_i\,dx$, then ν does not explicitly appear. We will see later that for $c^2K_{ji}^{(n)}$ for $e \in M_K$, we need to apply equation (23) where ${}^{M_K}c^2K_{ji}^{(n)} = h/\sqrt{3}\big(c_T^2\int_0^\nu \nabla\phi_j.\nabla\phi_i\,ds + c_P^2\int_\nu^1 \nabla\phi_j.\nabla\phi_i\,ds\big)$ and so ν does appear explicitly in that case. For exterior piezoelectric elements ($e \in M_I = \{M+1, M+2, M+3\}$), let us take the example for one element that is $e = 7 \in M_I$ which is connected between node 1 at $(x_i, y_j) = (0, 0)$ and node 5 at $(x_j, y_j) = (-h, 0)$ and apply equation (80) to get $(x(s), y(s)) = (hs, 0)$. Then from equation (81) we get

$$
\begin{aligned}
{}^{e=7}H_{11}^{(1)} &= h\int_0^1 \phi_1(hs,0)\phi_1(hs,0)\,ds && (98)\\
&= h\int_0^1 \big(1-s^2\big)^2\,ds. && (99)
\end{aligned}
$$

Similarly, for each exterior piezoelectric element ($e \in M_I$),

$${}^{M_I}H_{ji}^{(n)} = h\begin{cases} \int_0^1 (s^2-1)^2\,ds & \text{if } j = i = q \\ 0 & \text{otherwise.} \end{cases} \qquad (100)$$

Note that there is only one combination of basis functions in these exterior piezoelectric elements since the left hand side of equation (31) does not involve the basis functions at boundary vertices I denoted by ψ_I. That is

$${}^{M_I}H_{ji}^{(n)} = \frac{h}{30}\begin{cases} 16 & \text{if } j = i = q \\ 0 & \text{otherwise} \end{cases} \qquad (101)$$

where q is the corner vertex of the $SG(3,4)$ lattice connected to element e (for $n = 1$, $q \in \{1, 2, 3\}$, and for $n = 2$, $q \in \{1, 6, 11\}$). Assembling the full matrix

in equation (36) gives, for generation level $n = 1$

$$H_{ji}^{(1)} = \frac{h}{30}\begin{bmatrix} 48+\frac{16}{\sqrt{3}} & 11 & 11 & \frac{11}{\sqrt{3}} \\ 11 & 48+\frac{16}{\sqrt{3}} & 11 & \frac{11}{\sqrt{3}} \\ 11 & 11 & 48+\frac{16}{\sqrt{3}} & \frac{11}{\sqrt{3}} \\ \frac{11}{\sqrt{3}} & \frac{11}{\sqrt{3}} & \frac{11}{\sqrt{3}} & \frac{48}{\sqrt{3}} \end{bmatrix} = \frac{h}{30}\hat{H}_{ji}^{(1)}, \tag{102}$$

and for generation level $n = 2$

$$H_{ji}^{(2)} = \frac{h}{30}\begin{bmatrix} & & & & 0 & 0 & 0 & 0 & 0 & 0 & 0 & 0 \\ & & \hat{H}_{ji}^{(1)} & & 11 & 0 & 0 & 0 & 0 & 0 & 0 & 0 \\ & & & & 0 & 0 & 0 & 0 & 11 & 0 & 0 & 0 \\ & & & & 0 & 0 & 0 & 0 & 0 & 0 & 0 & 0 \\ 0 & 11 & 0 & 0 & & & & & 0 & 0 & 0 & 0 \\ 0 & 0 & 0 & 0 & & & \hat{H}_{ji}^{(1)} & & 0 & 0 & 0 & 0 \\ 0 & 0 & 0 & 0 & & & & & 0 & 11 & 0 & 0 \\ 0 & 0 & 0 & 0 & & & & & 0 & 0 & 0 & 0 \\ 0 & 0 & 11 & 0 & 0 & 0 & 0 & 0 & & & & \\ 0 & 0 & 0 & 0 & 0 & 0 & 11 & 0 & & \hat{H}_{ji}^{(1)} & & \\ 0 & 0 & 0 & 0 & 0 & 0 & 0 & 0 & & & & \\ 0 & 0 & 0 & 0 & 0 & 0 & 0 & 0 & & & & \end{bmatrix}. \tag{103}$$

Similarly for ${}^{e}K_{ji}^{(n)}$ we can write equation (37)

$$\begin{aligned} {}^{M_J}K_{ji}^{(n)} &= c^2 \int_e \big((b_j + 2d_j x + g_j y, c_j + 2f_j y + g_j x).(b_i + 2d_i x + g_i y, c_i + 2f_i y + g_i x)\big) d\underline{x} \\ &= c^2 \int_e \big(b_j b_i + 2(b_j d_i + b_i d_j)x + (b_j g_i + b_i g_j)y + 4d_j d_i x^2 + g_j g_i y^2 \\ &\quad +2(d_j g_i + d_i g_j)xy + c_j c_i + (c_j g_i + c_i g_j)x + 2(c_j f_i + c_i f_j)y + g_j g_i x^2 \\ &\quad +4f_j f_i y^2 + 2(f_j g_i + f_i g_j)xy\big) d\underline{x}. \end{aligned} \tag{104}$$

For each element (edge) e where $e \in M_K$ or $e \in M_I$

$$\begin{aligned} {}^{M_K}K_{ji}^{(n)} = {}^{M_I}K_{ji}^{(n)} &= c^2 \int_e (b_j + 2d_j x, c_j + 2d_j y).(b_i + 2d_i x, c_i + 2d_i y) d\underline{x}, \\ &= c^2 \int_e \Big(b_i b_j + 2(d_j b_i + d_i b_j)x + 4d_i d_j x^2 + c_i c_j + 2(d_i c_j + d_j c_i)y \\ &\quad + 4d_i d_j y^2 \Big) d\underline{x}. \end{aligned} \tag{105}$$

By using the definition of c that in equation (23) and using equation (80) then we can write equation (37) as

$$K_{ji}^{(n)} = \begin{cases} hc_T^2 \int_0^1 \nabla\phi_j . \nabla\phi_i \, ds & \text{if } e \in M_J \\ \frac{h}{\sqrt{3}} \big(c_T^2 \int_0^\nu \nabla\phi_j . \nabla\phi_i \, ds + c_P^2 \int_\nu^1 \nabla\phi_j . \nabla\phi_i \, ds \big) & \text{if } e \in M_K \\ hc_T^2 \int_0^1 \nabla\phi_j . \nabla\phi_i \, ds & \text{if } e \in M_I, \end{cases} \tag{106}$$

where ν is a parameter indicating the volume fraction of piezoelectric material in edge e. For $e \in M_J$,

$${}^{M_J}K_{ji}^{(n)} = hc_T^2 \begin{cases} \frac{52}{h^2} \int_0^1 s^2 \, ds & \text{if } j = i = p \\ \frac{-44}{h^2} \int_0^1 s(s-1) \, ds & \text{if } (j = p \text{ and } i = q) \text{ or } (j = q \text{ and } i = p) \\ \frac{52}{h^2} \int_0^1 (s-1)^2 \, ds & \text{if } j = i = q \\ 0 & \text{otherwise.} \end{cases} \tag{107}$$

That is

$${}^{M_J}K_{ji}^{(n)} = \frac{2}{3h} c_T^2 \begin{cases} 26 & \text{if } j = i = p \\ 11 & \text{if } (j = p \text{ and } i = q) \text{ or } (j = q \text{ and } i = p) \\ 26 & \text{if } j = i = q \\ 0 & \text{otherwise.} \end{cases} \tag{108}$$

For $e \in M_K$,

$$
{}^{M_K}K_{ji}^{(n)} = \frac{h}{\sqrt{3}} \begin{cases} \frac{12}{h^2}(c_T^2 \int_0^\nu s^2\,ds + c_P^2 \int_\nu^1 s^2\,ds) & \text{if } j = i = p \\ \frac{12}{h^2}(c_T^2 \int_0^\nu s(s-1)\,ds + c_P^2 \int_\nu^1 s(s-1)\,ds) & \text{if } (j = p \text{ and } i = q) \\ & \text{or } (j = q \text{ and } i = p) \\ \frac{12}{h^2}(c_T^2 \int_0^\nu (s-1)^2\,ds + c_P^2 \int_\nu^1 (s-1)^2\,ds) & \text{if } j = i = q \\ 0 & \text{otherwise.} \end{cases} \tag{109}
$$

That is

$$
{}^{M_K}K_{ji}^{(n)} = \frac{2}{3h}c_T^2 \begin{cases} 2\sqrt{3}\big(\nu^3 + \frac{c_P^2}{c_T^2}(1-\nu^3)\big) & \text{if } j = i = p \\ \sqrt{3}\big(\nu^2(2\nu-3) - \frac{c_P^2}{c_T^2}(\nu-1)^2(1+2\nu)\big) & \text{if } (j = p \text{ and } i = q) \\ & \text{or } (j = q \text{ and } i = p) \\ 2\sqrt{3}\big(\nu(\nu^2-3\nu+3) - \frac{c_P^2}{c_T^2}(\nu-1)^3\big) & \text{if } j = i = q \\ 0 & \text{otherwise.} \end{cases} \tag{110}
$$

For $e \in M_I$,

$$
{}^{M_I}K_{ji}^{(n)} = hc_T^2 \begin{cases} \frac{52}{h^2}\int_0^1 s^2\,ds & \text{if } j = i = q \\ 0 & \text{otherwise.} \end{cases} \tag{111}
$$

That is

$$
{}^{M_I}K_{ji}^{(n)} = \frac{2}{3h}c_T^2 \begin{cases} 26 & \text{if } j = i = q \\ 0 & \text{otherwise.} \end{cases} \tag{112}
$$

Assembling the full matrix in equation (37) gives, for generation level $n = 1$

$$
K_{ji}^{(1)} = \frac{2}{3h}c_T^2 \begin{bmatrix} D & 11 & 11 & R \\ 11 & D & 11 & R \\ 11 & 11 & D & R \\ R & R & R & E \end{bmatrix} = \frac{2}{3h}c_T^2 \hat{K}_{ji}^{(1)}, \tag{113}
$$

D=$78 + 2\sqrt{3}\big(\nu^3 + \frac{c_P^2}{c_T^2}(1-\nu^3)\big)$, R=$\sqrt{3}\big(\nu^2(2\nu-3) - \frac{c_P^2}{c_T^2}(\nu-1)^2(1+2\nu)\big)$ and E=$6\sqrt{3}\big(\nu(\nu^2-3\nu+3) - \frac{c_P^2}{c_T^2}(\nu-1)^3\big)$. For generation level $n=2$

$$K_{ji}^{(2)} = \frac{2}{3h}c_T^2 \begin{bmatrix} & & & & 0 & 0 & 0 & 0 & 0 & 0 & 0 & 0 \\ & & \hat{K}_{ji}^{(1)} & & 11 & 0 & 0 & 0 & 0 & 0 & 0 & 0 \\ & & & & 0 & 0 & 0 & 0 & 11 & 0 & 0 & 0 \\ & & & & 0 & 0 & 0 & 0 & 0 & 0 & 0 & 0 \\ 0 & 11 & 0 & 0 & & & & & 0 & 0 & 0 & 0 \\ 0 & 0 & 0 & 0 & & & \hat{K}_{ji}^{(1)} & & 0 & 0 & 0 & 0 \\ 0 & 0 & 0 & 0 & & & & & 0 & 11 & 0 & 0 \\ 0 & 0 & 0 & 0 & & & & & 0 & 0 & 0 & 0 \\ 0 & 0 & 11 & 0 & 0 & 0 & 0 & 0 & & & & \\ 0 & 0 & 0 & 0 & 0 & 0 & 11 & 0 & & \hat{K}_{ji}^{(1)} & & \\ 0 & 0 & 0 & 0 & 0 & 0 & 0 & 0 & & & & \\ 0 & 0 & 0 & 0 & 0 & 0 & 0 & 0 & & & & \end{bmatrix}. \tag{114}$$

Combining equations (102) and (113) gives equation (35) as

$$A_{ji}^{(1)} = h \begin{bmatrix} \alpha & \beta & \beta & \mathcal{P} \\ \beta & \alpha & \beta & \mathcal{P} \\ \beta & \beta & \alpha & \mathcal{P} \\ \mathcal{P} & \mathcal{P} & \mathcal{P} & \theta \end{bmatrix} = h\hat{A}_{ji}^{(1)}, \tag{115}$$

where $\alpha = (q^2/30)\big(48 + (16/\sqrt{3})\big) + (2/3)\big(78 + 2\sqrt{3}\big(\nu^3 + (c_P^2/c_T^2)(1-\nu^3)\big)\big)$, $\beta = (11/30)q^2 + 22/3$, $\mathcal{P} = (q^2/30)(11/\sqrt{3}) + (2/3)\big(\sqrt{3}\big(\nu^2(2\nu-3) - (c_P^2/c_T^2)(\nu-1)^2(1+2\nu)\big)\big)$, and $\theta = (q^2/30)(48/\sqrt{3}) + (2/3)\big(6\sqrt{3}\big(\nu(\nu^2-3\nu+3) - (c_P^2/c_T^2)(\nu-1)^3\big)\big)$.

Similarly, for generation level $n = 2$,

$$A_{ji}^{(2)} = h \begin{bmatrix} & & & & 0 & 0 & 0 & 0 & 0 & 0 & 0 & 0 \\ & & \hat{A}_{ji}^{(1)} & & \beta & 0 & 0 & 0 & 0 & 0 & 0 & 0 \\ & & & & 0 & 0 & 0 & 0 & \beta & 0 & 0 & 0 \\ & & & & 0 & 0 & 0 & 0 & 0 & 0 & 0 & 0 \\ 0 & \beta & 0 & 0 & & & & & 0 & 0 & 0 & 0 \\ 0 & 0 & 0 & 0 & & & \hat{A}_{ji}^{(1)} & & 0 & 0 & 0 & 0 \\ 0 & 0 & 0 & 0 & & & & & 0 & \beta & 0 & 0 \\ 0 & 0 & 0 & 0 & & & & & 0 & 0 & 0 & 0 \\ 0 & 0 & \beta & 0 & 0 & 0 & 0 & 0 & & & & \\ 0 & 0 & 0 & 0 & 0 & 0 & \beta & 0 & & \hat{A}_{ji}^{(1)} & & \\ 0 & 0 & 0 & 0 & 0 & 0 & 0 & 0 & & & & \\ 0 & 0 & 0 & 0 & 0 & 0 & 0 & 0 & & & & \end{bmatrix}. \tag{116}$$

A similar treatment, by using the definition of c that in equation (23), can be given to equation (34) to give $\big(m = (N+1)/2\big)$

$$b_j^{(n)} = \begin{cases} -(\int_{e_{M+1}} (q^2 \psi_{N+2} \phi_j + h^2 \nabla \psi_{N+2} . \nabla \phi_j) d\underline{x}) U_A, & j = 1 \\ -(\int_{e_{M+2}} (q^2 \psi_{N+3} \phi_j + h^2 \nabla \psi_{N+3} . \nabla \phi_j) d\underline{x}) U_B, & j = m = (N+1)/2 \\ -(\int_{e_{M+3}} (q^2 \psi_{N+4} \phi_j + h^2 \nabla \psi_{N+4} . \nabla \phi_j) d\underline{x}) U_C, & j = N \\ 0 & \text{otherwise.} \end{cases} \tag{117}$$

Using the isoparametric representation given by equation (80)

$$b_j^{(n)} = h\eta \begin{cases} U_A, & j = 1 \\ U_B, & j = m \\ U_C, & j = N \\ 0 & \text{otherwise} \end{cases} \tag{118}$$

where

$$\eta = \frac{2}{3} - \frac{11}{30}q^2. \tag{119}$$

For generation level $n = 1$,

$$b_j^{(1)} = h(\frac{2}{3} - \frac{11}{30}q^2) \begin{cases} U_A, & j = 1 \\ U_B, & j = 2 \\ U_C\ , & j = 3 \\ 0 & \text{otherwise} \end{cases}, \tag{120}$$

and for generation level $n = 2$,

$$b_j^{(2)} = h(\frac{2}{3} - \frac{11}{30}q^2) \begin{cases} U_A\ , & j = 1 \\ U_B\ , & j = 6 \\ U_C\ , & j = 11 \\ 0 & \text{otherwise} \end{cases}. \tag{121}$$

4 A Homogenised Model of the Transducer

In this section we introduce a homogenised model of this composite transducer [29, 33] that will be compared with the renormalisation approach being developed here; this comparison being made at a low number of fractal generation

levels (these are the most interesting cases as these are potentially manufacturable). The homogenised model described below can be thought of as the

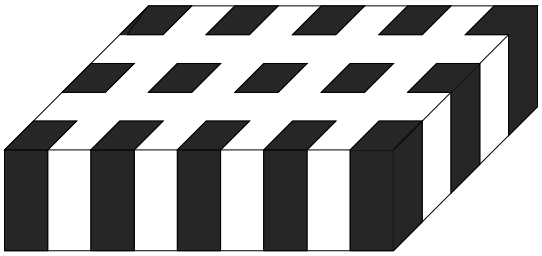

Figure 42: Illustration of a standard 1-3 composite transducer where the ceramic is black and the polymer is white. It clearly shows the regularity in the structure and the reliance on a single length scale.

operating characteristics that one would obtain from a conventional (i.e. non-fractal) 1-3 composite transducer as illustrated in Figure 42. The constitutive relations for the individual phases have a compact form, within the ceramic (E) phase, and within the polymer (P) phase [35, 34, 15]. From equation (1), and due to the properties of PZT-5H (see Appendix), we get

$$T_{11} = T_{12} = T_{21} = T_{22} = T_{33} = 0, \tag{122}$$

and

$$T_{13} = T_{31} = c_{1313}S_{13} + c_{1331}S_{31} - e_{113}E_1. \tag{123}$$

That is

$$T_5 = c_{55}(S_{13} + S_{31}) - e_{15}E_1, \tag{124}$$

and, using equation (3), since from equation (9) $u_{1,3} = 0$, then

$$T_5 = c_{44}u_{3,1} - e_{24}E_1, \tag{125}$$

since $c_{55} = c_{44}$ and $e_{15} = e_{24}$. Similarly we get

$$T_{23} = T_{32} = c_{3223}S_{23} + c_{3232}S_{32} - e_{232}E_2, \tag{126}$$

that is

$$T_4 = c_{44}u_{3,2} - e_{24}E_2. \tag{127}$$

So we rewrite equations (125) and (127), for the piezoelectric phase as

$$T_5^E = c_{44}^E u_{3,1}^E - e_{24}E_1^E \tag{128}$$

and

$$T_4^E = c_{44}^E u_{3,2}^E - e_{24}E_2^E. \tag{129}$$

Similarly, for polymer phase we get

$$T_5^P = c_{44}^P u_{3,1}^P, \tag{130}$$

and

$$T_4^P = c_{44}^P u_{3,2}^P, \tag{131}$$

since there is no piezoelectric effect in the polymer phase. From equation (2) we get for the piezoelectric phase

$$D_1^E = e_{24}u_{3,1}^E + \varepsilon_{11}^E E_1^E, \tag{132}$$

and

$$D_2^E = e_{24}^E u_{3,2}^E + \varepsilon_{11}^E E_2^E, \tag{133}$$

and for the polymer phase we get

$$D_1^P = \varepsilon_{11}^P E_1^P, \tag{134}$$

and

$$D_2^P = \varepsilon_{11}^P E_2^P, \tag{135}$$

where D_3^E, D_3^P are zero. We assume that any movement (strain) in the polymer phase is compensated by a strain in the piezoelectric phase, and so we can write

$$\bar{u}_{3,1} = vu_{3,1}^E + \bar{v}u_{3,1}^P, \tag{136}$$

and

$$\bar{u}_{3,2} = v u^E_{3,2} + \bar{v} u^P_{3,2}, \tag{137}$$

where v is the volume fraction of the piezoelectric phase where this is calculated via

$$v^{(n)} = \frac{\frac{3}{2}(3^n - 1)\left(\frac{L}{2^n - 1}\right) + 3^n\left(\frac{L}{(2^n-1)\sqrt{3}}\right)\nu}{\frac{3}{2}(3^n - 1)\left(\frac{L}{2^n - 1}\right) + 3^n\left(\frac{L}{(2^n-1)\sqrt{3}}\right)} \tag{138}$$

where $3(3^n - 1)/2$ is the number of elements that are piezoelectric (M_J), 3^n is the number of elements that are a polymer-piezoelectric composite (M_K), $L/(2^n - 1)$ is the length of elements M_J and $L/\left((2^n - 1)\sqrt{3}\right)$ is the length of elements M_K. That is

$$v^{(n)} = \frac{\frac{3}{2}(3^n - 1) + 3^{n-\frac{1}{2}}\nu}{\frac{3}{2}(3^n - 1) + 3^{n-\frac{1}{2}}} \tag{139}$$

and $\bar{v}^{(n)} = 1 - v^{(n)}$ is the volume fraction of polymer, where ν is the volume fraction of ceramic in the edges adjacent to the degree three vertices as detailed in section 3 and in equation (106) (see Figure 3, 4). For example at generation level $(n = 1)$ if $\nu = 1$ then $v = 1$ and if $\nu = 0$ then $v = 3/(3 + \sqrt{3})$. Assuming the electric fields are similarly averaged then

$$\bar{E}_1 = v E^E_1 + \bar{v} E^P_1, \tag{140}$$

and

$$\bar{E}_2 = v E^E_2 + \bar{v} E^P_2. \tag{141}$$

Assuming that the stresses in each phase are equal then

$$\bar{T}_4 = T^E_4 = T^P_4 \tag{142}$$

and

$$\bar{T}_5 = T^E_5 = T^P_5. \tag{143}$$

If the electrical displacements are also equal in each phase then

$$\bar{D}_1 = D_1^E = D_1^P \tag{144}$$

and

$$\bar{D}_2 = D_2^E = D_2^P. \tag{145}$$

From the symmetry of the $SG(3,4)$ lattice (see Figure 44) then we have

$$\bar{u}_{3,2} = \bar{u}_{3,1} = \bar{u}, \tag{146}$$

since $u_{3,2}^E = u_{3,1}^E = u^E$, and $u_{3,2}^P = u_{3,1}^P = u^P$. We take the electric fields to be the same in both phases, namely,

$$\bar{E}_1 = \bar{E}_2 = \bar{E}, \tag{147}$$

since $E_1^E = E_2^E = E^E$, and $E_1^P = E_2^P = E^P$. Also

$$\bar{T}_4 = \bar{T}_5 = \bar{T}, \tag{148}$$

and

$$\bar{D}_1 = \bar{D}_2 = \bar{D}. \tag{149}$$

From equations (142), (148), (146) and (147) we can write equation (129) as

$$\bar{T} = c_{44}^E u^E - e_{24} E^E, \tag{150}$$

and from equations (144), (149), (146) and (147) we can write equation (132) as

$$\bar{D} = e_{24} u^E + \varepsilon_{11}^E E^E. \tag{151}$$

For the polymer phase, we have from equations (142), (148) and (146) that we can write equation (131) as

$$\bar{T} = c_{44}^P u^P, \tag{152}$$

and from equations (144), (149) and (147) we can write equation (134) as

$$\bar{D} = \varepsilon_{11}^{P} E^{P}. \tag{153}$$

From equation (146) we can write equations (137) and (136) as

$$\bar{u} = \bar{S} = v u^{E} + \bar{v} u^{P}, \tag{154}$$

and from equation (147) we can write equations (140) and (141) as

$$\bar{E} = v E^{E} + \bar{v} E^{P}. \tag{155}$$

From equation (152) we get

$$u^{P} = \frac{\bar{T}}{c_{44}^{P}}, \tag{156}$$

and from equation (153) we get

$$E^{P} = \frac{\bar{D}}{\varepsilon_{11}^{P}}. \tag{157}$$

Hence, from equations (154) and (156) we get

$$u^{E} = \frac{1}{v}(\bar{S} - \bar{v}\frac{\bar{T}}{c_{44}^{P}}), \tag{158}$$

and from equations (155) and (157) we get

$$E^{E} = \frac{1}{v}(\bar{E} - \bar{v}\frac{\bar{D}}{\varepsilon_{11}^{P}}). \tag{159}$$

Substituting equations (158) and (159) into equation (150) gives

$$\bar{T} = c_{44}^{E}\frac{1}{v}(\bar{S} - \bar{v}\frac{\bar{T}}{c_{44}^{P}}) - e_{24}\frac{1}{v}(\bar{E} - \bar{v}\frac{\bar{D}}{\varepsilon_{11}^{P}}). \tag{160}$$

That is

$$\bar{T}\big(1 + \frac{\bar{v}c_{44}^{E}}{v c_{44}^{P}}\big) = \frac{c_{44}^{E}}{v}\bar{S} - \frac{e_{24}}{v}\bar{E} + \frac{\bar{v}e_{24}}{v\varepsilon_{11}^{P}}\bar{D}. \tag{161}$$

Also, substituting equations (158) and (159) into equation (151) gives

$$\bar{D} = \frac{e_{24}}{v}\big(\bar{S} - \bar{v}\frac{\bar{T}}{c_{44}^P}\big) + \frac{\varepsilon_{11}^E}{v}\big(\bar{E} - \bar{v}\frac{\bar{D}}{\varepsilon_{11}^P}\big). \tag{162}$$

That is

$$\bar{D}\big(1 + \frac{\bar{v}\varepsilon_{11}^E}{v\varepsilon_{11}^P}\big) = \frac{e_{24}}{v}\bar{S} - \frac{\bar{v}e_{24}}{vc_{44}^P}\bar{T} + \frac{\varepsilon_{11}^E}{v}\bar{E}. \tag{163}$$

Hence,

$$\bar{D} = \frac{\varepsilon_{11}^P e_{24}}{v\varepsilon_{11}^P + \bar{v}\varepsilon_{11}^E}\bar{S} - \frac{\bar{v}e_{24}\varepsilon_{11}^P}{c_{44}^P(v\varepsilon_{11}^P + \bar{v}\varepsilon_{11}^E)}\bar{T} + \frac{\varepsilon_{11}^P\varepsilon_{11}^E}{v\varepsilon_{11}^P + \bar{v}\varepsilon_{11}^E}\bar{E}. \tag{164}$$

That is

$$\bar{D} = \frac{\varepsilon_{11}^P e_{24}}{\bar{\varepsilon}^*}\bar{S} - \frac{\bar{v}e_{24}\varepsilon_{11}^P}{c_{44}^P\bar{\varepsilon}^*}\bar{T} + \frac{\varepsilon_{11}^P\varepsilon_{11}^E}{\bar{\varepsilon}^*}\bar{E}, \tag{165}$$

where $\bar{\varepsilon}^* = v\varepsilon_{11}^P + \bar{v}\varepsilon_{11}^E$. Putting this into equation (161) gives

$$\bar{T}\big(1 + \frac{\bar{v}c_{44}^E}{vc_{44}^P}\big) = \frac{c_{44}^E}{v}\bar{S} - \frac{e_{24}}{v}\bar{E} + \frac{\bar{v}e_{24}^2}{v\bar{\varepsilon}^*}\bar{S} - \frac{\bar{v}^2e_{24}^2}{vc_{44}^P\bar{\varepsilon}^*}\bar{T} + \frac{\bar{v}e_{24}\varepsilon_{11}^E}{v\bar{\varepsilon}^*}\bar{E} \tag{166}$$

that is

$$\bar{T}\big(1 + \frac{\bar{v}c_{44}^E}{vc_{44}^P} + \frac{\bar{v}^2e_{24}^2}{vc_{44}^P\bar{\varepsilon}^*}\big) = \big(\frac{c_{44}^E}{v} + \frac{\bar{v}e_{24}^2}{v\bar{\varepsilon}^*}\big)\bar{S} + \big(\frac{\bar{v}e_{24}\varepsilon_{11}^E}{v\bar{\varepsilon}^*} - \frac{e_{24}}{v}\big)\bar{E}, \tag{167}$$

and so

$$\bar{T}\big(vc_{44}^P\bar{\varepsilon}^* + \bar{v}c_{44}^E\bar{\varepsilon}^* + \bar{v}^2e_{24}^2\big) = \big(c_{44}^Ec_{44}^P\bar{\varepsilon}^* + \bar{v}c_{44}^Pe_{24}^2\big)\bar{S} + \big(\bar{v}c_{44}^Pe_{24}\varepsilon_{11}^E - c_{44}^Pe_{24}\bar{\varepsilon}^*\big)\bar{E}. \tag{168}$$

That is

$$\bar{T} = \bar{c}_{44}\bar{S} - \bar{e}_{24}\bar{E}, \tag{169}$$

since $\bar{c}_{44} = \big(c_{44}^Ec_{44}^P\bar{\varepsilon}^* + \bar{v}c_{44}^Pe_{24}^2\big)/\big(vc_{44}^P\bar{\varepsilon}^* + \bar{v}c_{44}^E\bar{\varepsilon}^* + \bar{v}^2e_{24}^2\big)$ and $\bar{e}_{24} = \big(c_{44}^Pe_{24}v\varepsilon_{11}^P\big)/\big(vc_{44}^P\bar{\varepsilon}^* + \bar{v}c_{44}^E\bar{\varepsilon}^* + \bar{v}^2e_{24}^2\big)$. Substituting this into equation (165) gives

$$\bar{D} = \frac{\varepsilon_{11}^P e_{24}}{\bar{\varepsilon}^*}\bar{S} + \frac{\varepsilon_{11}^P\varepsilon_{11}^E}{\bar{\varepsilon}^*}\bar{E} - \frac{\bar{v}e_{24}\varepsilon_{11}^P}{c_{44}^P\bar{\varepsilon}^*}(\bar{c}_{44}\bar{S} - \bar{e}_{24}\bar{E}), \tag{170}$$

that is

$$\bar{D} = \Big(\frac{\varepsilon_{11}^P e_{24}}{\bar{\varepsilon}^*} - \frac{\bar{v} e_{24} \varepsilon_{11}^P \bar{c}_{44}}{c_{44}^P \bar{\varepsilon}^*}\Big)\bar{S} + \Big(\frac{\varepsilon_{11}^P \varepsilon_{11}^E}{\bar{\varepsilon}^*} + \frac{\bar{v} e_{24} \varepsilon_{11}^P \bar{e}_{24}}{c_{44}^P \bar{\varepsilon}^*}\Big)\bar{E}. \tag{171}$$

Now

$$\begin{aligned} \frac{\varepsilon_{11}^P e_{24}}{\bar{\varepsilon}^*} - \frac{\bar{v} e_{24} \varepsilon_{11}^P \bar{c}_{44}}{c_{44}^P \bar{\varepsilon}^*} &= \frac{\varepsilon_{11}^P e_{24}}{\bar{\varepsilon}^*} - \frac{\bar{v} e_{24} \varepsilon_{11}^P \big(c_{44}^E c_{44}^P \bar{\varepsilon}^* + \bar{v} c_{44}^P e_{24}^2\big)}{c_{44}^P \bar{\varepsilon}^* \big(v c_{44}^P \bar{\varepsilon}^* + \bar{v} c_{44}^E \bar{\varepsilon}^* + \bar{v}^2 e_{24}^2\big)} \\ &= \frac{c_{44}^P e_{24} v \varepsilon_{11}^P}{v c_{44}^P \bar{\varepsilon}^* + \bar{v} c_{44}^E \bar{\varepsilon}^* + \bar{v}^2 e_{24}^2} = \bar{e}_{24}. \end{aligned} \tag{172}$$

So

$$\bar{D} = \bar{e}_{24}\bar{S} + \bar{\varepsilon}_{11}\bar{E}, \tag{173}$$

where $\bar{\varepsilon}_{11} = (\varepsilon_{11}^P \varepsilon_{11}^E)/\bar{\varepsilon}^* + (\bar{v} e_{24} \varepsilon_{11}^P \bar{e}_{24})/(c_{44}^P \bar{\varepsilon}^*)$. We then have

$$\bar{E} = \frac{\bar{D}}{\bar{\varepsilon}_{11}} - \frac{\bar{e}_{24}}{\bar{\varepsilon}_{11}}\bar{S}, \tag{174}$$

and so we can rewrite equation (169) as

$$\bar{T} = \bar{c}_{44}\bar{S} - \bar{e}_{24}\big(\frac{\bar{D}}{\bar{\varepsilon}_{11}} - \frac{\bar{e}_{24}}{\bar{\varepsilon}_{11}}\bar{S}\big). \tag{175}$$

That is

$$\bar{T} = \bar{c}_{44}^T \bar{S} - \bar{\zeta}\bar{D}, \tag{176}$$

where $\bar{c}_{44}^T = \bar{c}_{44} + \bar{e}_{24}^2/\bar{\varepsilon}_{11}$ and $\bar{\zeta} = \bar{e}_{24}/\bar{\varepsilon}_{11}$. The specific acoustic impedance of the composite is then [33],

$$\bar{Z}_T = \sqrt{\bar{c}_{44}^T \bar{\rho}_T} \tag{177}$$

where $\bar{\rho}_T = v\rho^E + \bar{v}\rho^P$ is the average density, and the longitudinal velocity is [33],

$$\bar{c}_T = \sqrt{\frac{\bar{c}_{44}^T}{\bar{\rho}_T}}. \tag{178}$$

In order to calculate the transmission sensitivity, consider the circuit shown in Figure 43. The current across the transducer $\bar{I}$ is given by [29]

$$\bar{I} = \frac{a\bar{V}}{Z_E + b} \tag{179}$$

where $a = Z_P/(Z_0 + Z_P)$, $b = Z_0 Z_P/(Z_0 + Z_P)$, Z_0 is series electrical load and Z_P is the parallel electrical load. The non-dimensionalised form for the electrical impedance of the transducer is then [29]

$$\bar{Z}_E = \frac{1}{q\bar{C}_0 Z_0}\Big(1 - \frac{\bar{\zeta}^2\bar{C}_0}{2q\bar{Z}_T}(\bar{K}_F\bar{T}_F + \bar{K}_B\bar{T}_B)\Big), \tag{180}$$

where $\bar{T}_F = 2\bar{Z}_T/(\bar{Z}_T + Z_L)$ and $\bar{T}_B = 2\bar{Z}_T/(\bar{Z}_T + Z_B)$ are non-dimensional transmission coefficients, $\bar{K}_F$ and $\bar{K}_B$ are also non-dimensional and are given by

$$\bar{K}_F = \frac{(1 - e^{-q\bar{\tau}})(1 - \bar{R}_B e^{-q\bar{\tau}})}{(1 - \bar{R}_F\bar{R}_B e^{-2q\bar{\tau}})} \tag{181}$$

and

$$\bar{K}_B = \frac{(1 - e^{-q\bar{\tau}})(1 - \bar{R}_F e^{-q\bar{\tau}})}{(1 - \bar{R}_F\bar{R}_B e^{-2q\bar{\tau}})} \tag{182}$$

where $\bar{R}_F = (\bar{Z}_T - Z_L)/(\bar{Z}_T + Z_L)$ and $\bar{R}_B = (\bar{Z}_T - Z_B)/(\bar{Z}_T + Z_B)$ are non-dimensionalised reflection coefficients and $\bar{\tau} = L/\bar{c}_T$ is the wave transit time across the device. Note that the capacitance of the device is given by $\bar{C}_0 = A_r\bar{\varepsilon}_{11}/L$. The non-dimensionalised transmission sensitivity $\bar{\psi}$ is [14]

$$\bar{\psi}(f) = \Big(\frac{\bar{F}}{V}\Big)/\bar{\zeta}\bar{C}_0 = -\frac{a\bar{A}_F\bar{\lambda}\bar{K}_F}{2\bar{C}_0}\Big(1 - \frac{\bar{\zeta}^2\bar{\lambda}(\bar{K}_F T_F + \bar{K}_B T_B)}{2q\bar{Z}_T}\Big)^{-1}, \tag{183}$$

where $\bar{\lambda} = \bar{C}_0/(1 + q\bar{C}_0 b)$ and $\bar{A}_F = 2Z_L/(Z_L + \bar{Z}_T)$ are dimensionless constants. The non-dimensionalised reception sensitivity $\bar{\phi}$ is [13]

$$\bar{\phi} = \Big(\frac{\bar{V}}{F}\Big)(\bar{e}_{24}L) = \Big(\frac{-\bar{\zeta}T_F\bar{K}_F\bar{H}\bar{e}_{24}L}{q\bar{Z}_T}\Big)\Big(1 - \frac{\bar{\zeta}^2\bar{H}(\bar{K}_F T_F + \bar{K}_B T_B)}{2q^2\bar{Z}_T Z_E}\Big)^{-1}, \tag{184}$$

where $\bar{H} = q\bar{C}_0 b/(1 + q\bar{C}_0 b)$. Having derived expressions for the main operating characteristics of a homogenised device these will be used to compare with the characteristics of the fractal device using the renormalisation approach. This will allow us to assess any practical benefits arising from this novel design.

5 Renormalisation Model of the Transducer Operating Characteristics

Mechanical and electrical loads will be introduced to the transducer at its boundaries as displayed in Figure 43. In the mechanical load at the front face of the transducer the governing equation is

$$\rho_L \frac{\partial^2 u_L}{\partial t^2} = Y_L \frac{\partial^2 u_L}{\partial x_L^2}, \tag{185}$$

where u_L is the displacement of the load material, ρ_L is the density and Y_L is the shear modulus. That is

$$\frac{\partial^2 u_L}{\partial t^2} = \frac{Y_L}{\rho_L} \frac{\partial^2 u_L}{\partial x_L^2} \tag{186}$$

and so, nondimensionalising in a similar fashion to equation (24), gives

$$\frac{\partial^2 u_L}{\partial \theta^2} = \Big(\frac{hc_L}{c_T}\Big)^2 \frac{\partial^2 u_L}{\partial x_L^2} \tag{187}$$

where c_L is the wave speed in the load ($c_L^2 = Y_L/\rho_L$). Taking Laplace transforms as was done in equation (25) gives

$$\frac{\partial^2 \bar{u}_L}{\partial x_L^2} - \Big(\frac{qc_T}{hc_L}\Big)^2 \bar{u}_L = 0. \tag{188}$$

Hence, the displacement in the load is

$$\bar{u}_L = A_L e^{(-qc_T x_L/hc_L)} + B_L e^{(qc_T x_L/hc_L)}, \tag{189}$$

where A_L and B_L are constants. Similarly the displacement in the backing layer (subscript B) is given by

$$\bar{u}_B = A_B e^{(-qc_T x_B/hc_B)} + B_B e^{(qc_T x_B/hc_B)}, \tag{190}$$

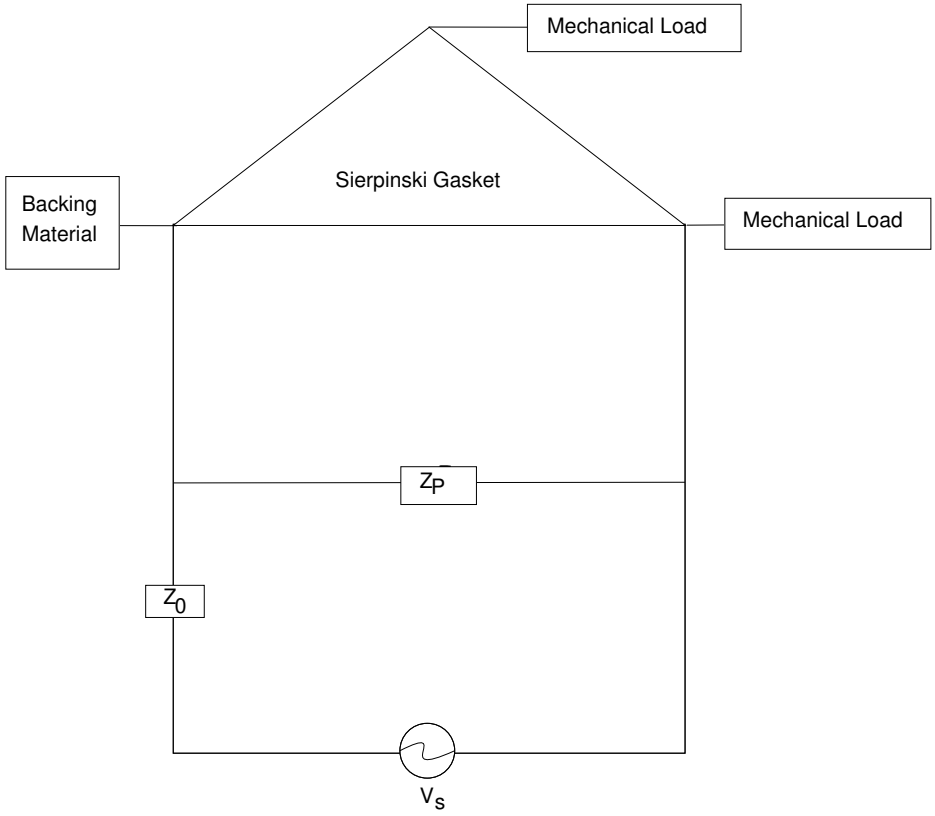

Figure 43: Physical layout of the fractal transducer.

where A_B and B_B are constants and c_B is the wave speed in the backing material. As the backing layer is highly attenuative it is assumed that there is only a wave travelling away from the piezoelectric layer ($SG(3,4)$) interface ($x_B = 0$) in the direction of increasing x_B, and so we set $B_B = 0$. Continuity of displacement at the transducer-mechanical load interface and the symmetry of the $SG(3,4)$ lattice give

$$U_A = \bar{u}_B(0) = A_B, \tag{191}$$

$$U_B = \bar{u}_L(0) = A_L + B_L, \tag{192}$$

$$U_C = \bar{u}_L(0) = A_L + B_L, \tag{193}$$

where U_A, U_B and U_C are the mechanical displacements at the fictitious vertices A, B and C, respectively. The force F on each vertex is given by $F = A_r\bar{T}$, where $A_r = \xi L/(2^n - 1)$ is the cross-sectional area of each edge of the fractal lattice. Hence, from equation (176),

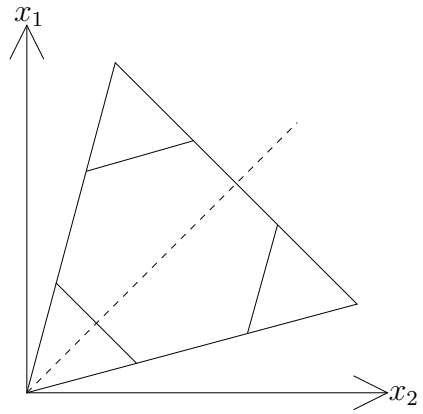

Figure 44: The line of symmetry given by $x_1 = x_2$

$$F = A_r\bar{c}_{44}^T\bar{S} - \bar{\zeta}\bar{D}A_r. \tag{194}$$

By applying an electrical charge $\bar{Q}$ at one of the transducer-electrical load interfaces then Gauss' law gives $\bar{D} = \bar{Q}/A_r$. Since $\bar{S} = \partial\bar{u}/\partial x$, then

$$F = A_r\bar{c}_{44}^T\frac{\partial\bar{u}}{\partial x} - \bar{\zeta}\bar{Q}. \tag{195}$$

So from the continuity of force we get $F_T(\bar{u}_m) = F_L(\bar{u}_{\partial\Omega}) = F_L(x_L = 0)$. That is, from equation (189),

$$A_r\bar{c}_{44}^T\frac{(U_B - U_m)}{h} - \bar{\zeta}\bar{Q} = A_rY_L\Big(\frac{qc_T}{hc_L}\Big)(-A_L + B_L), \tag{196}$$

and so

$$U_B - U_m - \frac{\bar{\zeta}\bar{Q}}{\bar{c}_{44}^T}\Big(\frac{h}{A_r}\Big) = \frac{Z_L}{\bar{\bar{Z}}_T}q(-A_L + B_L), \tag{197}$$

where the mechanical impedance of the load is $Z_L = A_r Y_L/c_L$, of the backing material is $Z_B = \rho_B c_B A_r$, and of the transducer is $\bar{\bar{Z}}_T = A_r \bar{c}_{44}^T/c_T$, where ρ_L (ρ_B) is the density and c_L (c_B) is the wave velocity in the load (backing material). At each generation level of the Sierpinski gasket transducer the ratio of the cross-sectional area of each edge to its length is denoted by $\xi = A_r/h$. The overall extent of the lattice (L) is fixed and so the length of the edges will steadily decrease and, by fixing ξ, the cross-sectional area will also decrease as the fractal generation level increases. Hence, equation (197), and its equivalent at the front face of the transducer, can be written

$$U_1 - U_A - \frac{\bar{\zeta}\bar{Q}}{\bar{c}_{44}^T \xi} = \frac{Z_B}{\bar{\bar{Z}}_T} q(-A_B), \tag{198}$$

$$U_B - U_m - \frac{\bar{\zeta}\bar{Q}}{\bar{c}_{44}^T \xi} = \frac{Z_L}{\bar{\bar{Z}}_T} q(-A_L + B_L). \tag{199}$$

From equations (191) and (198) we have that $U_A = \gamma_1 U_1 + \delta_1$ and from equations (192),(193) and (199) we have

$$U_B = \gamma_m U_m + \delta_m = U_C = \gamma_N U_N + \delta_N, \tag{200}$$

where

$$\gamma_j = \begin{cases} (1 - q\frac{Z_B}{\bar{\bar{Z}}_T})^{-1}, & j = 1 \\ (1 - q\frac{Z_L}{\bar{\bar{Z}}_T})^{-1}, & j = m \text{ or } N \end{cases} \tag{201}$$

and

$$\delta_j = \begin{cases} -\frac{\bar{\zeta}\bar{Q}}{\bar{c}_{44}^T \xi}\left(1 - q\frac{Z_B}{\bar{\bar{Z}}_T}\right)^{-1}, & j = 1 \\ \left(1 - q\frac{Z_L}{\bar{\bar{Z}}_T}\right)^{-1}\left(\frac{\bar{\zeta}\bar{Q}}{\bar{c}_{44}^T \xi} - 2A_L q\frac{Z_L}{\bar{\bar{Z}}_T}\right), & j = m \text{ or } N. \end{cases} \tag{202}$$

Hence, equation (118) becomes

$$b_j^{(n)} = h\bar{\gamma}_j U_j + h\bar{\delta}_j \quad j = 1, m \text{ or } N \tag{203}$$

where $\bar{\gamma}_j = \eta\gamma_j$ and $\bar{\delta}_j = \eta\delta_j$. Putting equation (203) into equation (32) gives

$$\hat{A}_{ji}^{(n)} U_i = \bar{\gamma}_j U_j + \bar{\delta}_j \tag{204}$$

where $\hat{A} = A/h$ as in equation (115). Hence,

$$(\hat{A}_{ji}^{(n)} - \hat{B}_{ji}^{(n)}) U_i = \bar{\delta}_j, \quad i = 1, m \text{ or } N \tag{205}$$

where

$$\hat{B}_{ji}^{(n)} = \begin{bmatrix} \bar{\gamma}_1 & 0 & \cdots & & & & \cdots & 0 \\ 0 & 0 & \ddots & & & & & \vdots \\ \vdots & \ddots & \ddots & & & & & \\ & & & 0 & & 0 & & \\ & & & & \bar{\gamma}_m & & & \\ & & & 0 & & 0 & & \\ & & & & & & \ddots & \ddots & \vdots \\ \vdots & & & & & & \ddots & 0 & 0 \\ 0 & \cdots & & & & & \cdots & 0 & \bar{\gamma}_N \end{bmatrix}. \tag{206}$$

That is

$$F_{ji}^{(n)} U_i = \bar{\delta}_j, \tag{207}$$

and so

$$U_i = G_{ji}^{(n)} \bar{\delta}_j, \tag{208}$$

where

$$G_{ji}^{(n)} = \left(F_{ji}^{(n)}\right)^{-1} = \left(\hat{A}_{ji}^{(n)} - \hat{B}_{ji}^{(n)}\right)^{-1} \tag{209}$$

represents the Green's transfer matrix.

6 Renormalisation

From equation (208) the desired weightings at each vertex in Ω is given by

$$U_j^{(n)} = G_{j1}^{(n)}\bar{\delta}_1 + G_{jm}^{(n)}\bar{\delta}_m + G_{jN}^{(n)}\bar{\delta}_N. \tag{210}$$

In particular we will be interested in $U_1^{(n)}, U_m^{(n)}$ and $U_N^{(n)}$ and so we only need to be able to calculate the pivotal Green's functions $G_{ij}^{(n)}, \quad i,j \in \{1,m,N\}$. If

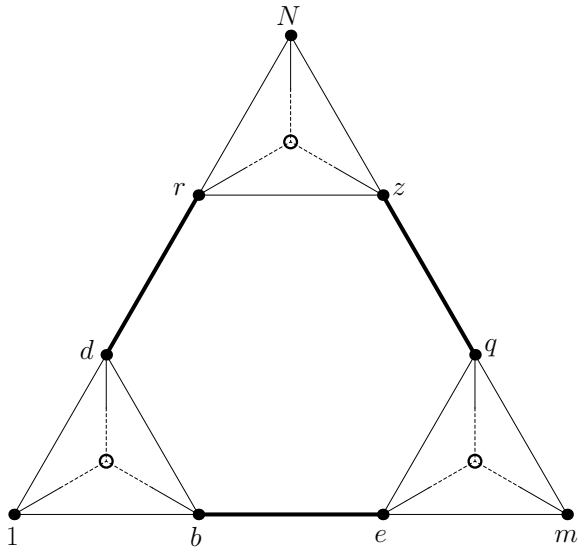

Figure 45: Three Sierpinski Gasket lattices of generation level $n-1$ are connected by the edges in bold $\big((b,e),(d,r)$ and $(q,z)\big)$ to create the Sierpinski Gasket lattice at generation level n.

we temporarily ignore matrix $\hat{B}$ in equation (209) (this matrix originates from consideration of the boundary conditions) then, due to the symmetries of the $SG(3,4)$ lattice (and hence in matrix $A^{(n)}$), we have

$$\hat{G}_{ii}^{(n)} = \hat{G}_{jj}^{(n)} = \hat{x}, \text{ say, where } i,j \in \{1,m,N\} \tag{211}$$

(i.e corner-to-same-corner), and

$$\hat{G}_{jk}^{(n)} = \hat{G}_{hk}^{(n)} = \hat{y}, \text{ say, where } j,k,h \in \{1,m,N\},\ j \neq k \neq h \tag{212}$$

(i.e corner-to-other-corner), where

$$\hat{G}^{(n)} = (\hat{A}^{(n)})^{-1}. \tag{213}$$

For clarity, at level $n+1$, we denote, $\hat{X} = \hat{G}_{ii}^{(n+1)}$ and $\hat{Y} = \hat{G}_{ij}^{(n+1)}$ where $i, j, \in \{1, m, N\}$, $i \neq j$. The matrix is symmetrical and consequently, $\hat{G}_{ij}^{(n)} = \hat{G}_{ji}^{(n)}$. From equation (24), since

$$\theta^{(n)} = \frac{c_T}{h^{(n)}} t, \tag{214}$$

then $\mathscr{L} : \theta^{(n)} \rightarrow q^{(n)}$ where $q^{(n)} = i\hat{\omega}^{(n)} = i2\pi\hat{f}^{(n)} = i2\pi(c_T/h^{(n)})^{-1} f^{(n)}$, $\hat{f}^{(n)}$ is the nondimensionalised natural frequency, $\hat{\omega}^{(n)}$ is the nondimensionalised angular frequency and $f^{(n)}$ (and $\omega^{(n)}$) are the dimensionalised equivalents. In order to use the renormalisation approach detailed below then we set $q = q^{(n)} = q^{(n+1)}$. This simply means that the output from the renormalisation methodology (and hence the electrical impedance and transmission/reception sensitivities) at a given q (fixed) is then that quantity at frequency $f^{(n)}$ at generation level n. So when comparing outputs at different generation levels one must ensure that the frequency is scaled appropriately (by $(c_T/h^{(n)})^{-1}$) when re-dimensionalising. An iterative procedure can be developed from equation (35) which can be written as

$$\hat{A}_{ji}^{(n)} = \tfrac{8}{5} q^2 I_n - T^{(n)} \tag{215}$$

where

$$T^{(n)} = \beta R^{(n)} - 4I_n, \tag{216}$$

$$R^{(n)} = \bar{R}^{(n-1)} + V^{(n-1)}, \tag{217}$$

$\bar{R}^{(n-1)}$ is a block-diagonal matrix whose three blocks are equal to $R^{(n-1)}$ with

$$R^{(1)} = \begin{bmatrix} 0 & -1 & -1 \\ -1 & 0 & -1 \\ -1 & -1 & 0 \end{bmatrix}, \tag{218}$$

and (see Figure 45)

$$V^{(n)} = \begin{cases} -1 & \text{if } (h,k) \in \{(b,e),(d,r),(q,z),(e,b),(r,d),(z,q)\} \\ 0 & \text{otherwise} \end{cases}. \tag{219}$$

So, using equations (215) and (216), we can write equation (213) as

$$\begin{aligned} \hat{G}^{(n)} &= \left(\tfrac{8}{5}q^2 I_n - T^{(n)}\right)^{-1} \\ &= \left((\tfrac{8}{5}q^2+4)I_n - \beta R^{(n)}\right)^{-1}. \end{aligned} \tag{220}$$

Hence,

$$(\hat{G}^{(n+1)})^{-1} = (\tfrac{8}{5}q^2+4)I_{n+1} - \beta R^{(n+1)}. \tag{221}$$

Since $\bar{G}^{(n)}$ is a block-diagonal matrix then

$$\begin{aligned} (\bar{G}^{(n)})^{-1} &= \overline{\hat{A}^{(n)}} \\ &= \overline{\left(\tfrac{8}{5}q^2 I_n - T^{(n)}\right)} \\ &= \tfrac{8}{5}q^2 I_{n+1} - \bar{T}^{(n)} \\ &= \tfrac{8}{5}q^2 I_{n+1} - (\beta\bar{R}^{(n)} - 4\bar{I}_n) \\ &= (\tfrac{8}{5}q^2+4)I_{n+1} - \beta\bar{R}^{(n)}. \end{aligned} \tag{222}$$

Now

$$\begin{aligned} I_{n+1} &= \bar{G}^{(n)}(\bar{G}^{(n)})^{-1} \\ &= \bar{G}^{(n)}\left((\tfrac{8}{5}q^2+4)I_{n+1} - \beta\bar{R}^{(n)}\right) \\ &= \bar{G}^{(n)}\left((\tfrac{8}{5}q^2+4)I_{n+1} - \beta(\bar{R}^{(n)} + V^{(n)}) + \beta V^{(n)}\right). \end{aligned}$$

From equations (217) and (221) then

$$\begin{aligned} I_{n+1} &= \bar{G}^{(n)}\big((\hat{G}^{(n+1)})^{-1} + \beta V^{(n)}\big) \\ &= \bar{G}^{(n)}\big((\hat{G}^{(n+1)})^{-1} + \beta V^{(n)}\hat{G}^{(n+1)}(\hat{G}^{(n+1)})^{-1}\big) \\ &= (\bar{G}^{(n)} + \bar{G}^{(n)}\beta V^{(n)}\hat{G}^{(n+1)})(\hat{G}^{(n+1)})^{-1}. \end{aligned} \tag{223}$$

Hence

$$\hat{G}^{(n+1)} = \bar{G}^{(n)} + \beta\bar{G}^{(n)}V^{(n)}\hat{G}^{(n+1)}. \tag{224}$$

To calculate $G_{ij}^{(n)}$ the boundary conditions must be reintroduced. From equations (209),(215) and (216)

$$\begin{aligned} (G^{(n)})^{-1} &= \hat{A}^{(n)} - \hat{B}^{(n)} \\ &= (\tfrac{8}{5}q^2 I_n - T^{(n)}) - \hat{B}^{(n)} \\ &= \tfrac{8}{5}q^2 I_n - (\beta R^{(n)} - 4I_n) - \hat{B}^{(n)} \\ &= (\tfrac{8}{5}q^2 + 4)I_n - \beta R^{(n)} - \hat{B}^{(n)}. \end{aligned} \tag{225}$$

Now, from equation (220)

$$\begin{aligned} I_n &= \hat{G}^{(n)}(\hat{G}^{(n)})^{-1} \\ &= \hat{G}^{(n)}\big((\tfrac{8}{5}q^2 + 4)I_n - \beta R^{(n)} - \hat{B}^{(n)} + \hat{B}^{(n)}\big). \end{aligned}$$

From equation (225) then,

$$\begin{aligned} I_n &= \hat{G}^{(n)}\big((G^{(n)})^{-1} + \hat{B}^{(n)}\big) \\ &= \hat{G}^{(n)}\big((G^{(n)})^{-1} + \hat{B}^{(n)}G^{(n)}(G^{(n)})^{-1}\big) \\ &= (\hat{G}^{(n)} + \hat{G}^{(n)}\hat{B}^{(n)}G^{(n)})(G^{(n)})^{-1}. \end{aligned} \tag{226}$$

Hence

$$G^{(n)} = \hat{G}^{(n)} + \hat{G}^{(n)}\hat{B}^{(n)}G^{(n)}. \tag{227}$$

6.1 Derivation of the pivotal recursion relationships

The $(i,j)^{th}$ element of the matrix equation (224) can be written as,

$$\hat{G}_{ij}^{(n+1)} = \bar{G}_{ij}^{(n)} + \sum_{h,k} \beta \bar{G}_{ih}^{(n)} V_{hk}^{(n)} \hat{G}_{kj}^{(n+1)}. \tag{228}$$

The system of linear equation in $\hat{G}_{ij}^{(n+1)}$ will create the renormalisation recursion relationships for the pivotal Green's functions. However, these recursions do not include the boundary conditions. Since the subgraphs of Figure 1 only connect to each other at the corners, it will transpire that the recursions in equation (228) only involve two pivotal Green's functions, namely, corner-to-corner and corner-to-same-corner; the so called input/output nodes. To proceed, we now need to determine $\hat{x}$ and $\hat{y}$ as defined in equations (211) and (212). Using equations (219) and (228) we get

$$\begin{aligned}
\hat{G}_{11}^{(n+1)} &= \bar{G}_{11}^{(n)} + \sum_{h,k} \beta \bar{G}_{1h}^{(n)} V_{hk}^{(n)} \hat{G}_{k1}^{(n+1)} \\
&= \hat{G}_{11}^{(n)} + \beta \bar{G}_{1d}^{(n)} V_{dr}^{(n)} \hat{G}_{r1}^{(n+1)} + \beta \bar{G}_{1b}^{(n)} V_{be}^{(n)} \hat{G}_{e1}^{(n+1)} \\
&= \hat{G}_{11}^{(n)} - \beta \hat{G}_{1N}^{(n)} \hat{G}_{r1}^{(n+1)} - \beta \hat{G}_{1m}^{(n)} \hat{G}_{e1}^{(n+1)}.
\end{aligned}$$

That is

$$\hat{X} = \hat{x} - 2\beta \hat{y} \hat{G}_{e1}^{(n+1)}, \tag{229}$$

since we know from equation (219) that $V_{dr}^{(n)} = V_{be}^{(n)} = -1$ and by symmetry $\bar{G}_{1d}^{(n)} = \hat{G}_{1N}^{(n)}$, $\hat{G}_{1N}^{(n)} = \hat{G}_{1m}^{(n)}$ and $\hat{G}_{r1}^{(n+1)} = \hat{G}_{e1}^{(n+1)}$. Similarly,

$$\begin{aligned}
\hat{G}_{e1}^{(n+1)} &= \bar{G}_{e1}^{(n)} + \sum_{h,k} \beta \bar{G}_{eh}^{(n)} V_{hk}^{(n)} \hat{G}_{k1}^{(n+1)} \\
&= \beta \bar{G}_{ee}^{(n)} V_{eb}^{(n)} \hat{G}_{b1}^{(n+1)} + \beta \bar{G}_{eq}^{(n)} V_{qz}^{(n)} \hat{G}_{z1}^{(n+1)} \\
&= -\beta \hat{G}_{11}^{(n)} \hat{G}_{b1}^{(n+1)} - \beta \hat{G}_{1N}^{(n)} \hat{G}_{z1}^{(n+1)}.
\end{aligned}$$

Therefore

$$\hat{G}_{e1}^{(n+1)} = -\beta\hat{x}\hat{G}_{b1}^{(n+1)} - \beta\hat{y}\hat{G}_{z1}^{(n+1)}. \tag{230}$$

Also

$$\begin{aligned}
\hat{G}_{b1}^{(n+1)} &= \bar{G}_{b1}^{(n)} + \sum_{h,k} \beta\bar{G}_{bh}^{(n)} V_{hk}^{(n)} \hat{G}_{k1}^{(n+1)} \\
&= \hat{G}_{m1}^{(n)} + \beta\bar{G}_{bb}^{(n)} V_{be}^{(n)} \hat{G}_{e1}^{(n+1)} + \beta\bar{G}_{bd}^{(n)} V_{dr}^{(n)} \hat{G}_{r1}^{(n+1)} \\
&= \hat{y} - \beta\hat{G}_{mm}^{(n)} \hat{G}_{e1}^{(n+1)} - \beta\hat{G}_{mN}^{(n)} \hat{G}_{e1}^{(n+1)}.
\end{aligned}$$

Hence

$$\hat{G}_{b1}^{(n+1)} = \hat{y} - \beta\hat{G}_{e1}^{(n+1)}(\hat{x} + \hat{y}), \tag{231}$$

since $\hat{G}_{r1}^{(n+1)} = \hat{G}_{e1}^{(n+1)}$. Finally,

$$\begin{aligned}
\hat{G}_{z1}^{(n+1)} &= \bar{G}_{z1}^{(n)} + \sum_{h,k} \beta\bar{G}_{zh}^{(n)} V_{hk}^{(n)} \hat{G}_{k1}^{(n+1)} \\
&= \beta\bar{G}_{zr}^{(n)} V_{rd}^{(n)} \hat{G}_{d1}^{(n+1)} + \beta\bar{G}_{zz}^{(n)} V_{zq}^{(n)} \hat{G}_{q1}^{(n+1)} \\
&= -\beta\hat{G}_{m1}^{(n)} \hat{G}_{b1}^{(n+1)} - \beta\hat{G}_{mm}^{(n)} \hat{G}_{z1}^{(n+1)}.
\end{aligned}$$

Therefore

$$\hat{G}_{z1}^{(n+1)} = -\beta\hat{y}\hat{G}_{b1}^{(n+1)} - \beta\hat{x}\hat{G}_{z1}^{(n+1)}, \tag{232}$$

since $\hat{G}_{d1}^{(n+1)} = \hat{G}_{b1}^{(n+1)}$ and $\hat{G}_{q1}^{(n+1)} = \hat{G}_{z1}^{(n+1)}$. Equations (229) to (232) provide four equations in the four unknows $\hat{X}, \hat{G}_{e1}^{(n+1)}, \hat{G}_{b1}^{(n+1)}$ and $\hat{G}_{z1}^{(n+1)}$. Rearranging equation (229) gives (for $\hat{y} \neq 0, \beta \neq 0$)

$$\hat{G}_{e1}^{(n+1)} = \frac{\hat{x} - \hat{X}}{2\beta\hat{y}}, \tag{233}$$

and substituting this into equation (231) gives

$$\hat{G}_{b1}^{(n+1)} = \hat{y} + (\hat{x} + \hat{y})\Big(\frac{\hat{X} - \hat{x}}{2\hat{y}}\Big). \tag{234}$$

Now rearranging equation (230) gives (for $\hat{y} \neq 0, \beta \neq 0$)

$$\hat{G}_{z1}^{(n+1)} = \frac{-1}{\beta\hat{y}}\Big(\hat{G}_{e1}^{(n+1)} + \beta\hat{x}\hat{G}_{b1}^{(n+1)}\Big), \tag{235}$$

and substituting equations (233) and (234) into equation (235) gives

$$\begin{aligned}\hat{G}_{z1}^{(n+1)} &= \frac{-1}{\beta\hat{y}}\Big[\frac{\hat{x}-\hat{X}}{2\beta\hat{y}} + \beta\hat{x}\hat{y} + \beta\hat{x}(\hat{x}+\hat{y})\Big(\frac{\hat{X}-\hat{x}}{2\hat{y}}\Big)\Big] \\ &= \frac{\hat{X}-\hat{x}}{2\beta^2\hat{y}^2}\big(1-\hat{x}\beta^2(\hat{x}+\hat{y})\big) - \hat{x}, \end{aligned} \tag{236}$$

and substituting equations (234) and (236) into equation (232) gives (where $\hat{X} = \hat{G}_{11}^{(n+1)}$)

$$\Big[\frac{(\hat{X}-\hat{x})}{2\beta^2\hat{y}^2}\big(1-\beta^2\hat{x}(\hat{x}+\hat{y})\big) - \hat{x}\Big](1+\beta\hat{x}) = -\beta\hat{y}\Big[\hat{y} + (\hat{x}+\hat{y})\frac{(\hat{X}-\hat{x})}{2\hat{y}}\Big] \tag{237}$$

so

$$(\hat{X}-\hat{x})\Big[\frac{\big(1-\beta^2\hat{x}(\hat{x}+\hat{y})\big)(1+\beta\hat{x})}{2\beta^2\hat{y}^2} + \frac{\beta\hat{y}(\hat{x}+\hat{y})}{2\hat{y}}\Big] = \hat{x}(1+\beta\hat{x}) - \beta\hat{y}^2 \tag{238}$$

and so

$$(\hat{X}-\hat{x})\Big[(1-\beta^2\hat{x}^2-\beta^2\hat{x}\hat{y})(1+\beta\hat{x}) + \beta^3\hat{y}^2(\hat{x}+\hat{y})\Big] = 2\beta^2\hat{y}^2(\hat{x}+\beta\hat{x}^2-\beta\hat{y}^2) \tag{239}$$

Expanding and factorising we get,

$$\hat{X} = \hat{x} + \frac{2\beta^2\hat{y}^2(\hat{x}+\beta\hat{x}^2-\beta\hat{y}^2)}{(1+\beta\hat{x}+\beta\hat{y})(1-\beta^2\hat{x}^2-\beta\hat{y}+\beta^2\hat{y}^2)}. \tag{240}$$

By substituting this into equations (233),(234) and (236) gives

$$\hat{G}_{e1}^{(n+1)} = \frac{-\beta\hat{y}(\hat{x}+\beta\hat{x}^2-\beta\hat{y}^2)}{(1+\beta\hat{x}+\beta\hat{y})(1-\beta^2\hat{x}^2-\beta\hat{y}+\beta^2\hat{y}^2)}, \tag{241}$$

and

$$\hat{G}_{b1}^{(n+1)} = \frac{\hat{y}(1+\beta\hat{x})}{(1+\beta\hat{x}+\beta\hat{y})(1-\beta^2\hat{x}^2-\beta\hat{y}+\beta^2\hat{y}^2)}, \tag{242}$$

and so

$$\hat{G}_{z1}^{(n+1)} = \frac{-\beta\hat{y}^2}{(1+\beta\hat{x}+\beta\hat{y})(1-\beta^2\hat{x}^2-\beta\hat{y}+\beta^2\hat{y}^2)}. \tag{243}$$

Now, for $\hat{Y} = \hat{G}_{m1}^{(n+1)}$, equation (228) gives

$$\begin{aligned}
\hat{G}_{m1}^{(n+1)} &= \bar{G}_{m1}^{(n)} + \sum_{h,k} \beta \bar{G}_{mh}^{(n)} V_{hk}^{(n)} \hat{G}_{k1}^{(n+1)} \\
&= \beta \bar{G}_{me}^{(n)} V_{eb}^{(n)} \hat{G}_{b1}^{(n+1)} + \beta \bar{G}_{mq}^{(n)} V_{qz}^{(n)} \hat{G}_{z1}^{(n+1)} \\
&= -\beta \hat{G}_{m1}^{(n)} \hat{G}_{b1}^{(n+1)} - \beta \hat{G}_{mN}^{(n)} \hat{G}_{z1}^{(n+1)}.
\end{aligned}$$

Therefore

$$\hat{Y} = -\beta\hat{y}(\hat{G}_{b1}^{(n+1)} + \hat{G}_{z1}^{(n+1)}). \tag{244}$$

Putting equations (242) and (243) into equation (244) gives

$$\hat{Y} = \frac{-\beta\hat{y}^2(1+\beta\hat{x}-\beta\hat{y})}{(1+\beta\hat{x}+\beta\hat{y})(1-\beta^2\hat{x}^2-\beta\hat{y}+\beta^2\hat{y}^2)}. \tag{245}$$

The boundary conditions can now be considered by rewriting the $(i,j)^{th}$ element of the matrix equation (227) as,

$$G_{ij}^{(n)} = \hat{G}_{ij}^{(n)} + \sum_{h,k} \hat{G}_{ih}^{(n)} \hat{B}_{hk}^{(n)} G_{kj}^{(n)} \tag{246}$$

and so we have,

$$\begin{aligned}
G_{11}^{(n)} &= \hat{G}_{11}^{(n)} + \sum_{h,k} \hat{G}_{ih}^{(n)} \hat{B}_{hk}^{(n)} G_{k1}^{(n)} \\
&= \hat{G}_{11}^{(n)} + \hat{G}_{11}^{(n)} \hat{B}_{11}^{(n)} G_{11}^{(n)} + \hat{G}_{1m}^{(n)} \hat{B}_{mm}^{(n)} G_{m1}^{(n)} + \hat{G}_{1N}^{(n)} \hat{B}_{NN}^{(n)} G_{N1}^{(n)}.
\end{aligned}$$

Therefore

$$x = \hat{x} + \hat{x}\bar{\gamma}_1 x + 2\hat{y}\bar{\gamma}_m y \tag{247}$$

since $\hat{B}_{11}^{(n)} = \bar{\gamma}_1, \hat{B}_{mm}^{(n)} = \hat{B}_{NN}^{(n)} = \bar{\gamma}_m$ from equation (206). Similarly,

$$\begin{aligned}
G_{1m}^{(n)} &= \hat{G}_{1m}^{(n)} + \sum_{h,k} \hat{G}_{mh}^{(n)} \hat{B}_{hk}^{(n)} G_{k1}^{(n)} \\
&= \hat{G}_{m1}^{(n)} + \hat{G}_{m1}^{(n)} \hat{B}_{11}^{(n)} G_{11}^{(n)} + \hat{G}_{mm}^{(n)} \hat{B}_{mm}^{(n)} G_{m1}^{(n)} + \hat{G}_{mN}^{(n)} \hat{B}_{NN}^{(n)} G_{N1}^{(n)}.
\end{aligned}$$

Hence

$$y = \hat{y} + \hat{y}\bar{\gamma}_1 x + \hat{x}\bar{\gamma}_m y + \hat{y}\bar{\gamma}_m y. \tag{248}$$

Letting $G^{(n)}_{mm} = z$ and $G^{(n)}_{mN} = w$ then,

$$\begin{aligned} G^{(n)}_{mm} &= \hat{G}^{(n)}_{mm} + \sum_{h,k} \hat{G}^{(n)}_{mh}\hat{B}^{(n)}_{hk}G^{(n)}_{km} \\ &= \hat{G}^{(n)}_{mm} + \hat{G}^{(n)}_{m1}\hat{B}^{(n)}_{11}G^{(n)}_{1m} + \hat{G}^{(n)}_{mm}\hat{B}^{(n)}_{mm}G^{(n)}_{mm} + \hat{G}^{(n)}_{mN}\hat{B}^{(n)}_{NN}G^{(n)}_{Nm}. \end{aligned}$$

Therefore

$$z = \hat{x} + \hat{y}\bar{\gamma}_1 y + \hat{x}\bar{\gamma}_m z + \hat{y}\bar{\gamma}_m w. \tag{249}$$

Finally,

$$\begin{aligned} G^{(n)}_{mN} &= \hat{G}^{(n)}_{mN} + \sum_{h,k} \hat{G}^{(n)}_{mh}\hat{B}^{(n)}_{hk}G^{(n)}_{kN} \\ &= \hat{G}^{(n)}_{mN} + \hat{G}^{(n)}_{m1}\hat{B}^{(n)}_{11}G^{(n)}_{1N} + \hat{G}^{(n)}_{mm}\hat{B}^{(n)}_{mm}G^{(n)}_{mN} + \hat{G}^{(n)}_{mN}\hat{B}^{(n)}_{NN}G^{(n)}_{NN}. \end{aligned}$$

Hence

$$w = \hat{y} + \hat{y}\bar{\gamma}_1 y + \hat{x}\bar{\gamma}_m w + \hat{y}\bar{\gamma}_m z. \tag{250}$$

The four equations (247),(248),(249) and (250) can be solved to express x, y, w, z in terms of $\hat{x}, \hat{y}, \bar{\gamma}_1, \bar{\gamma}_m$. Solving equations (247),(248) for x and y gives

$$x = \frac{\hat{x} + 2\hat{y}\bar{\gamma}_m y}{1 - \hat{x}\bar{\gamma}_1}. \tag{251}$$

Substituting equation (251) into equation (248) gives

$$y = \hat{y} + \hat{y}\bar{\gamma}_1\big(\frac{\hat{x} + 2\hat{y}\bar{\gamma}_m y}{1 - \hat{x}\bar{\gamma}_1}\big) + \hat{x}\bar{\gamma}_m y + \hat{y}\bar{\gamma}_m y. \tag{252}$$

Therefore

$$y = \frac{\hat{y}}{\big(1 - \hat{x}\bar{\gamma}_1\big)\big(1 - \bar{\gamma}_m(\hat{x} + \hat{y})\big) - 2\hat{y}^2\bar{\gamma}_1\bar{\gamma}_m}. \tag{253}$$

Rearranging equation (249) we get

$$z(1 - \hat{x}\bar{\gamma}_m) = \hat{x} + \hat{y}\bar{\gamma}_1 y + \hat{y}\bar{\gamma}_m w. \tag{254}$$

That is

$$z = \frac{\hat{x} + \hat{y}\bar{\gamma}_1 y + \hat{y}\bar{\gamma}_m w}{1 - \hat{x}\bar{\gamma}_m}. \tag{255}$$

Substituting equation (255) into (250) gives

$$w(1 - \hat{x}\bar{\gamma}_m) = \hat{y} + \hat{y}\bar{\gamma}_1 y + \hat{y}\bar{\gamma}_m\big(\frac{\hat{x} + \hat{y}\bar{\gamma}_1 y + \hat{y}\bar{\gamma}_m w}{1 - \hat{x}\bar{\gamma}_m}\big) \tag{256}$$

which can be written as

$$w = \frac{\hat{y}(1 + \bar{\gamma}_1 y)}{1 - \hat{x}\bar{\gamma}_m} + \frac{\hat{y}\bar{\gamma}_m\big(\hat{x} + \hat{y}(\bar{\gamma}_1 y + \bar{\gamma}_m w)\big)}{(1 - \hat{x}\bar{\gamma}_m)^2}. \tag{257}$$

Therefore

$$w = \frac{\hat{y}\big(1 + \bar{\gamma}_1 y(1 + \bar{\gamma}_m(\hat{y} - \hat{x}))\big)}{(\hat{x}\bar{\gamma}_m - 1 + \hat{y}\bar{\gamma}_m)(\hat{x}\bar{\gamma}_m - 1 - \hat{y}\bar{\gamma}_m)}. \tag{258}$$

7 Electrical Impedance and Transmission Sensitivity

In transmission mode there is no force incident on the front face of the transducer and so in equation (202) $A_L = 0$. The voltage $\bar{V}$ is defined as follows

$$\bar{V} = \int_0^L \bar{E} dx \tag{259}$$

and using equation (174) and then equation (154)

$$\begin{aligned} \bar{V} &= \int_0^L \big(- \bar{\zeta}\bar{S} + \frac{\bar{D}}{\bar{\varepsilon}_{11}}\big) dx \\ &= \int_0^L \big(- \bar{\zeta}\frac{\partial \bar{u}}{\partial x} + \frac{\bar{D}}{\bar{\varepsilon}_{11}}\big) dx. \end{aligned}$$

Now integrating and using Gauss' law gives

$$\begin{aligned} \bar{V} &= -\bar{\zeta}(U_N - U_1) + \frac{\bar{Q}L}{A_r \bar{\varepsilon}_{11}} \\ &= -\bar{\zeta}(U_N - U_1) + \frac{\bar{Q}}{\bar{C}_0}. \end{aligned} \tag{260}$$

Since the charge $\bar{Q} = \int \bar{I} dt = \sqrt{\rho^E / c_{44}^T}\, h \int \bar{I} d\theta$ where $\theta = c_T t/h$ then, by taking Laplace transforms, we get

$$\bar{Q} = \sqrt{\frac{\rho^E}{c_{44}^T}} h \frac{\bar{I}}{q}. \tag{261}$$

That is

$$\bar{I} = \frac{q\bar{Q}c_{44}^T \xi}{Z_T}, \tag{262}$$

where $Z_T = \sqrt{c_{44}^T \rho^E} A_r$. The electrical impedance of the device, denoted by Z_E, is given by

$$\begin{aligned} Z_E = \frac{\bar{V}}{\bar{I}} &= \frac{\bar{V}}{q\bar{Q}} \Big(\frac{c_{44}^T \xi}{Z_T} \Big)^{-1} \\ &= \Big(\frac{-\bar{\zeta}\bar{C}_0 (U_N - U_1) + \bar{Q}}{\bar{Q}\bar{C}_0 q} \Big) \Big(\frac{c_{44}^T \xi}{Z_T} \Big)^{-1} \\ &= \Big(\frac{Z_T}{\bar{C}_0 q c_{44}^T \xi} \Big) \Big(1 - \frac{\bar{\zeta}\bar{C}_0 (U_N - U_1)}{\bar{Q}} \Big). \end{aligned} \tag{263}$$

Now using equation (210)

$$\begin{aligned} U_1^{(n)} &= G_{11}^{(n)} \bar{\delta}_1 + G_{1m}^{(n)} \bar{\delta}_m + G_{1N}^{(n)} \bar{\delta}_N \\ &= G_{11}^{(n)} \bar{\delta}_1 + \bar{\delta}_m (G_{1m}^{(n)} + G_{1N}^{(n)}) \\ &= G_{11}^{(n)} \bar{\delta}_1 + 2 G_{1m}^{(n)} \bar{\delta}_m \end{aligned}$$

since $G_{1m}^{(n)} = G_{1N}^{(n)}$ and $\bar{\delta}_N = \bar{\delta}_m$. From equation (202), then

$$U_1^{(n)} = -\frac{\bar{\zeta}\bar{Q}\eta}{\bar{c}_{44}^T \xi} \Big(\Big(1 - q \frac{Z_B}{\bar{\bar{Z}}_T} \Big)^{-1} G_{11}^{(n)} - \Big(1 - q \frac{Z_L}{\bar{\bar{Z}}_T} \Big)^{-1} 2 G_{1m}^{(n)} \Big). \tag{264}$$

Similarly,

$$\begin{aligned} U_N^{(n)} &= G_{N1}^{(n)} \bar{\delta}_1 + G_{Nm}^{(n)} \bar{\delta}_m + G_{NN}^{(n)} \bar{\delta}_N \\ &= G_{N1}^{(n)} \bar{\delta}_1 + \bar{\delta}_m (G_{Nm}^{(n)} + G_{NN}^{(n)}). \end{aligned}$$

Therefore

$$U_N^{(n)} = -\frac{\bar{\zeta}\bar{Q}\eta}{\bar{c}_{44}^T \xi} \Big(\Big(1 - q \frac{Z_B}{\bar{\bar{Z}}_T} \Big)^{-1} G_{N1}^{(n)} - \Big(1 - q \frac{Z_L}{\bar{\bar{Z}}_T} \Big)^{-1} (G_{Nm}^{(n)} + G_{NN}^{(n)}) \Big). \tag{265}$$

Substituting equations (264) and (265) into equation (263) gives

$$\begin{aligned} Z_E &= \Big(\frac{Z_T}{\bar{C}_0 q c_{44}^T \xi}\Big)\Big(1+\frac{\bar{\zeta}^2\bar{C}_0\eta}{\bar{c}_{44}^T\xi}\Big(\Big(1-q\frac{Z_B}{\bar{\bar{Z}}_T}\Big)^{-1}(G_{N1}^{(n)}-G_{11}^{(n)}) \\ &\quad +\Big(1-q\frac{Z_L}{\bar{\bar{Z}}_T}\Big)^{-1}(-G_{Nm}^{(n)}-G_{NN}^{(n)}+2G_{1m}^{(n)})\Big)\Big) \\ &= \Big(\frac{Z_T}{\bar{C}_0 q c_{44}^T \xi}\Big)\Big(1+\frac{\bar{\zeta}^2\bar{C}_0\eta}{\bar{c}_{44}^T\xi}(\sigma_1+\sigma_2)\Big). \end{aligned} \tag{266}$$

Hence, the non-dimensionalised electrical impedance is given by

$$\hat{Z}_E(f;n) = Z_E/Z_0 = \Big(\frac{Z_T}{\bar{C}_0 q c_{44}^T \xi Z_0}\Big)\Big(1+\frac{\bar{\zeta}^2\bar{C}_0\eta}{\bar{c}_{44}^T\xi}(\sigma_1+\sigma_2)\Big) \tag{267}$$

where $\sigma_1 = \big(1-q(Z_B/\bar{\bar{Z}}_T)\big)^{-1}(G_{N1}^{(n)}-G_{11}^{(n)})$ and $\sigma_2 = \big(1-q(Z_L/\bar{\bar{Z}}_T)\big)^{-1}(-G_{Nm}^{(n)}-G_{NN}^{(n)}+2G_{1m}^{(n)})$. Continuity of force at the front face given by equation (196) and continuity of displacement given by equation (193) (with $A_L = 0$) gives

$$F = F_L(x_L = 0) = A_r Y_L\Big(\frac{qc_T}{hc_L}\Big)U_C. \tag{268}$$

Substituting equation (200) into equation (268) gives

$$F = A_r Y_L\Big(\frac{qc_T}{hc_L}\Big)(\gamma_m U_m + \delta_m). \tag{269}$$

From equations (201) and (202) with $A_L = 0$, then

$$F = A_r Y_L\Big(\frac{qc_T}{hc_L}\Big)\Big(\Big(1-q\frac{Z_L}{\bar{\bar{Z}}_T}\Big)^{-1}U_m + \frac{\bar{\zeta}\bar{Q}}{\bar{c}_{44}^T\xi}\Big(1-q\frac{Z_L}{\bar{\bar{Z}}_T}\Big)^{-1}\Big). \tag{270}$$

Therefore

$$F = \frac{\xi Y_L q c_T}{c_L}\Big(1-q\frac{Z_L}{\bar{\bar{Z}}_T}\Big)^{-1}\Big(U_m + \frac{\bar{\zeta}\bar{Q}}{\bar{c}_{44}^T\xi}\Big), \tag{271}$$

since $\xi = A_r/h$. To obtain U_m we make use of equation (210) to obtain

$$U_m^{(n)} = \frac{\bar{\zeta}\bar{Q}\eta}{\bar{c}_{44}^T\xi}\Big(-\Big(1-q\frac{Z_B}{\bar{\bar{Z}}_T}\Big)^{-1}G_{m1}^{(n)} + \Big(1-q\frac{Z_L}{\bar{\bar{Z}}_T}\Big)^{-1}(G_{mm}^{(n)}+G_{mN}^{(n)})\Big). \tag{272}$$

Therefore equation (271) becomes

$$F = \frac{Y_L q c_T}{c_L}\Big(\frac{\bar{\zeta}\bar{Q}}{\bar{c}_{44}^T}\Big)\Big(1-q\frac{Z_L}{\bar{\bar{Z}}_T}\Big)^{-1}\Big(-\eta\Big(\Big(1-q\frac{Z_B}{\bar{\bar{Z}}_T}\Big)^{-1}G_{m1}^{(n)} - \Big(1-q\frac{Z_L}{\bar{\bar{Z}}_T}\Big)^{-1}(G_{mm}^{(n)}+G_{mN}^{(n)})\Big)+1\Big). \quad (273)$$

From equations (262) and (179)

$$\bar{Q} = \frac{\bar{I}Z_T}{qc_{44}^T\xi} = \frac{a\bar{V}}{(Z_E+b)}\frac{Z_T}{qY_T\xi}, \quad (274)$$

then substituting in equation (273) gives

$$\frac{F}{\bar{V}} = \frac{Z_T Z_L \bar{\zeta} a}{\bar{\bar{Z}}_T(Z_E+b)c_{44}^T\xi}\Big(1-q\frac{Z_L}{\bar{\bar{Z}}_T}\Big)^{-1}\Big(-\eta\Big(\Big(1-q\frac{Z_B}{\bar{\bar{Z}}_T}\Big)^{-1}G_{m1}^{(n)} - \Big(1-q\frac{Z_L}{\bar{\bar{Z}}_T}\Big)^{-1}(G_{mm}^{(n)}+G_{mN}^{(n)})\Big)+1\Big), \quad (275)$$

and so

$$\frac{F}{\bar{V}} = \frac{Z_T Z_L \bar{\zeta} a}{\bar{\bar{Z}}_T(Z_E+b)c_{44}^T\xi}K^{(n)} \quad (276)$$

where

$$K^{(n)} = \Big(1-q\frac{Z_L}{\bar{\bar{Z}}_T}\Big)^{-1}\Big(-\eta\Big(\Big(1-q\frac{Z_B}{\bar{\bar{Z}}_T}\Big)^{-1}G_{m1}^{(n)} - \Big(1-q\frac{Z_L}{\bar{\bar{Z}}_T}\Big)^{-1}(G_{mm}^{(n)}+G_{mN}^{(n)})\Big)+1\Big). \quad (277)$$

The non-dimensionalised transmission sensitivity ψ is then given by

$$\psi(f;n) = \Big(\frac{F}{\bar{V}}\Big)/\bar{\zeta}\bar{C}_0 = \frac{aZ_L Z_T}{\bar{\bar{Z}}_T(Z_E+b)c_{44}^T\xi\bar{C}_0}K^{(n)}. \quad (278)$$

7.1 Reception Sensitivity

In reception mode A_L is now non zero because the front face will be subject to a force (given by the incoming signal). From equations (202) and (210)

$$U_1^{(n)} = -\frac{\bar{\zeta}\bar{Q}\eta}{\bar{c}_{44}^T\xi}\Big(1-q\frac{Z_B}{\bar{\bar{Z}}_T}\Big)^{-1}G_{11}^{(n)} + \Big(\frac{\bar{\zeta}\bar{Q}}{\bar{c}_{44}^T\xi} - 2A_L q\frac{Z_L}{\bar{\bar{Z}}_T}\Big)\eta\Big(1-q\frac{Z_L}{\bar{\bar{Z}}_T}\Big)^{-1}2G_{1m}^{(n)} \quad (279)$$

and

$$U_N^{(n)} = -\frac{\bar{\zeta}\bar{Q}\eta}{\bar{c}_{44}^T\xi}\Big(1-q\frac{Z_B}{\bar{\bar{Z}}_T}\Big)^{-1}G_{N1}^{(n)}+\Big(\frac{\bar{\zeta}\bar{Q}}{\bar{c}_{44}^T\xi}-2A_Lq\frac{Z_L}{\bar{\bar{Z}}_T}\Big)\eta\Big(1-q\frac{Z_L}{\bar{\bar{Z}}_T}\Big)^{-1}(G_{Nm}^{(n)}+G_{NN}^{(n)}). \tag{280}$$

Putting these into equation (260) gives

$$\begin{aligned}\bar{V} &= \frac{\bar{\zeta}^2\bar{Q}\eta}{\bar{c}_{44}^T\xi}\Big(1-q\frac{Z_B}{\bar{\bar{Z}}_T}\Big)^{-1}(G_{N1}^{(n)}-G_{11}^{(n)})+\Big(\frac{\bar{\zeta}^2\bar{Q}}{\bar{c}_{44}^T\xi}-2\bar{\zeta}A_Lq\frac{Z_L}{\bar{\bar{Z}}_T}\Big)\eta\Big(1-q\frac{Z_L}{\bar{\bar{Z}}_T}\Big)^{-1}\\ &\quad (2G_{1m}^{(n)}-G_{Nm}^{(n)}-G_{NN}^{(n)})+\frac{\bar{Q}}{\bar{C}_0}.\end{aligned}$$

Then

$$\bar{V} = \frac{\bar{\zeta}^2\bar{Q}\eta}{\bar{c}_{44}^T\xi}\sigma_1+\frac{\bar{\zeta}^2\bar{Q}\eta}{\bar{c}_{44}^T\xi}\sigma_2-2\bar{\zeta}A_Lq\frac{Z_L}{\bar{\bar{Z}}_T}\eta\sigma_2+\frac{\bar{Q}}{\bar{C}_0} \tag{281}$$

and so

$$\bar{V} = \frac{\bar{\zeta}^2\bar{Q}\eta}{\bar{c}_{44}^T\xi}(\sigma_1+\sigma_2)-2\bar{\zeta}A_Lq\frac{Z_L}{\bar{\bar{Z}}_T}\eta\sigma_2+\frac{\bar{Q}}{\bar{C}_0}. \tag{282}$$

From equation (195) the force in the load ($\zeta = 0$) is given by

$$F = A_rY_L\frac{\partial\bar{u}_L}{\partial x}. \tag{283}$$

From equation (189)

$$\frac{\partial\bar{u}_L}{\partial x} = \Big(\frac{qc_T}{hc_L}\Big)\Big(B_Le^{(-qc_Tx_L/hc_L)}-A_Le^{(-qc_Tx_L/hc_L)}\Big), \tag{284}$$

and so, at $x_L = 0$,

$$\frac{\partial\bar{u}_L}{\partial x} = \Big(\frac{qc_T}{hc_L}\Big)\Big(-A_L\Big), \tag{285}$$

since in receiving mode $B_L = 0$. Substituting this equation into equation (283) we get

$$F = \frac{\xi qc_TZ_L}{A_r}\Big(-A_L\Big) \tag{286}$$

since $\xi = A_r/h$ and $Z_L = Y_LA_r/c_L$. Then

$$A_L = \frac{-FA_r}{\xi qc_TZ_L}. \tag{287}$$

Substituting this and equation (274) into equation (282) gives

$$\bar{V} = \frac{a\bar{V}Z_T}{(Z_E+b)qc_{44}^T\xi}\Big(\frac{\bar{\zeta}^2\eta}{\bar{c}_{44}^T\xi}(\sigma_1+\sigma_2)+\frac{1}{\bar{C}_0}\Big)+\frac{2F\bar{\zeta}\eta\sigma_2}{\xi\bar{c}_{44}^T}, \tag{288}$$

since $\bar{c}_{44}^T = \bar{\bar{Z}}_T c_T/A_r$, and so

$$\bar{V}\Big[1-\frac{aZ_T}{(Z_E+b)qc_{44}^T\xi}\Big(\frac{\bar{\zeta}^2\eta}{\bar{c}_{44}^T\xi}(\sigma_1+\sigma_2)+\frac{1}{\bar{C}_0}\Big)\Big] = \frac{2F\bar{\zeta}\eta\sigma_2}{\xi\bar{c}_{44}^T}, \tag{289}$$

and hence

$$\frac{\bar{V}}{F} = \frac{2\bar{\zeta}\eta\sigma_2}{\xi\bar{c}_{44}^T}\Big(1-\frac{aZ_T\bar{\zeta}^2\eta(\sigma_1+\sigma_2)}{(Z_E+b)qc_{44}^T\bar{c}_{44}^T\xi^2}-\frac{aZ_T}{(Z_E+b)qc_{44}^T\xi\bar{C}_0}\Big)^{-1}. \tag{290}$$

The non-dimensionalised reception sensitivity ϕ is then

$$\begin{aligned}\phi(f;n) &= \Big(\frac{\bar{V}}{F}\Big)(\bar{e}_{24}L)\\ &= \frac{2\bar{\zeta}\bar{e}_{24}L\eta\sigma_2}{\xi\bar{c}_{44}^T}\Big(1-\frac{aZ_T\bar{\zeta}^2\eta(\sigma_1+\sigma_2)}{(Z_E+b)qc_{44}^T\bar{c}_{44}^T\xi^2}-\frac{aZ_T}{(Z_E+b)qc_{44}^T\xi\bar{C}_0}\Big)^{-1}\end{aligned} \tag{291}$$

8 Steady State Solutions

The true fractal case arises when we allow the fractal generation level n to tend to infinity and we assume that the renormalisation recursion relationships converge to a steady state (we denote these steady state solutions by a $*$ superscript). Note we will examine the convergence of these recursion relationships later (see section 9.3) when we consider the pre-fractal $SG(3,4)$ transducer (at increasing but finite fractal generation levels).

Case A: $\hat{y}^* = 0$

If $\hat{y}^* = 0$ then equation (229) is automatically satisfied (since $\hat{X} = \hat{x} = \hat{x}^*$) and from equations (230) and (231) we get

$$\hat{G}_{e1}^* = -\beta\hat{x}^*\hat{G}_{b1}^* \tag{292}$$

and

$$\hat{G}^*_{b1} = -\beta \hat{x}^* \hat{G}^*_{e1}. \tag{293}$$

Substituting equation (292) into equation (293) gives

$$\hat{G}^*_{b1}(1 - \beta^2 \hat{x}^{*2}) = 0. \tag{294}$$

Therefore $\hat{G}^*_{b1} = 0$ or $\hat{x}^* = \pm 1/\beta$. In the former case then $\hat{G}^*_{e1} = 0$ and in the latter case $\hat{G}^*_{b1} = \mp \hat{G}^*_{e1}$. From equation (232) we get

$$\hat{G}^*_{z1}(1 + \beta \hat{x}^*) = 0. \tag{295}$$

Therefore $\hat{G}^*_{z1} = 0$ or $\hat{x}^* = -1/\beta$. Now bringing in the boundary conditions equation (255) gives

$$z = \frac{\hat{x}^*}{1 - \hat{x}^* \bar{\gamma}_m} \tag{296}$$

where $\hat{x}^* \neq 1/\bar{\gamma}_m$. From equation (251) we get

$$x = \frac{\hat{x}^*}{1 - \hat{x}^* \bar{\gamma}_1} \tag{297}$$

where $\hat{x}^* \neq 1/\bar{\gamma}_1$. From equation (248) we get

$$y = \hat{x}^* \bar{\gamma}_m y. \tag{298}$$

That is

$$y = 0 \tag{299}$$

and from equation (250) we get

$$w = \hat{x}^* \bar{\gamma}_m w, \tag{300}$$

giving

$$w = 0. \tag{301}$$

In the case where $\hat{G}^*_{b1} = \hat{G}^*_{e1} = \hat{G}^*_{z1} = 0$ we denote the solution as $x^* = \chi$, $\chi \in \mathbb{C}$ and in the case where $\hat{x}^* = \pm 1/\beta$ we denote the solutions as $\hat{G}^*_{b1} = \mp\lambda$, $\hat{G}^*_{e1} = \mp\lambda$ and $\hat{G}^*_{z1} = \theta$ (or 0 when $\hat{x}^* = 1/\beta$) where $\lambda, \theta \in \mathbb{C}$. The full set of steady state solutions for this branch of solutions are summarised in the table below.

Case	$\hat{x}^*$	$\hat{y}^*$	$\hat{G}^*_{b1}$	$\hat{G}^*_{e1}$	$\hat{G}^*_{z1}$	x	y	w	z	note
A1	$\frac{-1}{\beta}$	0	λ	$-\lambda$	θ	$\frac{-1}{\beta+\bar{\gamma}_1}$	0	0	$\frac{-1}{\beta+\bar{\gamma}_m}$	$\beta \neq \bar{\gamma}_1, \beta \neq \bar{\gamma}_m$
A2	$\frac{1}{\beta}$	0	$-\lambda$	λ	0	$\frac{1}{\beta-\bar{\gamma}_1}$	0	0	$\frac{1}{\beta-\bar{\gamma}_m}$	$\beta \neq \bar{\gamma}_1, \beta \neq \bar{\gamma}_m$
A3	χ	0	0	0	0	$\frac{\chi}{1-\chi\bar{\gamma}_1}$	0	0	$\frac{\chi}{1-\chi\bar{\gamma}_m}$	$\bar{\gamma}_1 \neq \frac{1}{\chi}, \bar{\gamma}_m \neq \frac{1}{\chi}, \chi \neq \pm\frac{1}{\beta}$

Case B: $\hat{y}^* \neq 0$

If $\hat{y}^* \neq 0$ then from equation (229) we get

$$-2\beta\hat{y}^*\hat{G}^*_{e1} = 0, \tag{302}$$

and so

$$\hat{G}^*_{e1} = 0. \tag{303}$$

Substituting this into equations (230) and (231) we get

$$\hat{x}^*\hat{G}^*_{b1} + \hat{y}^*\hat{G}^*_{z1} = 0 \tag{304}$$

and

$$\hat{G}^*_{b1} = \hat{y}^*. \tag{305}$$

Substituting equation (305) into equation (304) gives

$$\hat{G}^*_{z1} = -\hat{x}^*. \tag{306}$$

Substituting equations (305) and (306) into equation (232) gives

$$\hat{x}^* + \beta\hat{x}^{*2} - \beta\hat{y}^{*2} = 0. \tag{307}$$

Note that $\hat{x}^* \neq 0$ since this would imply that $\hat{y}^*$ was zero. Also substituting equations (305) and (306) into equation (244) gives

$$\hat{y}^* = -\beta\hat{y}^*(\hat{y}^* - \hat{x}^*). \tag{308}$$

That is

$$\hat{y}^* = \hat{x}^* - \frac{1}{\beta}. \tag{309}$$

Putting this into equation (307) gives

$$\hat{x}^* = \frac{1}{3\beta}. \tag{310}$$

Putting this into equation (309) gives

$$\hat{y}^* = \frac{-2}{3\beta}. \tag{311}$$

Now putting equations (310) and (311) into the boundary conditions equation (253) gives

$$y = \frac{-2\beta}{3\beta^2 - 3\bar{\gamma}_1\bar{\gamma}_m + \beta(-\bar{\gamma}_1 + \bar{\gamma}_m)}. \tag{312}$$

Putting equations (310),(311) and (312) into equations (251) and (258) gives

$$x = \frac{\beta + 3\bar{\gamma}_m}{3\beta^2 - \beta\bar{\gamma}_1 + \beta\bar{\gamma}_m - 3\bar{\gamma}_1\bar{\gamma}_m} \tag{313}$$

and

$$w = \frac{-2\beta(\beta - \bar{\gamma}_1)}{(\beta - \bar{\gamma}_m)\big(3\beta^2 - 3\bar{\gamma}_1\bar{\gamma}_m + \beta(-\bar{\gamma}_1 - \bar{\gamma}_m)\big)}. \tag{314}$$

Substituting equations (310),(311),(312) and (314) into equation (255) gives

$$z = \frac{\beta^2 - 3\bar{\gamma}_1\bar{\gamma}_m + \beta(\bar{\gamma}_1 + \bar{\gamma}_m)}{(\beta - \bar{\gamma}_m)\big(3\beta^2 - 3\bar{\gamma}_1\bar{\gamma}_m + \beta(-\bar{\gamma}_1 + \bar{\gamma}_m)\big)}. \tag{315}$$

Note that from equation (214), $h^{(n)} \to 0$ and $q^{(n)} \to 0$ as $n \to \infty$, and so from equation (267) the non-dimensionalised electrical impedance tends to infinity ($(\hat{Z}_E(f;n)) \to \infty$), from equation (278) the non-dimensionalised transmission sensitivity tends to zero ($\psi(f;n) \to 0$), and from equation (201) $\gamma_j \to 1$ and from equation (203) $\bar{\gamma}_j \to \eta^*$. From equation (119) we get

$$\eta^* = \frac{2}{3}. \tag{316}$$

From equation (291) the non-dimensionalised reception sensitivity is

$$\phi^*(f;n) = \frac{2\bar{\zeta}\bar{e}_{24}L\eta^*\sigma_2^*}{\xi\bar{c}_{44}^T}\Big(1 - \frac{aZ_T(\xi\bar{c}_{44}^T + \bar{C}_0\bar{\zeta}^2\eta^*(\sigma_1^* + \sigma_2^*))}{\xi\bar{c}_{44}^T Z_T + \xi^2 c_{44}^T\bar{c}_{44}^T bq\bar{C}_0 + \bar{C}_0\bar{\zeta}^2\eta^* Z_T(\sigma_1^* + \sigma_2^*)}\Big)^{-1}, \tag{317}$$

and, since $q^{(n)} \to 0$, then

$$\phi^*(f;n) = \frac{4\bar{\zeta}\bar{e}_{24}L\sigma_2^*}{3\xi\bar{c}_{44}^T(1-a)}, \tag{318}$$

where

$$\sigma_2^* = \begin{cases} \frac{1}{1+\beta}, & \text{in case A1} \\ \frac{1}{1-\beta}, & \text{in case A2} \\ \frac{\chi}{\chi-1}, & \text{in case A3} \\ \frac{-3(3\beta+4)}{9\beta^2+\beta-12} & \text{in case B.} \end{cases} \tag{319}$$

9 Results

From a practical perspective, these fractal transducers will only be able to be manufactured at low fractal generation levels. The formulation presented above will allow us to compare the fractal design (using the renormalisation derivation) with a conventional (Euclidean) design (using homogenisation) in terms of the

key operating characteristics of the reception and transmission sensitivity spectra [16]. Within each, the presence of higher amplitudes, multiple resonances, and improved bandwidth (the range of frequencies over which the performance exceeds a certain decibel level) are the key performance indicators of interest in this section. A careful examination of the transmission and reception sensitivities of the fractal device as the fractal generation level is increased has been performed. However, to keep the presentation here succinct and to produce results that are pertinent to devices that can be physically produced, we will focus on fractal generation levels $n = 4, 5, 6$. A typical profile of the electrical impedance spectrum (magnitude) given by equation (267) is shown in Figures 46 ($n = 4$), 49 ($n = 5$) and 52 ($n = 6$) (dashed line); it is compared to the equivalent profile given by a model of the traditional design (180) (full line). The overall trend of the curve is that of a capacitor ($1/f$ profile) with a prominent resonance. The important features of this plot that the design engineer is interested in are the location and magnitude of the first minimum (f_r) and the first maximum (f_a) turning points. The first minimum is where the mechanical resonance (or series resonance) occurs and, as this provides the least resistance to the electrical energy being supplied, is the frequency at which the device should be used in transmission mode. This device will produce its maximum force on the mechanical load at this frequency. The absolute value of the electrical impedance at this frequency is also important therefore and the lower it is the higher will be the peak transmission sensitivity of the device. The first maximum (known as the anti-resonance or parallel resonance frequency) is where the electrical impedance of the device peaks and is therefore the optimal frequency to operate the device in reception mode. As can be seen in Figures 46, 49 and 52 for the traditional design (full line) $f_r^{(4)} = 1.7$ MHz, $|Z_E(f_r; 4)| = 31.5$ dB, $f_a^{(4)} = 2.5$

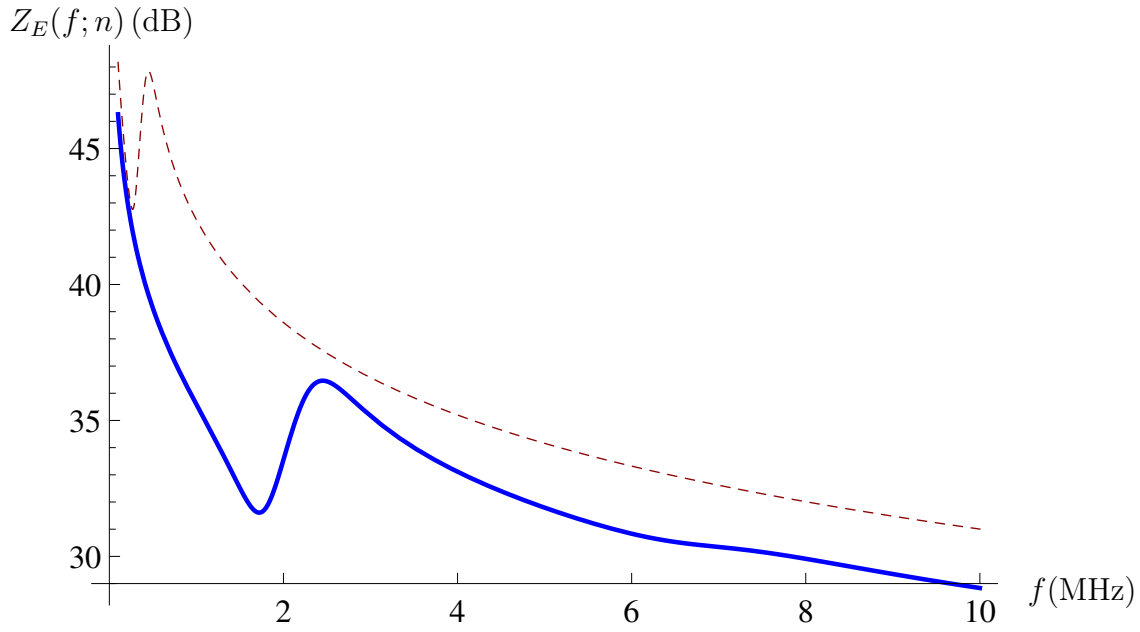

Figure 46: Non-dimensionalised electrical impedance (equation (267)) versus frequency for the $SG(3)$ lattice transducer at fractal generation level $n = 4$ (dashed line). The non-dimensionalised electrical impedance of the standard (Euclidean) transducer (equation (180)) is plotted for comparison (full line). Parameter values are given in Table 4.

MHz, $f_r^{(5)} = 1.7$ MHz, $|Z_E(f_r;5)| = 35$ dB, $f_a^{(5)} = 2.5$ MHz, $f_r^{(6)} = 1.7$ MHz, $|Z_E(f_r;6)| = 38$ dB and $f_a^{(6)} = 2.5$ MHz. As discussed above, these frequencies correspond precisely to the first maximum in the transmission sensitivity plots (Figures 47, 50 and 53, full line) and the reception sensitivity plots (Figures 48, 51 and 54 full line). From the parameter values for PZT5-H (see [4]) then in equation (23) the piezoelectrically stiffened velocity (c_T) is approximately 2370 m/s and the polymer stiffened velocity (c_P) is approximately 992 m/s and, with an overall device length of $L = 0.5$ mm, then the first mechanical resonant frequency is approximately $f_a = c_T/(2L) = 2.4$ MHz. This agrees reasonably well

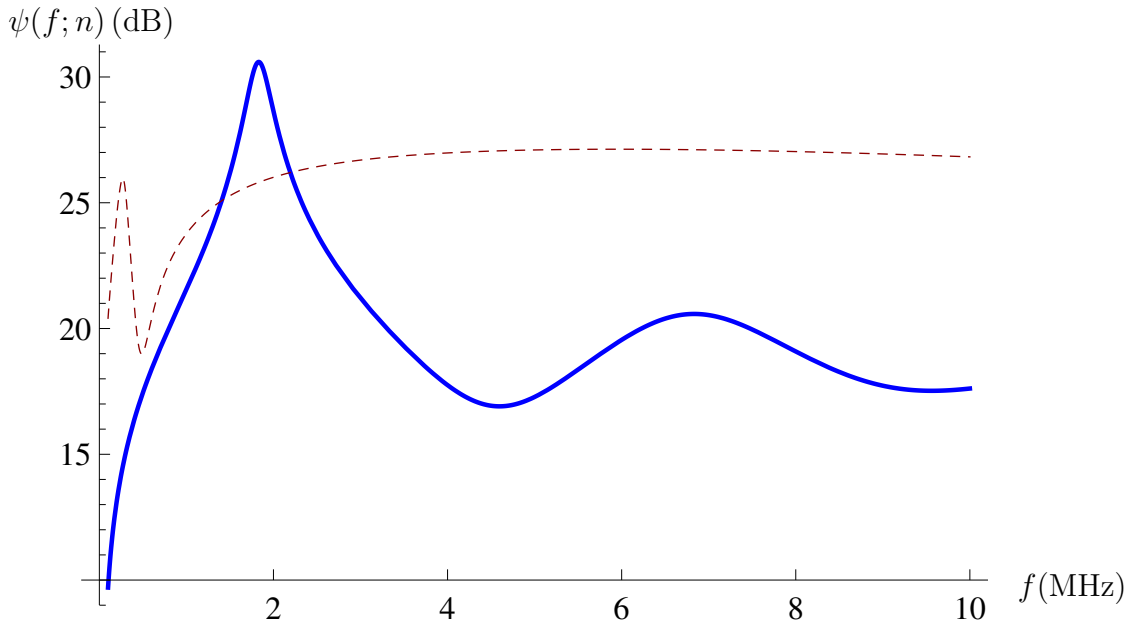

Figure 47: Non-dimensionalised transmission sensitivity (equation (278)) versus frequency for the $SG(3)$ lattice transducer at fractal generation level $n = 4$ (dashed line). The non-dimensionalised transmission sensitivity of the standard (Euclidean) transducer (equation (183)) is plotted for comparison (full line). Parameter values are given in Table 4.

with the reception sensitivity maximum for the homogenised estimate for f_a. For the Sierpinski gasket design the electrical impedance resonance frequencies are much lower ($f_r^{(4)} = 0.25$ MHz, $f_r^{(5)} = 0.54$ MHz, $f_r^{(6)} = 1.2$ MHz and $f_a^{(4)} = 0.45$ MHz, $f_a^{(5)} = .93$ MHz, $f_a^{(6)} = 2$ MHz) and this suggests that it is a complex interaction between the edge lengths in the graph associated with the various generation levels that are causing these resonances; so the internal geometry is dictating the device behaviour as anticipated. Importantly, the magnitude of the electrical impedance at the electrical resonance frequency is higher than the traditional design; there is about a 5 dB increase for $n = 6$. This results in the

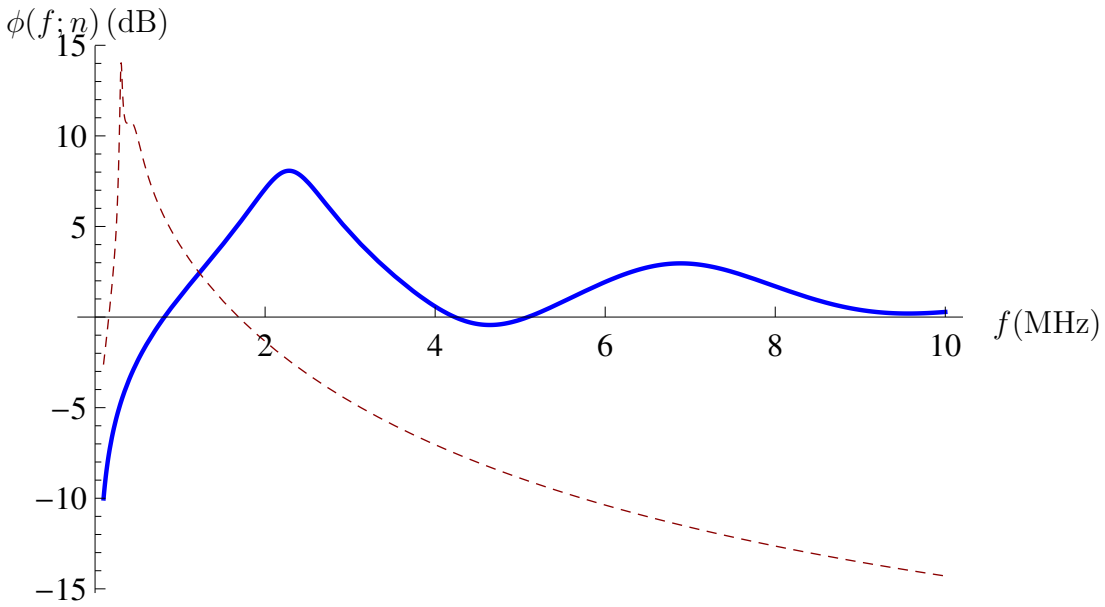

Figure 48: Non-dimensionalised reception sensitivity (equation (291)) versus frequency for the $SG(3)$ lattice transducer at fractal generation level $n = 4$ (dashed line). The non-dimensionalised reception sensitivity of the standard (Euclidean) transducer (equation (184)) is plotted for comparison (full line). Parameter values are given in Table 4.

reception sensitivity spectrum having a much larger gain for $n = 6$; there is a 7 dB improvement in the transmission sensitivity gain from the traditional design to the fractal design (see Figure 54). Importantly, this peak in the reception sensitivity also results in an enhanced bandwidth; if we take the noise floor to be 3 dB below the peak gain of the traditional design (that is 5 dB) then the operational bandwidth of the traditional design is 1.5 MHz (or 70%) whereas the fractal design has an operational bandwidth of around 3 MHz (or 140%). It should be borne in mind of course that no matching layers (or indeed an optimised backing layer) have been used in this design, and that the transducer is solely composed of the piezoelectric-polymer composite material.

9.1 Electrical Impedance and Transmission/Reception Sensitivities

Let us start by examining the performance of the first generation lattice ($n = 4$). Figure 46 shows that the electrical impedance of the fractal lattice has its first resonance (the electrical resonance) at around $f_r^{(4)} = 0.25$ MHz (at a lower frequency than the Euclidean case $f_r^{(4)} = 1.7$ MHz) and that the higher frequency resonances are absent. Figure 47 shows that the transmission sensitivity of the fractal design has a maximum amplitude (gain) that is lower than the Euclidean case (standard design) at its lower operating frequency (26 dB at 0.23 MHz compared to 31 dB at 1.8 MHz for the Euclidean case). Although if we take the noise floor to be 3 dB below the peak gain of the traditional design then the operational bandwidth of the traditional design is 0.5 MHz whereas the fractal design has no operational bandwidth. Figure 48 shows that the reception sensitivity the fractal design does show some encouraging results with a much higher peak amplitude than that of the Euclidean case and at a lower operating frequency (at 0.32 MHz its sensitivity is 14 dB whereas the peak sensitivity of the standard device is 8 dB at 2.3 MHz). Following this is an examination of the next generation level ($n = 5$). Also in generation level $n = 5$ the electrical impedance of the fractal lattice has its first resonance at around 0.5 MHz (at a lower frequency than the Euclidean case) and that the higher frequency resonances are absent.

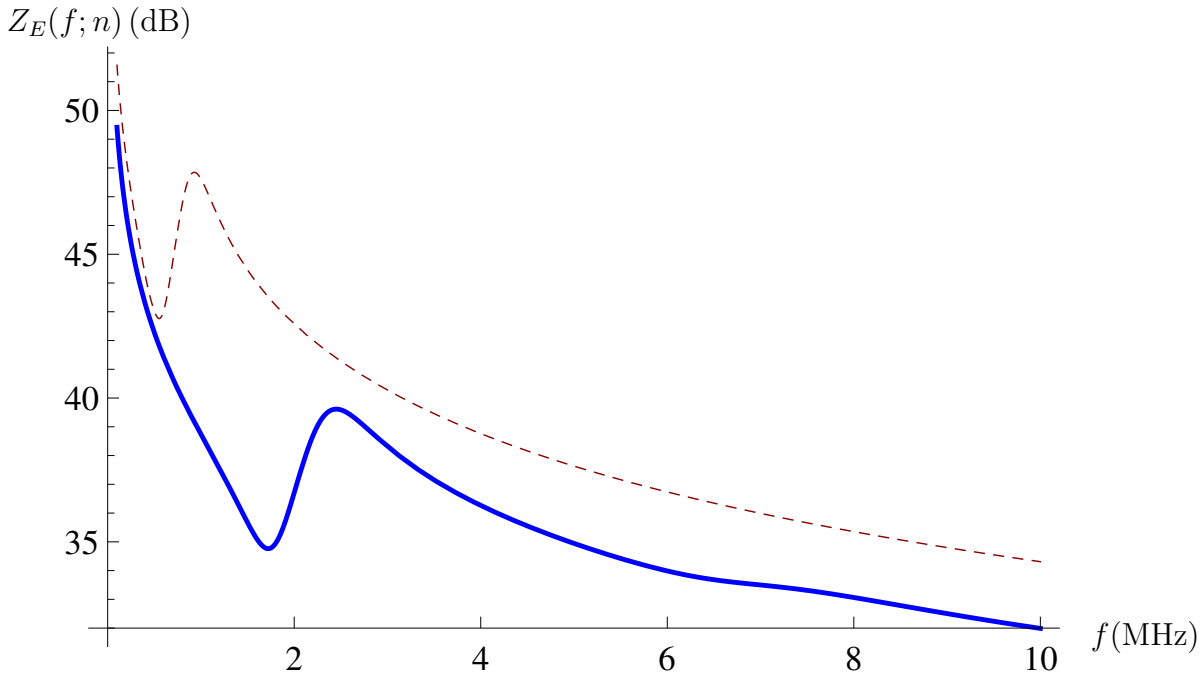

Figure 49: Non-dimensionalised electrical impedance (equation (267)) versus frequency for the $SG(3)$ lattice transducer at fractal generation level $n = 5$ (dashed line). The non-dimensionalised electrical impedance of the standard (Euclidean) transducer (equation (180)) is plotted for comparison (full line). Parameter values are given in Table 4.

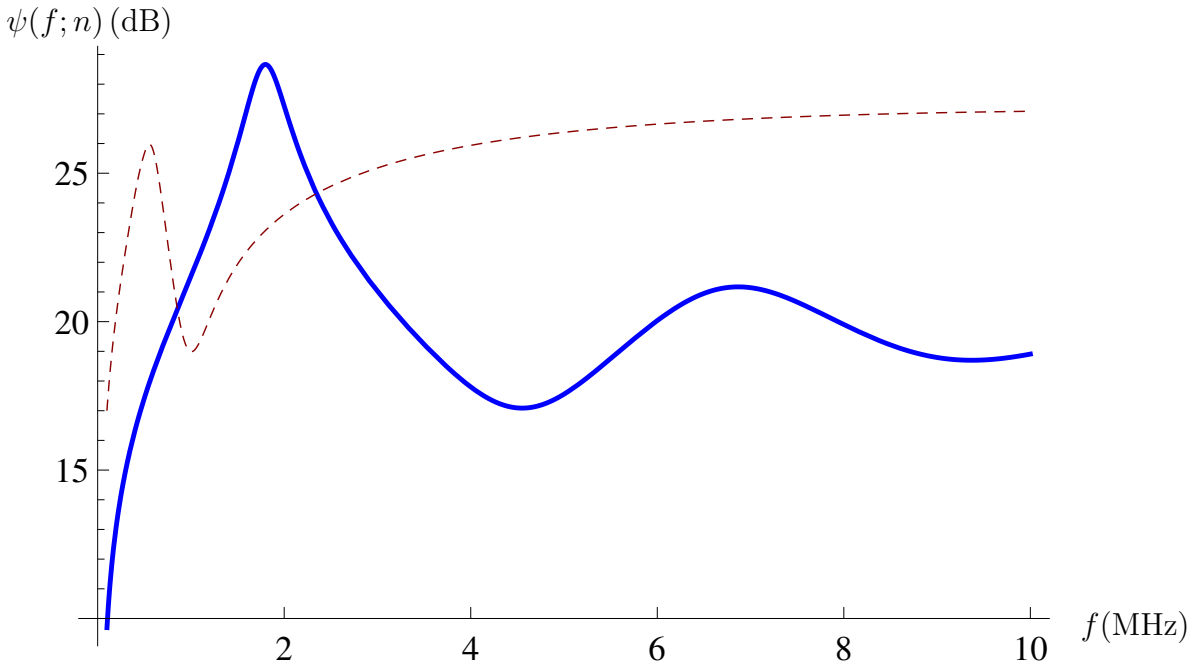

Figure 50: Non-dimensionalised transmission sensitivity (equation (278)) versus frequency for the $SG(3)$ lattice transducer at fractal generation level $n = 5$ (dashed line). The non-dimensionalised transmission sensitivity of the standard (Euclidean) transducer (equation (183)) is plotted for comparison (full line). Parameter values are given in Table 4.

The transmission sensitivity of the fractal design in generation level $n = 5$ has a maximum amplitude (gain) that is lower than the homogenised case (standard Euclidean design) at its lower operating frequency (at 0.55 MHz its sensitivity is 26 dB and the peak sensitivity of the standard (Euclidean) device is 29 dB at 1.8 MHz). The bandwidth of around 25 dB is smaller than that of the Euclidean case (see Table 3).

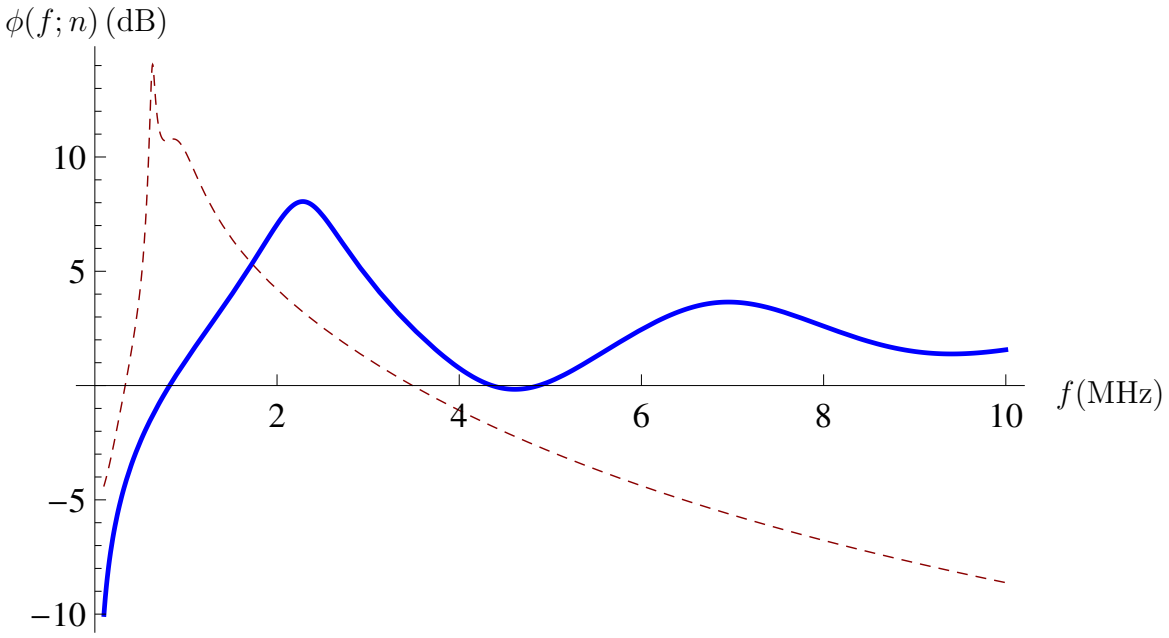

Figure 51: Non-dimensionalised reception sensitivity (equation (291)) versus frequency for the $SG(3)$ lattice transducer at fractal generation level $n = 5$ (dashed line). The non-dimensionalised reception sensitivity of the standard (Euclidean) transducer (equation (184)) is plotted for comparison (full line). Parameter values are given in Table 4.

The reception sensitivity of the fractal design in generation level $n = 5$ has again a much higher peak amplitude than that of the Euclidean case at its lower operating frequency (at 0.6 MHz its sensitivity is 14 dB whereas the peak sensitivity of the standard (Euclidean) device is 8 dB at 2.3 MHz). This examination can continue and below we consider the sixth generation level ($n = 6$) performance.

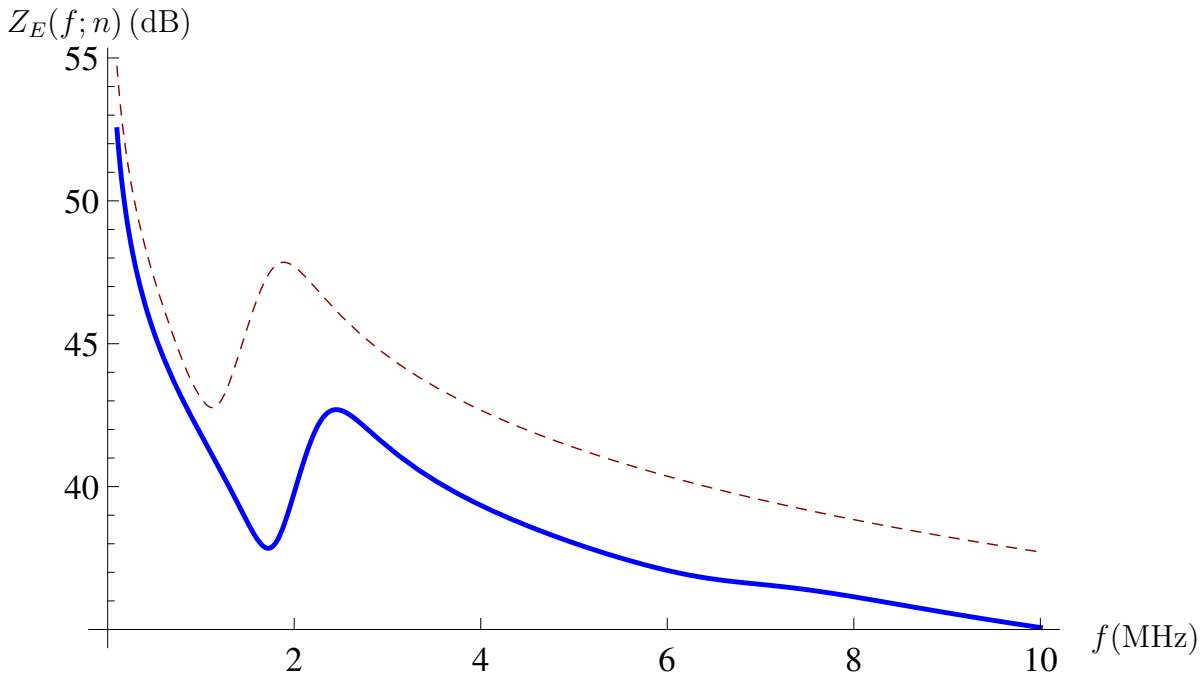

Figure 52: Non-dimensionalised electrical impedance (equation (267)) versus frequency for the $SG(3)$ lattice transducer at fractal generation level $n = 6$ (dashed line). The non-dimensionalised electrical impedance of the standard (Euclidean) transducer (equation (180)) is plotted for comparison (full line). Parameter values are given in Table 4.

At fractal generation level $n = 6$ the electrical impedance of the fractal lattice has its first resonance at around 1.2 MHz. This is at a higher impedance gain than the Euclidean case (which resonates at a higher frequency) and again the higher frequency resonances are absent.

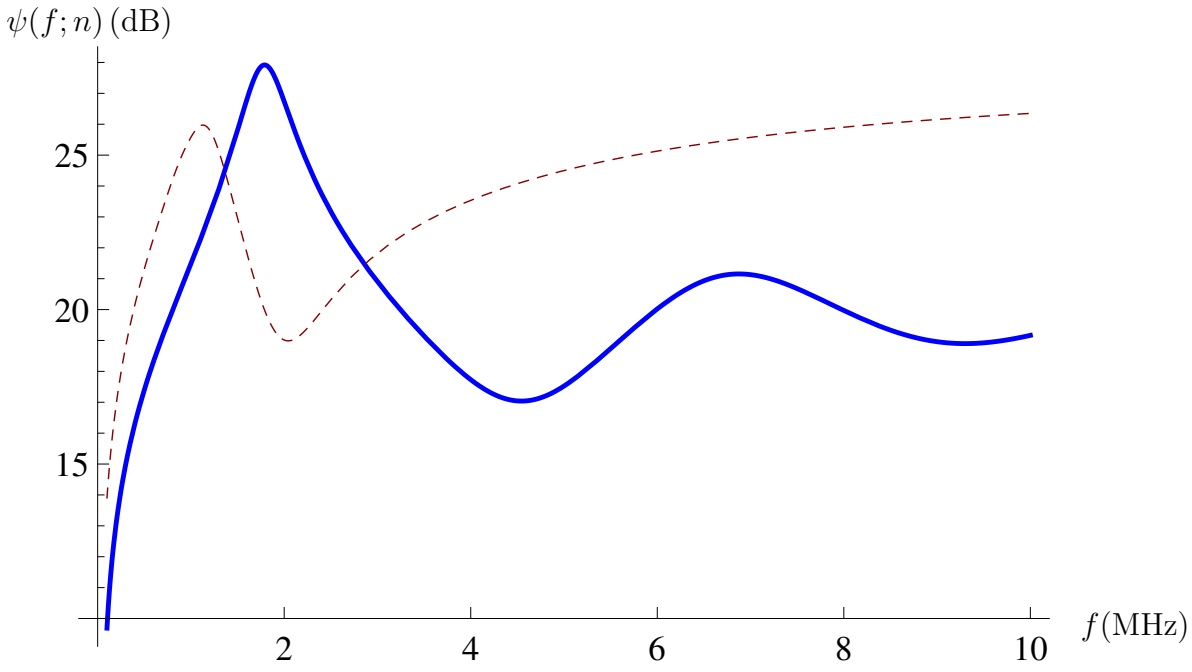

Figure 53: Non-dimensionalised transmission sensitivity (equation (278)) versus frequency for the $SG(3)$ lattice transducer at fractal generation level $n = 6$ (dashed line). The non-dimensionalised transmission sensitivity of the standard (Euclidean) transducer (equation (183)) is plotted for comparison (full line). Parameter values are given in Table 4.

The transmission sensitivity of the fractal design in generation level $n = 6$ has a maximum amplitude (gain) that is lower than the Euclidean case (at 1.1 MHz its sensitivity is 26 dB and the peak sensitivity of the standard device is 28 dB at 1.8 MHz). Once again the bandwidth around 25 dB is smaller than that of the homogenised case.

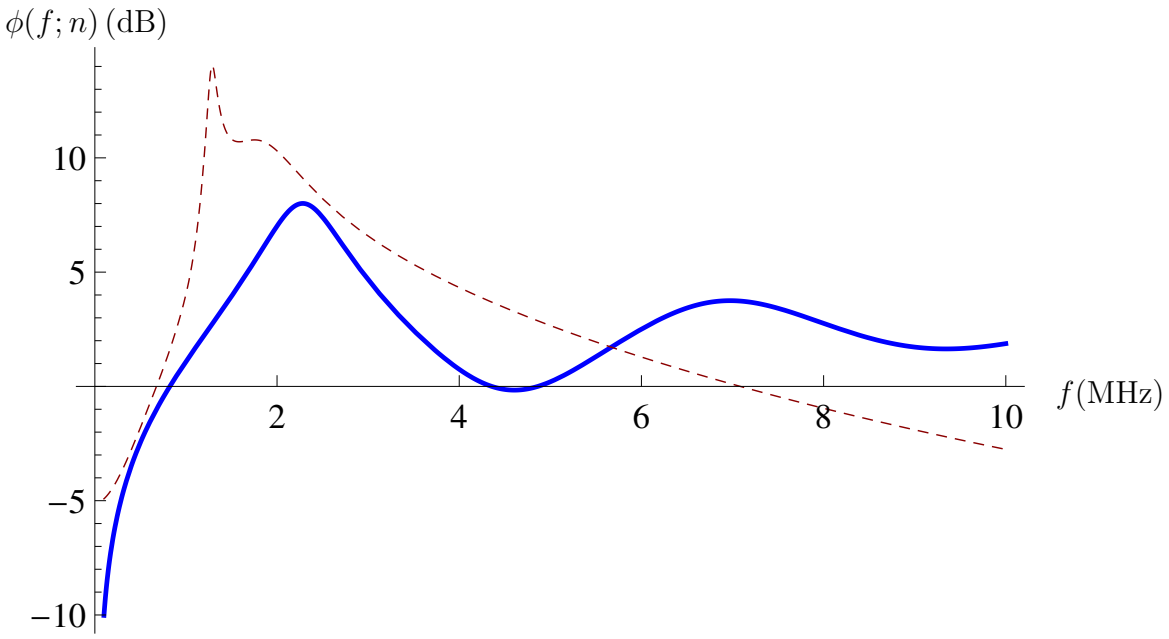

Figure 54: Non-dimensionalised reception sensitivity (equation (291)) versus frequency for the $SG(3)$ lattice transducer at fractal generation level $n = 6$ (dashed line). The non-dimensionalised reception sensitivity of the standard (Euclidean) transducer (equation (184)) is plotted for comparison (full line). Parameter values are given in Table 4.

As before the reception sensitivity maximum amplitude of the fractal design (in generation level $n = 6$) is higher than the Euclidean case (14 dB at 1.3 MHz compared to 8 dB at 2.3 MHz for the Euclidean case), with the bandwidth around this peak sensitivity being bigger than that of the Euclidean case.

Generation level (n)	Mechanical Resonant Frequency (MHz)		Electrical Resonant Frequency (MHz)		Transmission Sensitivity Gain (dB)		Transmission Sensitivity Bandwidth (MHz)		Reception Sensitivity Gain (dB)		Reception Sensitivity Bandwidth (MHz)	
	R	H	R	H	R	H	R	H	R	H	R	H
4	0.25	1.7	0.45	2.5	26	31	0	0.3	14	8	0.5	1.5
5	0.54	1.7	0.93	2.5	26	29	0.2	0.8	14	8	1.5	1.5
6	1.2	1.7	2	2.5	26	28	0.5	1	14	8	3	1.5

Table 3: A comparison between the operating characteristics of a fractal transducer (using the renormalisation approach (R)) and an equation standard design (using homogenisation approach (H))

9.2 Homogeneous Euclidean transducers

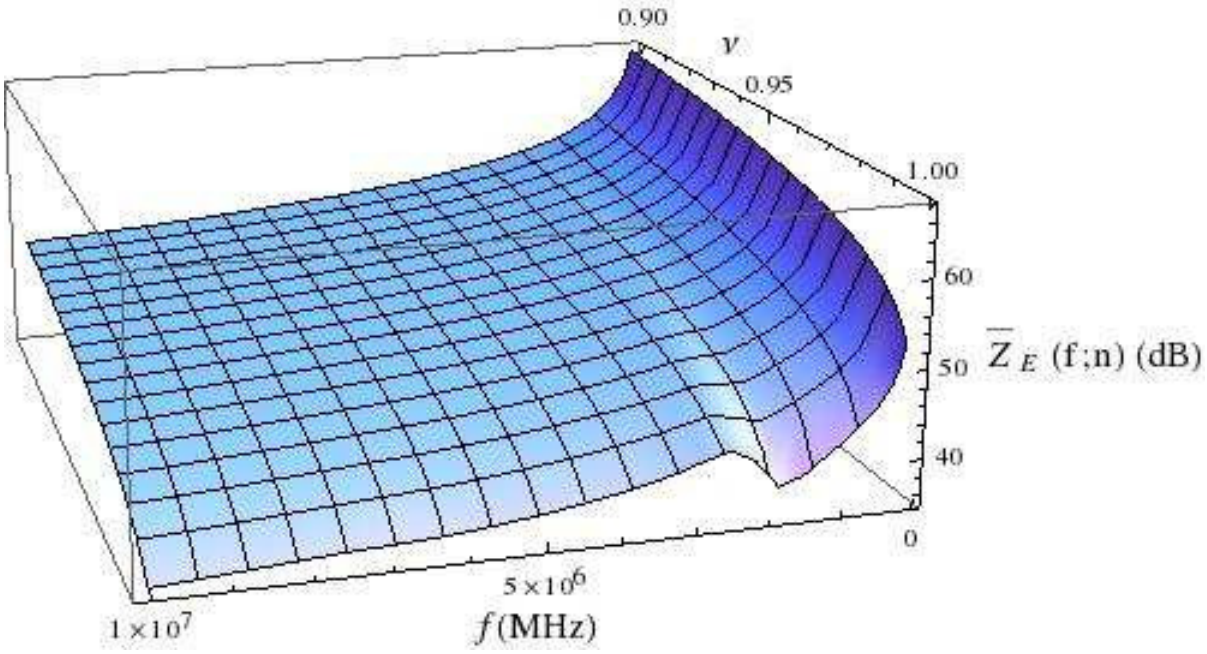

Figure 55: Non-dimensionalised electrical impedance of the standard (Euclidean) transducer $\bar{Z}_E(f;n)$ (dB) (equation (180)) versus frequency f(MHz) and volume fraction of ceramic ν for a 1-3 composite transducer. Parameter values are given in Table 4.

The electrical impedance of the standard (Euclidean) design was calculated using the homogenisation approach that led to equation (180). As can be seen in Figure 55 the resonances (peaks in the electrical impedance amplitude) only appear once the volume fraction of the polymer (ν) exceeds a threshold of roughly 0.95.

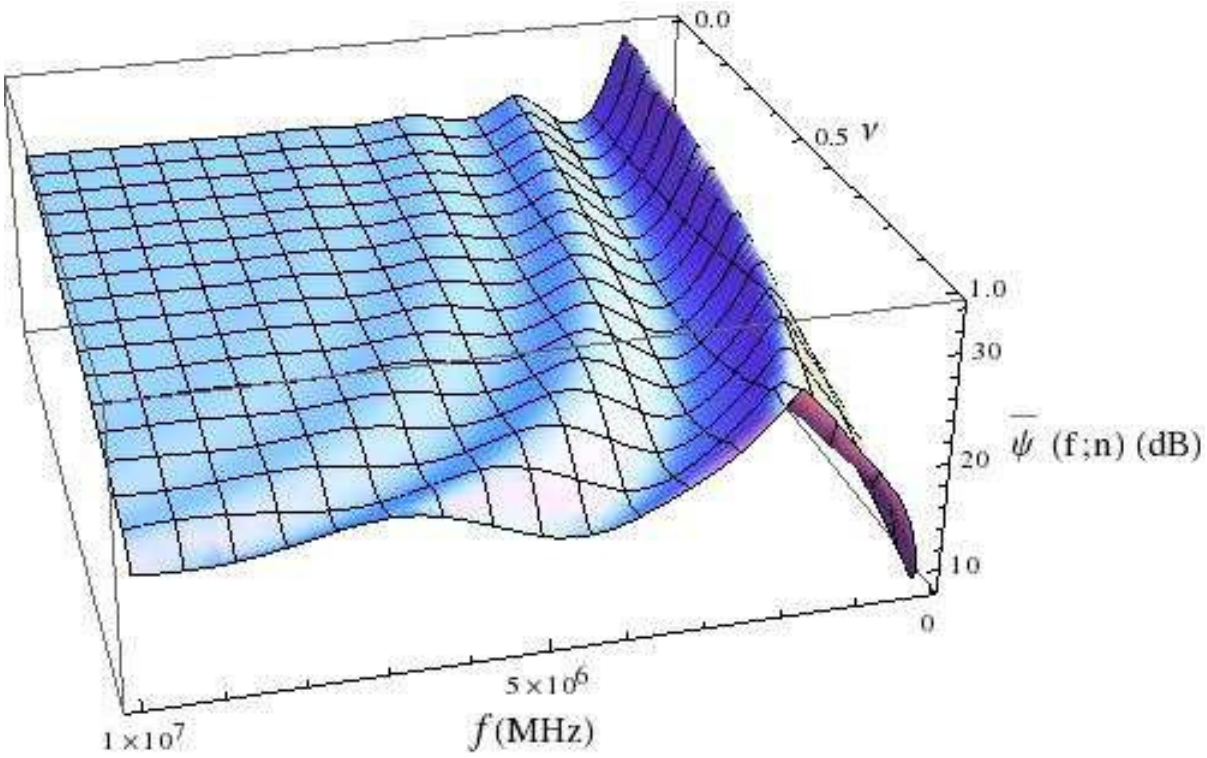

Figure 56: Non-dimensionalised transmission sensitivity of the standard (Euclidean) transducer $\psi(f;n)$ (dB) (equation (183)) versus frequency f(MHz) and volume fraction of ceramic ν for a 1-3 composite transducer. Parameter values are given in Table 4.

At the low volume fraction of the polymer (ν) there is a number of resonances. As the volume fraction increases these resonances shift to higher frequencies. It can be seen that the peak sensitivity is 28 dB and the bandwidth around this peak sensitivity is bigger at the low volume fractions of the polymer (ν).

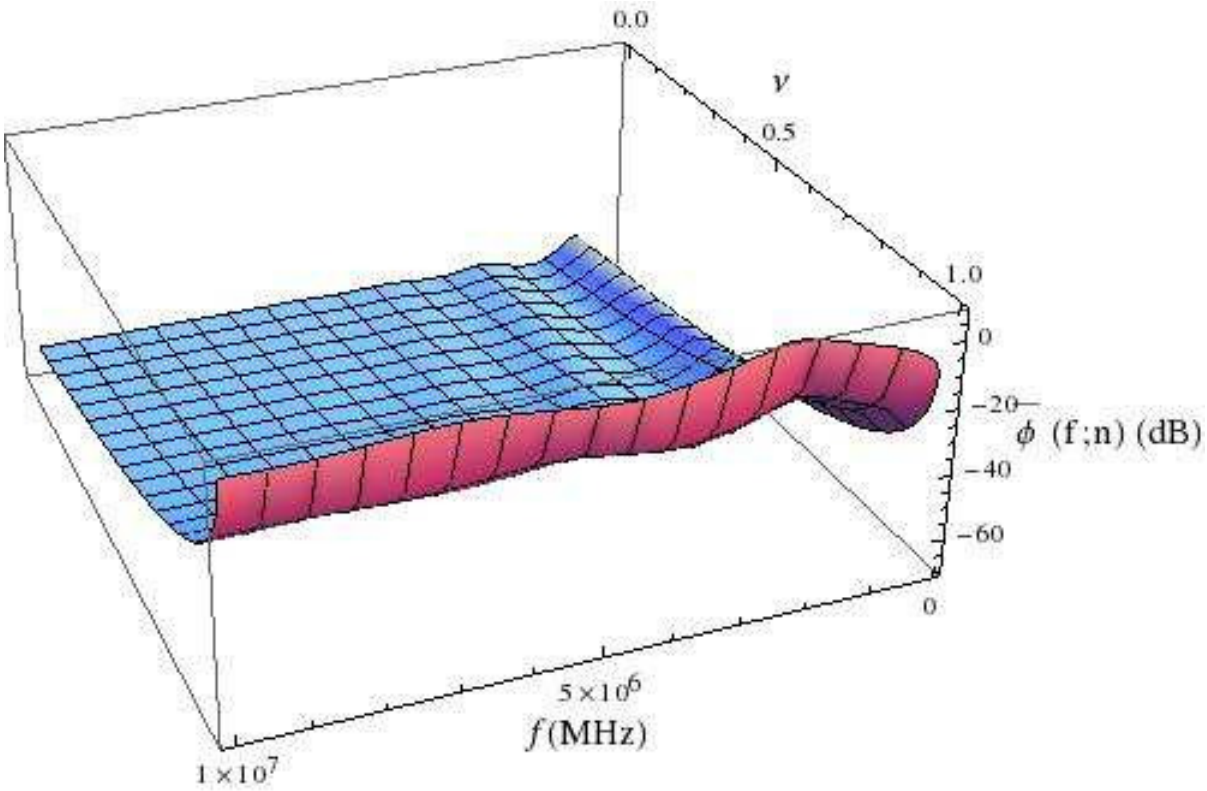

Figure 57: Non-dimensionalised reception sensitivity of the standard (Euclidean) transducer $\phi(f;n)\,(\mathrm{dB})$ (equation (184)) versus frequency $f(\mathrm{MHz})$ and volume fraction of ceramic ν for a 1-3 composite transducer. Parameter values are given in Table 4.

At low volume fractions of the polymer (ν) there are a number of resonances in the low frequency regime. As the volume fraction of ceramic increases the peak sensitivity increases as well.

Design Parameter	Symbol	Magnitude	Dimensions
Parallel electrical impedance load	Z_P	1000	Ohms
Series electrical impedance load	Z_0	50	Ohms
Length of fractal	L	0.5	mm
Mechanical impedance of the front load	Z_L	1.5	MRayls
Mechanical impedance of the backing layer	Z_B	0.02	MRayls

Table 4: Parameter Values for the Sierpinski Gasket Transducer [22, 23].

9.3 Convergence

The norm of the difference between the energy in the power spectrum at successive generation levels, integrated with respect to frequency, is calculated for the transmission/reception sensitivities, as follows

$$\sum_{i=1}^{m} |\psi(f_i; n) - \psi(f_i; n+1)| = \psi^*(n), \tag{320}$$

and

$$\sum_{i=1}^{m} |\phi(f_i; n) - \phi(f_i; n+1)| = \phi^*(n). \tag{321}$$

where $\psi^*(n)$ and $\phi^*(n)$ record the convergence of the transmission and reception sensitivities respectively as the fractal generation level increases. Figure 58 shows the dependence of these norms on the generation level. Scrutiny of the underlying spectra shows that the transmission sensitivity accrues more and more resonances as the fractal generation n increases. As the length scale of the smallest edge is decreasing with n then resonances at higher frequencies appear; again the lack of damping in the model permits these resonances to have amplitudes which would not be present in an experimental setting. As n

is increased further, then the various peaks become quite dense and a very flat response emerges which doesnt change over the frequency range of interest (up to 10MHz). Hence, the successive spectra start to reach a steady state and this accounts for the steady state that is reached after $n = 10$. A similar story holds for the reception sensitivity.

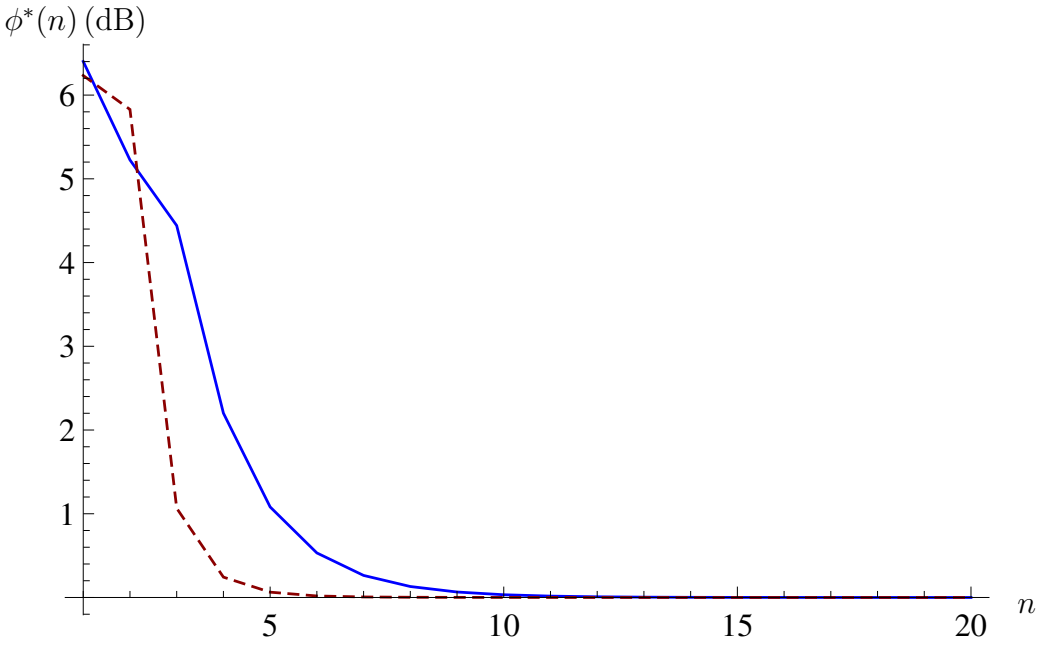

Figure 58: The convergence of the transmission and reception sensitivities is examined by plotting the differences in the energies in successive spectra as the fractal generation level increases. Non-dimensionalised transmission sensitivity ($\psi^*(n)$) (equation (320)) (full line) and non-dimensionalised reception sensitivity ($\phi^*(n)$) (equation (321)) (dashed line) versus the fractal generation level. The transmission sensitivity converges by generation level $n = 10$ and the reception sensitivity by generation level $n = 5$, over this frequency range where $f_i \in [0.1, 10]$MHz.

10 Conclusions

The performance of a composite piezoelectric ultrasound transducer, where its internal architecture is a fractal, is compared with that of a traditional design. The former case is modelled using a renormalisation approach whereas the latter case is modelled using homogenisation. In the previously published paper [3], only ceramic elements were used, however in this paper, this was improved on by using a combination of ceramic and polymer elements. New basis functions, whose support is the underlying fractal graph, were developed for the finite element analysis. To assess the performance of this new device a model for a homogenised device was derived. This represents the standard designs that are used whereby the piezoelectric and polymer constituents are on the same length scale and are often arranged in a periodic structure. A low fractal generation levels ($n = 4, 5$ and 6) of this new transducer was investigated as these are in the regime most likely to be amenable to manufacture. A significantly higher amplitude reception sensitivity was produced by the fractal transducer when compared to the standard design; note however that a lower transmission sensitivity amplitude resulted. The convergence of the fractal device's performance as the fractal generation level increases was also considered. It was seen that, in both transmission and reception modes, the outputs converge by generation level $n = 5$ and $n = 10$ respectively. The reception sensitivity also resulted in a wider bandwidth than the standard design; if we take the noise floor to be 3 dB below the peak gain of the traditional design. The positive results in this theoretical work have subsequently led to a program to manufacture these fractal devices. Our future work will then focus on a comparison between the results presented here and our experimental findings.

11 Appendix

11.1 Geometrical and basis function details for fractal generation levels $n = 1$ and $n = 2$

		Adjacent vertices to (x_j, y_j)			
j	(x_j, y_j)	(x_{j+1}, y_{j+1})	(x_{j+2}, y_{j+2})	(x_{j+3}, y_{j+3})	(x_{j+4}, y_{j+4})
1	$(0, 0)$	A	2	3	4
2	$(h, 0)$	1	3	B	4
3	$(\frac{h}{2}, \frac{\sqrt{3}h}{2})$	1	2	C	4
4	$(\frac{h}{2}, \frac{h}{2\sqrt{3}})$	1	2	3	
A	$(-h, 0)$	1			
B	$(2h, 0)$	2			
C	$(h, \sqrt{3}h)$	3			

Table 5: Coordinates of the vertices and a list of the adjacent vertices to vertex (x_j, y_j) for generation level $n = 1$. The vertex labelling is given in Figure 3.

j	(x_j, y_j)	Adjacent vertices to (x_j, y_j)			
		(x_{j+1}, y_{j+1})	(x_{j+2}, y_{j+2})	(x_{j+3}, y_{j+3})	(x_{j+4}, y_{j+4})
1	$(0, 0)$	A	2	3	4
2	$(h, 0)$	1	3	5	4
3	$(\frac{h}{2}, \frac{\sqrt{3}h}{2})$	1	2	9	4
4	$(\frac{h}{2}, \frac{h}{2\sqrt{3}})$	1	2	3	
5	$(2h, 0)$	2	6	7	8
6	$(3h, 0)$	5	7	B	8
7	$(\frac{5h}{2}, \frac{\sqrt{3}h}{2})$	5	6	10	8
8	$(\frac{5h}{2}, \frac{h}{2\sqrt{3}})$	5	6	7	
9	$(h, \sqrt{3}h)$	3	10	11	12
10	$(2h, \sqrt{3}h)$	7	9	11	12
11	$(\frac{3h}{2}, \frac{3\sqrt{3}h}{2})$	9	10	C	12
12	$(\frac{3h}{2}, \frac{7h}{2\sqrt{3}})$	9	10	11	
A	$(-h, 0)$	1			
B	$(4h, 0)$	6			
C	$(2h, 2\sqrt{3}h)$	11			

Table 6: Coordinates of the vertices and a list of the adjacent vertices to vertex (x_j, y_j) for generation level $n = 2$. The vertex labelling is given in Figure 4.

j	a	b	c	d	f	g
1	1	0	0	$-\frac{1}{h^2}$	$\frac{3}{h^2}$	$-\frac{4\sqrt{3}}{h^2}$
2	0	$\frac{2}{h}$	$-\frac{4\sqrt{3}}{h}$	$-\frac{1}{h^2}$	$\frac{3}{h^2}$	$\frac{4\sqrt{3}}{h^2}$
3	0	$-\frac{5}{h}$	$\frac{3\sqrt{3}}{h}$	$\frac{5}{h^2}$	$-\frac{3}{h^2}$	0
4	0	$\frac{3}{h}$	$\frac{\sqrt{3}}{h}$	$-\frac{3}{h^2}$		
5	0	$-\frac{2}{h}$	0	$-\frac{1}{h^2}$		
6	-3	$\frac{4}{h}$	0	$-\frac{1}{h^2}$		
7	-3	$\frac{2}{h}$	$\frac{2\sqrt{3}}{h}$	$-\frac{1}{h^2}$		

Table 7: Coefficients of the basis functions ϕ_j $j = 1, \ldots, 4$ (see equations (61), (63) and (74)) and ψ_j $j = 5, 6, 7$ (see equations (65) and (67)) for fractal generation level $n = 1$.

j	a	b	c	d	f	g
1	1	0	0	$-\frac{1}{h^2}$	$\frac{3}{h^2}$	$-\frac{4\sqrt{3}}{h^2}$
2	0	$\frac{2}{h}$	$-\frac{4\sqrt{3}}{h}$	$-\frac{1}{h^2}$	$\frac{3}{h^2}$	$\frac{4\sqrt{3}}{h^2}$
3	0	$-\frac{5}{h}$	$\frac{3\sqrt{3}}{h}$	$\frac{5}{h^2}$	$-\frac{3}{h^2}$	0
4	0	$\frac{3}{h}$	$\frac{\sqrt{3}}{h}$	$-\frac{3}{h^2}$		
5	-3	$\frac{4}{h}$	$\frac{8\sqrt{3}}{h}$	$-\frac{1}{h^2}$	$\frac{3}{h^2}$	$-\frac{4\sqrt{3}}{h^2}$
6	-8	$\frac{6}{h}$	$-\frac{12\sqrt{3}}{h}$	$-\frac{1}{h^2}$	$\frac{3}{h^2}$	$\frac{4\sqrt{3}}{h^2}$
7	30	$-\frac{25}{h}$	$\frac{3\sqrt{3}}{h}$	$\frac{5}{h^2}$	$-\frac{3}{h^2}$	0
8	-18	$\frac{15}{h}$	$\frac{\sqrt{3}}{h}$	$-\frac{3}{h^2}$		
9	-3	$\frac{14}{h}$	$-\frac{2\sqrt{3}}{h}$	$-\frac{1}{h^2}$	$\frac{3}{h^2}$	$-\frac{4\sqrt{3}}{h^2}$
10	30	$-\frac{8}{h}$	$-\frac{14\sqrt{3}}{h}$	$-\frac{1}{h^2}$	$\frac{3}{h^2}$	$\frac{4\sqrt{3}}{h^2}$
11	-8	$-\frac{15}{h}$	$\frac{9\sqrt{3}}{h}$	$\frac{5}{h^2}$	$-\frac{3}{h^2}$	0
12	-18	$\frac{9}{h}$	$\frac{7\sqrt{3}}{h}$	$-\frac{3}{h^2}$		
13	0	$-\frac{2}{h}$	0	$-\frac{1}{h^2}$		
14	-15	$\frac{8}{h}$	0	$-\frac{1}{h^2}$		
15	-15	$\frac{4}{h}$	$\frac{4\sqrt{3}}{h}$	$-\frac{1}{h^2}$		

Table 8: Coefficients of the basis functions ϕ_j $j = 1, \ldots, 12$ (see equations (69), (71), (73) and (74)) and ψ_j $j = 13, 14, 15$ for fractal generation level $n = 2$.

11.2 The material properties of PZT-5H [4, 36, 37]

$$c_{pq}^{E} = \begin{bmatrix} 12.6 & 7.95 & 8.41 & 0 & 0 & 0 \\ 7.95 & 12.6 & 8.41 & 0 & 0 & 0 \\ 8.41 & 8.41 & 11.7 & 0 & 0 & 0 \\ 0 & 0 & 0 & 2.3 & 0 & 0 \\ 0 & 0 & 0 & 0 & 2.3 & 0 \\ 0 & 0 & 0 & 0 & 0 & 2.325 \end{bmatrix} \times 10^{10} N/m^2, \tag{322}$$

$$e_{ip} = \begin{bmatrix} 0 & 0 & 0 & 0 & 17 & 0 \\ 0 & 0 & 0 & 17 & 0 & 0 \\ -6.5 & -6.5 & 23.3 & 0 & 0 & 0 \end{bmatrix} C/m^2, \tag{323}$$

$$\varepsilon_{ij}^{E} = \begin{bmatrix} 1700\varepsilon_0 & 0 & 0 \\ 0 & 1700\varepsilon_0 & 0 \\ 0 & 0 & 1470\varepsilon_0 \end{bmatrix} C/(Vm). \tag{324}$$

where $\varepsilon_0 = 8.854 \times 10^{-12}\, C/(Vm)$. The density is $\rho^E = 7500\, kgm^{-3}$.

11.3 The material properties of polymer HY1300/CY1301 hardset [22, 30]

$$c_{pq}^{P} = \begin{bmatrix} 0.71976 & 0.404985 & 0.404981 & 0 & 0 & 0 \\ 0.40498 & 0.71976 & 0.40498 & 0 & 0 & 0 \\ 0.40498 & 0.40498 & 0.71976 & 0 & 0 & 0 \\ 0 & 0 & 0 & 0.15739 & 0 & 0 \\ 0 & 0 & 0 & 0 & 0.15739 & 0 \\ 0 & 0 & 0 & 0 & 0 & 0.15739 \end{bmatrix} \times 10^{10} N/m^2, \tag{325}$$

and

$$\varepsilon_{ij}^{P} = \begin{bmatrix} 4\varepsilon_0 & 0 & 0 \\ 0 & 4\varepsilon_0 & 0 \\ 0 & 0 & 4\varepsilon_0 \end{bmatrix} C/(Vm). \tag{326}$$

where The density is $\rho^P = 1150\, kgm^{-3}$.

References

[1] J. Abdulbake, A. J. Mulholland, and J. Gomatam. A renormalization approach to reaction-diffusion processes on fractals. *Fractals*, 11(4):315–330, (2003).

[2] J. Abdulbake, A. J. Mulholland, and J. Gomatam. Existence and stability of reaction-diffusion waves on a fractal lattice. *Chaos, Solitons and Fractals*, 20(4):799–814, (2004).

[3] E. A. Algehyne and A. J. Mulholland. A finite element approach to modelling fractal ultrasonic transducers. *IMA Journal of Applied Mathematics*, first published online May 29, 2015, doi: 10.1093/imamat/hxv012, (2015).

[4] B. A. Auld. *Acoustic Fields and Waves in Solids,* 1. John Wiley and Sons, New York, (1973).

[5] M. T. Barlow. *Diffusion on fractals.* Lectures on probability theory and statistics, Berlin: Springer, ed. P Bernard, (1998). Lecture Notes in Mathematics 1690, 1-121.

[6] R. T. Beyer and S. V. Letcher. *Physical Ultrasonics.* Academic Press, New York, (1969).

[7] A. M. Chiselev, L. Moraru, and A. Gogu. Localization of an object using a bat model inspired from biology. *J. Biophys*, 19(4):251–258, (2009).

[8] F. M. de Espinosa, O. Martinez, L. E. Segura, and L. Gomez-Ullate. Double frequency piezoelectric transducer design for harmonic imaging purposes in NDT. *IEEE. TUFFC*, 52(6):980–986, (2005).

[9] D. F. Eberl, R. W. Hardy, and M. J. Kernan. Genetically similar transduction mechanisms for touch and hearing in drosophila. *J. Neurosci*, 20(16):5981–5988, (2000).

[10] K. Falconer. *Fractal Geometry: Mathematical Foundations and Applications*. John Wiley and Sons Ltd, Chichester, England, (2003).

[11] K. Falconer and J. Hu. Nonlinear diffusion equations on unbounded fractal domains. *J Math Anal App*, 256:606–624, (2001).

[12] P. J. Grabner G. Derfel and F. Vogl. Laplace operators on fractals and related functional equations. *J. Phys. A: Math. Theor*, 463001(45):doi:10.1088/1751–8113/45/46/463001, (2012).

[13] G. Hayward. A systems feedback representation of piezoelectric transducer operational impedance. *Ultrasonics*, 22:153–162, (1984).

[14] G. Hayward, C. J. McLeod, and T. S Duranni. A systems model of the thickness mode piezoelectric transducer. *JASA*, 76(2):369–382, (1984).

[15] IEEE and ANSI. Institute of electrical and electronic engineers, inc. *An American Naional Standard: IEEE Standard on Piezoelectricity*, (1988).

[16] Wolfram Research, Inc. *Mathematica*. Version 10.0. Champaign, Illinois, (2014).

[17] J. Kigami. *Analysis on Fractals*. Cambridge University Press, Cambridge, UK, (2001).

[18] Giona M. Transport phenomena in fractal and heterogeneous media: Input/output renormalization and exact results. *Chaos, Solitons and Fractas*, 7(9):1371–1396, (1996).

[19] M. K. Schwalm M. Giona, W. A.Schwalm and A. Adrover. Exact solution of linear transport equations in fractal media - I. Renormalization analysis and general theory. *Chem. Eng. Sci*, 51(20):4717–4729, (1996).

[20] R. N. Miles and R. R. Hoy. The development of a biologically-inspired directional microphone for hearing aids. *Audiol Neurootol*, 11(2):86–94, (2006).

[21] A. J. Mulholland. Bounds on the Hausdorff dimension of a renormalisation map arising from an excitable reaction-diffusion system on a fractal lattice. *Chaos, Solitons and Fractals*, 35(2):274–284, (2008).

[22] A. J. Mulholland, S. N. Ramadas, R. L. O'Leary, A.C. S. Parr, A. Troge, G. Hayward, and R. A. Pethrick. A Theoretical Analysis of a Piezoelectric Ultrasound Device with an Active Matching Layer. *Ultrasonics*, 47(1):102–110, (2007).

[23] A. J. Mulholland and A. J. Walker. Piezoelectric ultrasonic transducers with fractal geometry. *Fractals*, 19(4):469–479, (2011).

[24] A. J. Mulholland, A. J. Walker, J. W. Mackersie, R. L. O'Leary, A. Gachagan, and N. Ramadas. The Use of Fractal Geometry in the Design of

Piezoelectric Ultrasonic Transducers. *Ultrasonics Symposium (IUS)*, 2011 *IEEE International*, Orlando, FL:1559–1562, (2011).

[25] R. Müller. A numerical study of the role of the tragus in the big brown bat. *JASA*, 116(6):3701–3712, (2004).

[26] R. Müller, H. Lu, S. Zhang, and H. Peremans. A helical biosonar scanning pattern in the chinese noctule nycatalus plancyi. *JASA*, 119(6):4083–4092, (2006).

[27] B. Nadrowski, J. T. Albert, and M. C. Göpfert. Transducer-Based Force Generation Explains Active Process in Drosophila Hearing. *Curr. Biol*, 18:1365–1372, (2008).

[28] L. A. Orr, A. J. Mulholland, R. L. O'Leary, and G. Hayward. Analysis of Ultrasonic Transducers with Fractal Architecture. *Fractals*, 16(4):333–349, (2008).

[29] L. A. Orr, A. J. Mulholland, R. L. O'Leary, A. Parr, R. Pethrick, and G. Hayward. Theoretical Modelling of Frequency Dependent Elastic Loss in Composite Piezoelectric Transducers. *Ultrasonics*, 47(1):130–137, (2007).

[30] R.L. OLeary, G. Smillie, G. Hayward, and A.C.S. Parr. CUE materials database, Technical Report. *Centre for Ultrasonic Engineering, University of Strathclyde, Glasgow, Scotland*, (2002). www.cue.ac.uk.

[31] D. Robert and M. C. Göpfert. Novel schemes for hearing and orientation in insects. *Curr. Opin. Neurobiol*, 12:715–720, (2002).

[32] W. A. Schwalm and M. K. Schwalm. Extension theory for lattice Green functions. *Phys.Rev.B*, 37(16):9524–9542, (1988).

[33] W. A. Smith and B. A. Auld. Modeling 1-3 composite piezoelectric: Thickness-mode oscillations. *IEEE*, 38(1):40–47, (1991).

[34] H. F. Tiersten. Thickness vibrations of piezoelectric plates. *JASA*, 35(1):53–58, (1963).

[35] H. F. Tiersten. *Linear Piezoelectric Plate Vibrations*. Plenum, New York, (1969).

[36] J. Yang. *Analysis of Piezoelectric Devices*. World Scientific, Singapore, (2006).

[37] J. Yang. *The Mechanics of Piezoelectric Structures*. World Scientific, Singapore, (2006).